PROCESSING AND MICROSTRUCTURE EFFECTS ON THE STRENGTH AND THE LOCALIZED CORROSION RESISTANCE OF ULTRA-FINE GRAINED Al-Mg-Si ALLOYS

A Dissertation

by

RAMATOU LY

Submitted to the Office of Graduate and Professional Studies of
Texas A&M University
in partial fulfillment of the requirements for the degree of

DOCTOR OF PHILOSOPHY

Chair of Committee,	Homero Castaneda-Lopez
Co-Chair of Committee,	Karl. T. Hartwig
Committee Members,	Ankit Srivastava
	Hong Liang
Head of Department,	Ibrahim Karaman

December 2019

Major Subject: Materials Science and Engineering

ABSTRACT

Improving the strength, and the corrosion resistance of aluminum alloys simultaneously through aging treatment, and grain refinement is a challenge as these two properties are mutually exclusive. In this work, we investigated the effects of shear banding, dynamic recrystallization, and precipitation on the corrosion susceptibility, and the strength of an ultra-fine grained (UFG) AA6061 aluminum alloy. For that, we extruded the material by equal channel angular pressing (ECAP) up to seven passes following route Bc combined with a post-aging treatment at 100 ˚C. We first characterized the microstructure after processing in depth before investigating corrosion susceptibility by accelerated immersion tests, and electrochemical testing. We found that after 3 ECAP passes, the AlFeSi intermetallic compounds are fragmented and closely spaced along the shear direction and within the shear planes of the material making this direction and plane highly susceptible to pitting. Besides, the shear bands are preferred regions for precipitation after post-aging treatment. Therefore the corrosion susceptibility of UFG AA6061 alloys is tailored by the shear bands network of the material, and the precipitation within the bands.The immersion and electrochemical tests reveal that filiform corrosion, and intergranular corrosion (IGC) are severe when the material is partially recrystallized and peak aged. Also, the bulk potentiodynamic response is significantly affected by the bulk composition, and the precipitation within the shear bands. In addition, passivation is easier after ECAP regardless of the post-aging treatment. However the passive film is less stable. We also found that dynamic recrystallization decreases the susceptibility to IGC even at peak aging by reducing the volume fraction and the length of the shear bands. Thus in UFG AA6061 aluminum alloys, the energy stored in the grains seems to influence the susceptibility to IGC more than grain boundary precipitation.

DEDICATION

To my parents, my family, and all my friends from Cote d'Ivoire, France, Senegal, Mali, and the United States who have always motivated me, encouraged me, and extended all the help and the support I needed to succeed in this journey.

ACKNOWLEDGEMENTS

I would like to thank my advisor Dr. Homero Castaneda, and my co-advisor Dr. Karl Hartwig for their guidance, and support throughout my Ph.D. My thanks also go to my committee members, Dr. Ankit Srivastava, Dr. Bruce Tai, and Dr. Hong Liang for their interests in my research. Thank you to Dr. Xinghang Zhang for advising me before moving to Purdue University.

I am grateful to all the professors and staffs who helped me in my research, and my studies. Thank you to Robert Barber, and Michael Elverud for their technical assistance in performing the ECAP. Thank you to Murat Kaynak, and Dharmesh Patel for their help, time and sympathy. Thanks also go to Dr. Stanislav Verkhoturov for assisting me with the SIMS, Dr. Chun Hsin Kuo for helping me with the SEM, and Dr. Wilson Serem for his guidance with the AFM. I am thankful to Dr. Ahmad Ivan Karayan for his advice, and contributions to the work presented. Many thanks to Yenny Cubides for helping me with the drawings, Wahaz Nasim for his assistance during the EBSD analysis, and Abhinav Srivastava for guiding me during the mechanical testing.

Thank you to Dr. Indranhil Roy, and Dr. Agathe Robisson, for their dedication, and unconditional support when I started my Ph.D. journey at Texas A&M.

Thanks also go to my friends Shuang Quin, Parvin Karimi, Lin Chen, Yash Parikh, Hanna Hlushko, Chin-Hua Cheng, Taymaz Jozaghi and the whole corrosion group for making my time at Texas A&M University a great, and unforgettable experience.

CONTRIBUTORS AND FUNDING SOURCES

This work was initially supported by SCHLUMBERGER. The ECAP processing and the mechanical testing were supervised by Dr. Karl T. Hartwig, co-advisor - emeritus professor in the Department of Materials Science & Engineering of Texas A&M. The corrosion testing were supervised by Dr. Homero Castaneda, advisor-Assistant professor in the Department of Materials Science & Engineering of Texas A&M - Director of the national corrosion & materials reliability lab.

Sections 3, 4, and 5 were supervised by Dr. Karl T. Hartwig, Dr. Homero Castaneda, Dr. Ankit Srivastava, Dr. Hong Liang and Dr. Ivan Ahmad Karayan, post-doc fellow in the Department of Materials Science & Engineering of Texas A&M. These sections were published in 2018 and 2019 in three articles listed in the biographical sketch.

NOMENCLATURE

SPD	Severe Plastic Deformation
ARB	Accumulating Roll Bonding
HPT	High Pressure Torsion
ECAP	Equal Channel Angular Processing
UFG	Ultra-Fine Grained
GB	Grain Boundary
IGC	Intergranular Corrosion
IMC	Intermetallic Compounds
HAGBs	High Angle Boundaries
LAGBs	Low Angle Boundaries
SCE	Saturated Calomel Electrodes
EBSD	Electron Backscatter Diffraction
SEM	Scanning Electron Microscope
TEM	Transmission Electron Microscope
HRTEM	High Resolution Transmission Electron Microscope
OM	Optical Microscope
VPD	Volta Potential Difference
TOF-SIMS	Time of Flight Secondary Ions Mass Spectrometry
AFM	Atomic Force Microscopy
SKPFM	Scanning Kelvin Probe Force Microscopy
DRX	Dynamic Recrystallization

PFZ	Precipitation Free Zone
E_{corr}	Corrosion potential
E_{pit}	Pitting potential
E_{rep}	Repassivation potential
OCP	Open Circuit Potential
CPP	Cyclic Potentiodynamic Polarization
Rp	Polarization Resistance
XRD	X-Ray diffraction
3D-APT	3D Atom Probe Tomography
CSL	Coincidence Site Lattice

TABLE OF CONTENTS

Page

Page

LIST OF FIGURES

Page

Page

Page

Page

LIST OF TABLES

1. INTRODUCTION

1.1 Background

Over the past three decades, several processing routes known as severe plastic deformation (SPD) techniques have been developed to enhance the physical, and the mechanical properties of aluminum alloys[1]. These includes accumulate roll bonding (ARB), high-pressure torsion (HPT), and equal channel angular extrusion/processing (ECAP). They have been successful in improving the strength, electrical conductivity, and thermal stability of aluminum alloys in the laboratory through grain refinement, precipitation hardening, dislocation and particles strengthening[2] with ECAP being the most promising technique for large scale application among all.

Although the mechanical behavior of ultra-fine grained (UFG) materials has been well studied, and modeled in the literature, their corrosion susceptibility is still a challenging behavior to characterize and fully understand. Proofs are the existing controversial results reported in the literature even among the same family of aluminum grade. These conflicting results are mainly due to the large choice of processing routes offered by these SPD techniques, the sensibility of the extruded material's microstructure to processing parameters (post-aging conditions, processing temperature and speed), and the synergetic effects of grain boundary, dislocations, precipitates, and shear banding on corrosion mechanisms.

Therefore the goal of this study is (i) to understand the effects of microstructure and processing effects on the strength and corrosion resistance of UFG AA6061 aluminum alloys, (iii) elucidate the corrosion degradation mechanisms of UFG Al-Mg-Si alloys, and (ii) find the optimal microstructure design and processing parameters for high strength aluminum alloy with improved localized corrosion resistance.

1.2 Technical Approach

We focused our study on AA6061 aluminum alloy (maximal nominal composition[21]: Si 0.6wt%, Mg 0.9wt%, Cu 0.35wt%, Fe 0.7wt%, Mn 0.08wt%), which is the most extruded aluminum grade due to its high formability. We carried out the ECAP process at room temperature up to 3 passes, and at 125 ˚C up to 7 passes to achieve higher strain deformation. All extrusions passes were performed at a pressing speed of 5 mm/sec following route Bc (90˚ rotation between each pass). We investigated the effects of low-temperature post-aging treatment on corrosion by aging the material at 100 ˚C up to 3 days following ECAP (Fig. 1).

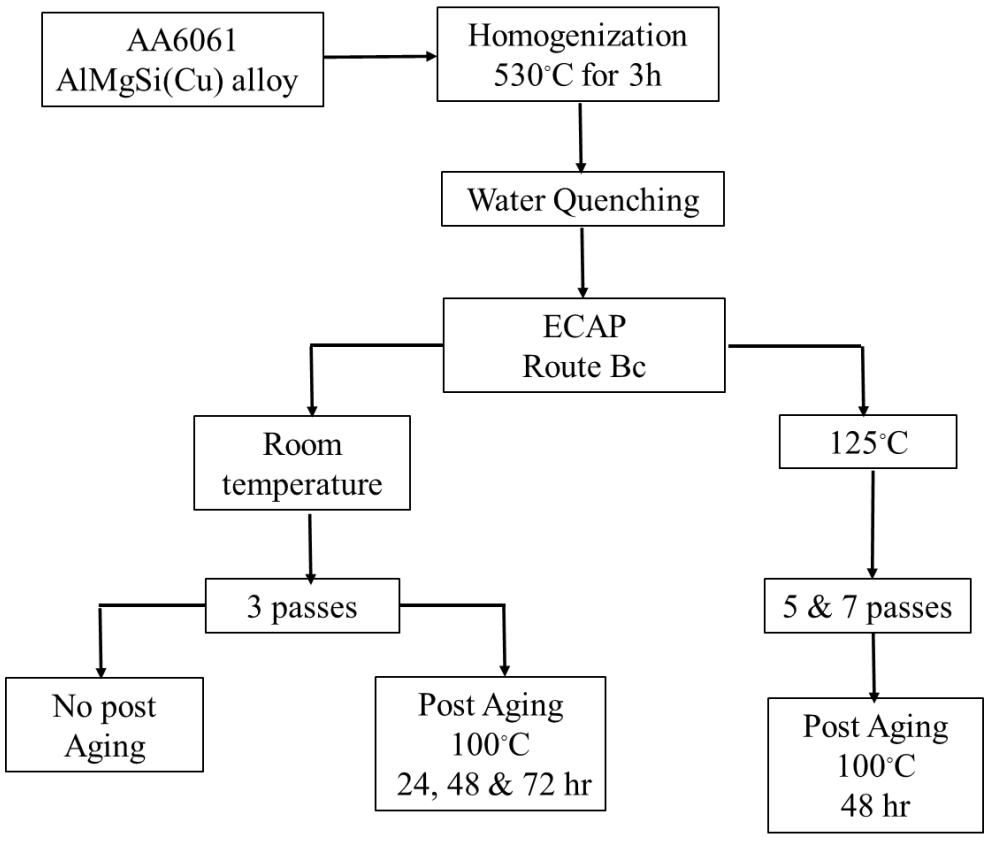

Figure 1: Test Matrix.

1.3 Dissertation Outline

The first part of section 2 gives an overview of the literature on the principle of ECAP processing, and its effects on the microstructure and the mechanical properties of UFG AA6061. In the second section, we provided a literature review on the corrosion mechanisms of aluminum alloys and how SPD techniques influence them.

Section 3 provides more insights into particles distribution, and precipitation phenomena in a partially recrystallized microstructure (3 passes) after aging treatment at 100 ˚C up to 3 days. The second part of the section investigates the effects of shear banding on corrosion. As a result, shear bands are preferred site for precipitation, and therefore corrosion in UFG AA6061.

Section 4 investigates the relationship between corrosion events (pitting filiform corrosion and IGC) and the electrochemical response of UFG AA6061 after 3 ECAP passes following aging treatment. We found that the aging treatment performed in section 3 highly influences the bulk electrochemical response in high chloride concentration and high dissolved oxygen. Also, pitting and filiform corrosion are two independent corrosion events.

Section 5 reports the effects of DRX, and peak-aging treatment on corrosion after 5 and 7 ECAP passes (near full recrystallization). We compared the hardness and the IGC resistance of the ECAPed material with those of conventionally extruded AA6061-T6 aluminum alloy. The higher the number of passes the higher the strength and the IGC resistance of the material even when compared with conventionally extruded AA6061-T6 aluminum. We explained these findings with the energy stored in the grains that seems to influence corrosion more than precipitation.

Section 6 provides some conclusions and future work to advance the understanding of the effects of ECAP processing on the localized corrosion of Al-Mg-Si alloys.

2. LITERATURE REVIEW

2.1 Aluminum and Aluminum Alloys

Aluminum (Al) is a chemical element from the Boron group (group 13 of the periodic table). It is the most abundant metal and the third most common element in the earth's crust[1]. Aluminum is a strong, conductive and light metal, with a theoretical density of 2.7 g/cm^3 (~ 3 times lower than carbon steel)[1].

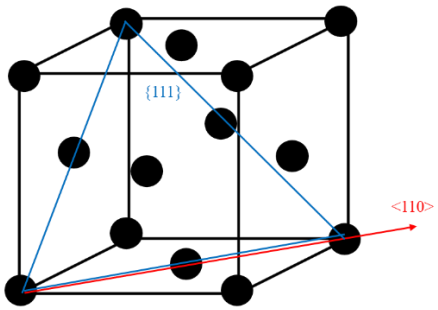

Figure 2: Aluminum FCC unit cell crystal showing atomic position, closed packed directions <110>, and closed packed plane {111}.

Pure aluminum has a face cubic center (FCC) crystallographic structure in which an atom sits at the center of each face (Fig. 2). FCC crystal has the highest packing density (74%), and the highest number of slip systems (12) which makes aluminum alloys more ductile than magnesium and titanium. Indeed hexagonal closed pack crystal possesses only 3 slip systems[2, 3]. In FCC crystal, primary slip occurs on the {111} plane along the <110> direction which correspond to the closed packed direction and plane of the crystal[2, 3] (Fig. 2).

Plastic deformation in single crystal involves primarily 2 modes of deformation: slip and twinning. Twinning is accommodated when there is not enough slip system to fulfil the plastic

deformation. It is mainly observed in crystal with law stacking fault energy (SFE). The SFE of aluminum is among the highest[2, 3] (~ 250 $mJ.s^{-2}$) therefore twinning is theoretically unexpected in coarse-grained aluminum. However in nanocrystalline (nc) aluminum, Yamako et al. predicted the occurrence of deformation twins by molecular dynamic simulations[4]. Subsequent experiments in nc aluminum films produced by physical vapor deposition[5] and nc aluminum produced by cryomilling[6] confirmed the MD predictions. Nucleation and growth of twins inside the grains and close to the grain boundaries were observed as well[5, 7]. It was attributed to grain size effects.

2.1.1 Al-Mg-Si Alloys - The 6xxx Aluminum Series

Pure aluminum is rarely used in engineering applications due to its relative low strength, and poor machinability. The mechanical, and physical properties of pure aluminum are improved through the addition of alloying elements, and subsequent heat treatment[8]. Thus, Mg, Si and Cu are added mainly in aluminum alloys from the 6xxx series (6061, 6060, 6063) to enhance the strength through precipitation hardening[9]. The aluminum grades that can be hardened through precipitation hardening are the 2xxx, 7xxx and 6xxx series. They are so-called age hardenable aluminum alloys. Precipitation hardening is a 3 steps process during which secondary hardening phases precipitate in the aluminum matrix through nucleation and growth to slow down dislocation motion[3, 9]. The combination of heat treatment temperature and time that maximize the strength of AA6061 is so-called T6 heat treatment or peak-aging treatment[10]. It consists of the following steps

- Solution treatment at 530 ˚C for about 3h: The aluminum alloy is held above the solvus temperature to dissolve all the precipitates until a single solid solution phase is obtained.

- Quenching: The single solid solution phase is rapidly cooled down to room temperature to obtain a non-equilibrium supersaturated solid solution, prevent diffusion, and the formation of Mg_2Si precipitates.
- Aging at 170 ˚C up to 10h. The supersaturated solid solution is heated long enough to allow diffusion and the precipitation of secondary hardening phases in the matrix (Fig. 3).

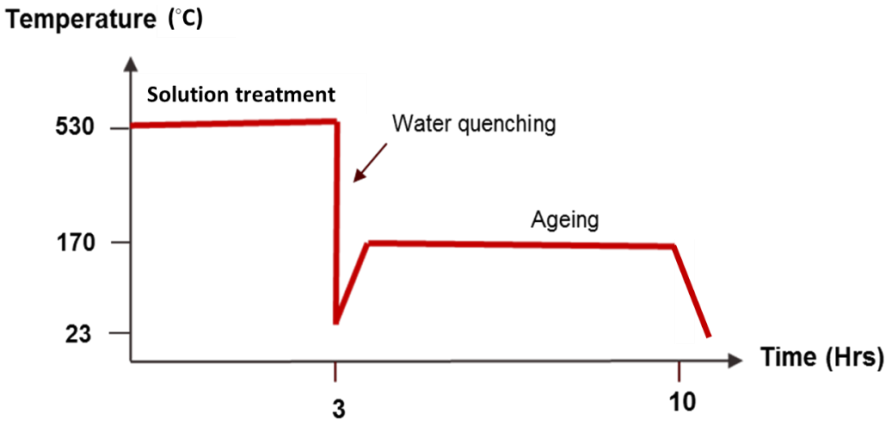

Figure 3: Schematic of T6 heat treatment procedure for aluminum 6XXX alloys.

The suggested precipitation sequence is the following[9, 11] : *Single clusters of Mg, and Si → co-clusters of Mg/Si → needle-shape β''(Mg_2Si) → rod-shape β'(Mg_2Si) → plate-shape β(Mg_2Si).* The β''(Mg_2Si) phase is the most predominant phase after peak-aging while the β(Mg_2Si) phase is predominate after over-aging[11]. In wrought AA6061, peak hardness (~100 HV) is reached after aging for 8h at 170 ˚C which corresponds to a ~40% increase in strength compare to the non-heat treated material (~ 65 HV)[10].

2.1.2 Aluminum Alloys

Aluminum alloys are an important family of material for the transportation industry because of its low density, and its good corrosion resistance[12, 13]. Indeed the 6xxx aluminum series

(Al-Mg-Si alloys) are mainly used in automobile, military vehicles, and equipment (e.g. AA6061, AA6063)[12]. The 5xxx series (Al-Mg alloys) is primarily found in naval vessels and ships structures (e.g. AA 5083) while the 7XXX series (Al-Zn-Cu alloys), and the 2XXX series (Al-Li-Cu alloys) are the main materials for aircraft structures (e.g., AA7075, AA2024)[13]. However aluminum alloys are not suitable for structures and applications where high strength is required. Indeed the 7XXX and 2XXX series; the strongest aluminum grades; exhibit a tensile strength and an ultimate tensile strength respectively of ~ 400 MPa and ~ 500 Mpa[8] which is ~ 3 times lower than those of steel (1500 MPa). In contrast for applications where strength is not required, the low IGC and stress-corrosion cracking of the 2XXX[14], 7XXX[15], and 5XXX[16] series is a problem because of their main alloying elements (Cu, Mg, and Zn).

2.2 Accumulative Roll Bonding

Accumulative Roll Bonding (ARB) is an intense plastic straining process during which ultra-fine grains materials (1μm< GZ < 100 nm) with high strength, and reasonable ductility[17, 18] are produced. The process consists of rolling two sheets stacked together after a pre-heat treatment. Between each rolling pass, the sheets are sectioned in half, and the rolling process is repeated[17-19] (Fig. 4). However, the maximum number of ARB cycle achievable (= maximum amount of strain to apply) is limited because of the reduction of the sheet cross section after each cycle. ARB was proved to improve the strength and the ductility of aluminum 5083 by 35% and 6% respectively[20]. Such increase in strength is attributed to the grain refinement, and the formation of a high density of dislocations during deformation. Several process parameters can be changed such as the rolls diameter, the rolling speed, the rolling temperature, the strain rate, and the number of rolling

passes[19]. They all affect the final microstructure of the material such as grain boundary density, grain boundary misorientation, and the shear bands network of the material[19-22].

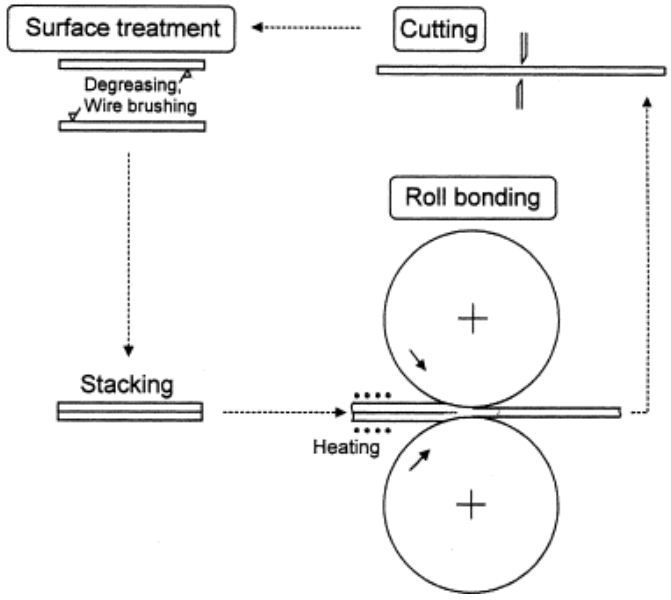

Figure 4: Principle of accumulate roll bonding (ARB). Reprinted with permission from Saito, Y., H. Utsunomiya, N. Tsuji, and T. Sakai. "Novel ultra-high straining process for bulk materials—development of the accumulative roll-bonding (ARB) process." Acta materialia 47, no. 2 (1999): 579-583.[18]

2.3 High Pressure Torsion

High pressure torsion (HPT) is a process by which a thin disc is subjected at the same time to a compressive force, and a torsional strain[23] (Fig. 5). It is capable of refining grain size down to 150 nm[24] which is smaller than what can be achieved through ECAP. Materials processed by HPT also exhibit high YS and TS due to the grain refinement, extensive precipitation (when HPT is combined with post-aging), and an increase in dislocation density[23, 24]. The final microstructure, which varies from the center to the edge of the disc is sensible to the processing parameters such as the imposed strain, the number of revolution, and the applied pressure[25].

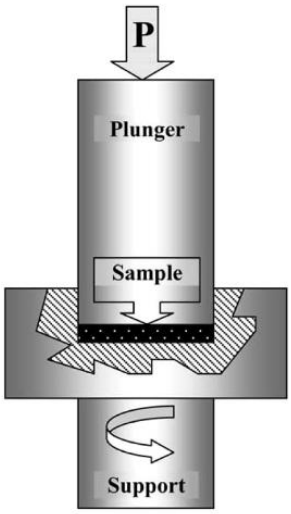

Figure 5: Principle of high pressure torsion (HPT). Reprinted with permission from Zhilyaev, A.P., Nurislamova, G.V., Kim, B.K., Baró, M.D., Szpunar, J.A. and Langdon, T.G., 2003. Experimental parameters influencing grain refinement and microstructural evolution during high-pressure torsion. Acta Materialia, 51(3), pp.753-765.[26]

2.4 Equal Channel Angular Pressing

Equal channel angular pressing (ECAP) is capable of producing ultra-fine grained aluminum alloys with improved mechanical properties, and thermal stability by shear deformation[27-29]. The technique consists of pressing a material through a die with a 90-degree angle without any change of its cross section at the exit (Fig. 6). Due to the die geometry, the material is subjected to a strain value of ~1 during each pass. Various texture and microstructure can be obtained depending on the number of passes and the billet rotation between them, which is dictated by the choice of extrusion route[30-32]. Four routes have been identified for the ECAP process (Fig. 6): Route A (no rotation of the bar after each pass), Route Bc (the bar is rotated by 90 degrees in the same direction around the X axis between each passes), Route E (the bar is rotated by +/- 90 degrees alternatively after each pass), Route C (the bar is rotated by 180 degrees after each pass)[28]. Route Bc was found to produce the most homogeneous, and fine microstructure for FCC metals

because of the high number of intercrossing slip systems on the X, Y and Z planes[28, 33]. Thus, it is the optimum processing route for UFG aluminum alloys.

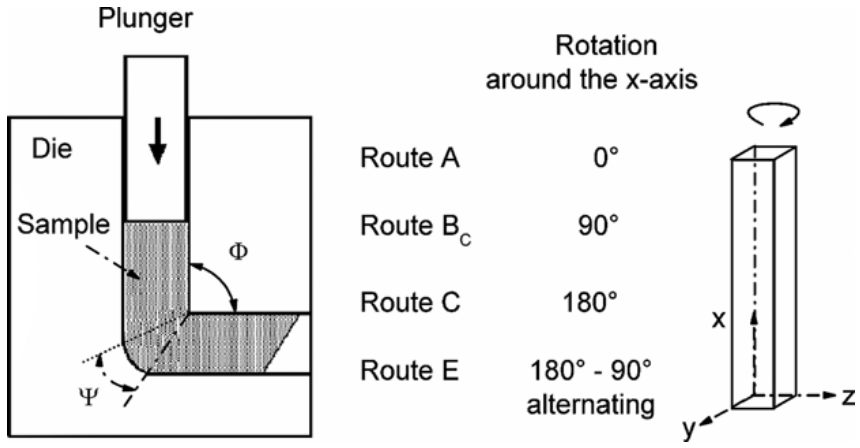

Figure 6: Principle of equal channel angular processing (ECAP). Illustration of the ECAP routes designations. Reprinted with permission from L. Kru¨ger, F. Schwarz, M. Mandel, M. Hockauf, Electrochemical corrosion studies of ultrafine-grained aluminium alloy EN AW-6063, Materials and Corrosion 2015, 66, No. 3.[34]

2.4.1 Dynamic Recrystallization and Shear Banding

Shear bands are narrow regions of localized plastic deformation and heat common in materials deformed at high strain rate including SPD processes[35, 36]. They are mainly made of elongated subgrains surrounded by low-angle boundary (misorientation < 15 degrees) which evolve to fine equiaxed grains with high-angle boundary when the strain increases[36-38]. Shear band formation was found to promote grain refinement during ECAP through a mechanism called dynamic recrystallization (DRX)[39] which has been extensively studied by Meyers et al.[40-42]. The proposed mechanism starts by the formation of a high density of dislocations during deformation that rearranges in low-energy dislocation cells (subgrains), then evolve to elongated subgrains[38]. The thermal energy stored in the shear bands may induce the rotation of the subgrain boundaries and the formation of fine equiaxed grains[40-42].

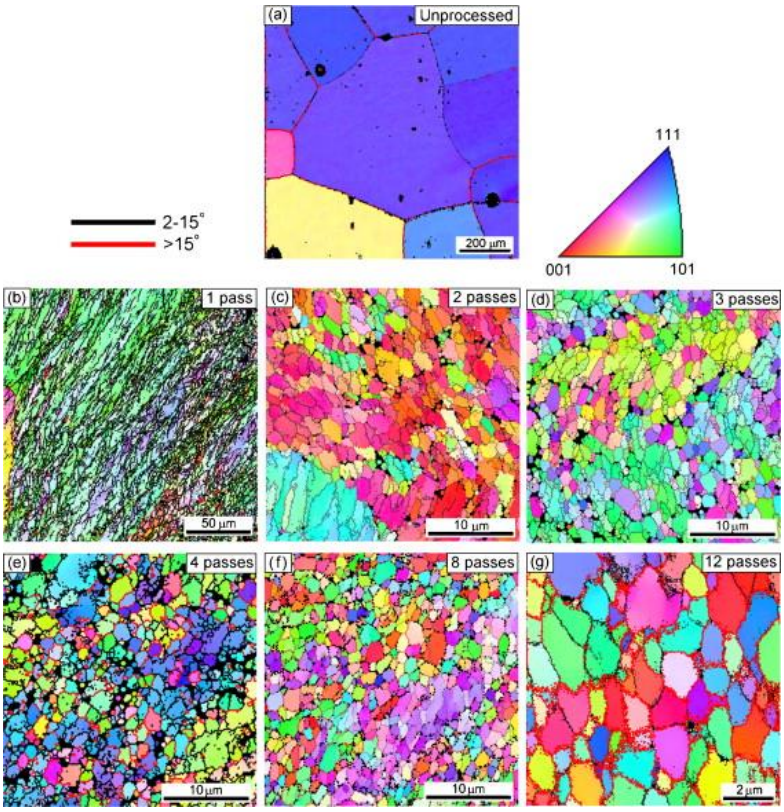

Figure 7: Microstructure and grain boundary misorientation evolution during ECAP. Reprinted with permission from Kawasaki, Megumi, Zenji Horita, and Terence G. Langdon. "Microstructural evolution in high purity aluminum processed by ECAP." Materials Science and Engineering: A 524, no. 1-2 (2009): 143-150.[38]

2.4.2 Dislocation Density, Grain Size, Grain Boundary Characteristics

Several studies investigated how dislocation density, grain size, and GB misorientation evolve with the number of ECAP passes following Route Bc[37, 43, 44]. It was found that the microstructure after 1 pass consists of elongated subgrains surrounded by LAGBs parallel to the shear direction (Fig. 7). After 2 passes, the average subgraing size, the aspect ratio of the elongated subgrains, and the fraction of LAGBs decrease while the dislocation density increases rapidly. After 4 passes the microstructure is composed of a mix of fine equiaxed grains and elongated subgrains surrounded by HAGBs and LAGBs[37, 38, 43] (Fig. 7). Between 4 and 8 passes the average cell size decreases further as well as the dislocation density and the fraction of HAGbs. The

microstructure at the end of this stage is near full recrystallization[37, 38, 43]. There is no significant change in the fraction of HAGBs and average grain size between 8 and 12 passes (Fig 7-10). They seem to reach a plateau although the fraction of recrystallized grains and dislocation density keep increasing. The microstructure is not fully recrystallized at the end of this stage[37, 38, 43].

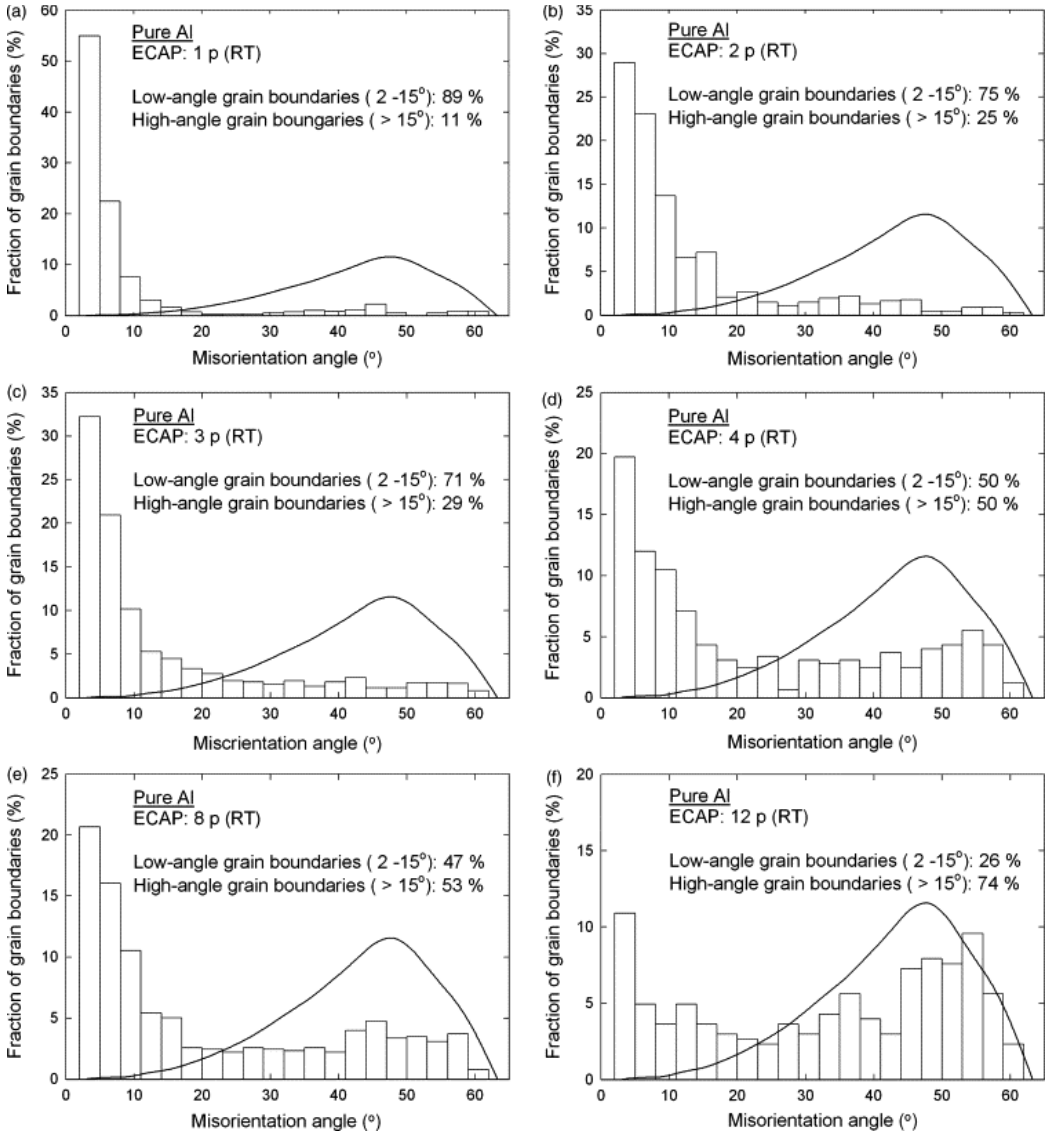

Figure 8: Schematic of the evolution of grain boundary misorientation in pure aluminum after ECAP following Route Bc. Reprinted with permission from Kawasaki, Megumi, Zenji Horita, and Terence G. Langdon. "Microstructural evolution in high purity aluminum processed by ECAP." Materials Science and Engineering: A 524, no. 1-2 (2009): 143-150.[38]

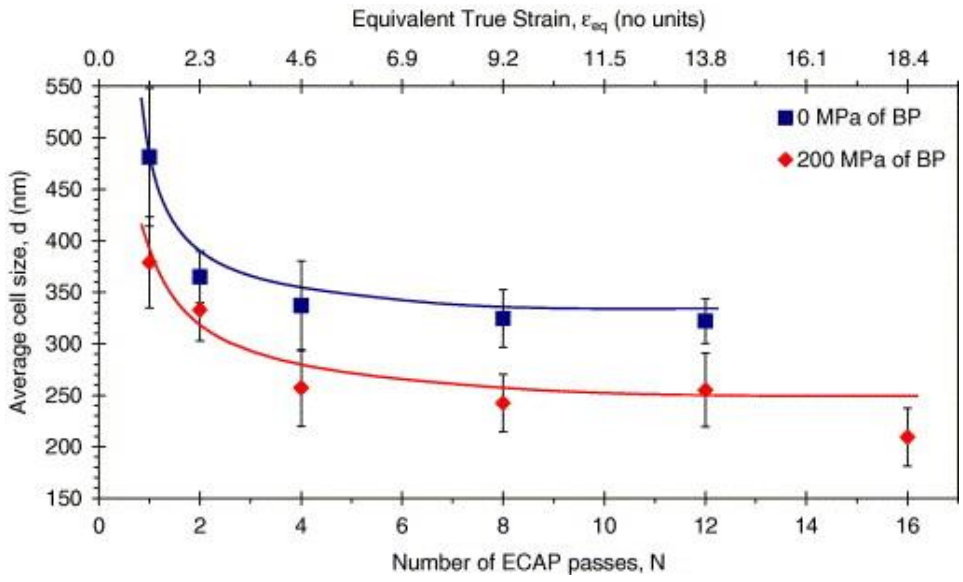

Figure 9: Modelling of the evolution of average cell size after ECAP with/without the use of backpressure (BP). Reprinted with permission from Mckenzie, P. W. J., Rimma Lapovok, and Y. Estrin. "The influence of back pressure on ECAP processed AA 6016: Modeling and experiment." Acta Materialia 55, no. 9 (2007): 2985-2993.[43]

2.4.3 Influence of Hydrostatic Pressure

Backpressure (BP) is used during ECAP processing to increase the number of passes (maximal amount of strain) and ultimately the grain refinement and the mechanical properties of the material[37, 43, 44]. McKenzi et al.[43] modelled the evolution of dislocation density in the cell interior, and the average cell size with the number of ECAP passes using a backpressure of 200 Mpa for an AA6016 aluminum alloy (Fig. 9 & 10). They found a good correlation between the use of hydrostatic pressure, the rapid increase in dislocation density, and the decrease in grain size (Fig. 9 & 10). Later Mogucheva et al.[37] found that hydrostactic pressure increases the hardness distribution in the material and the stress distribution during deformation. This results in a significant decrease of the amount of material wasted after each passes; an important criteria for commercial applications[37].

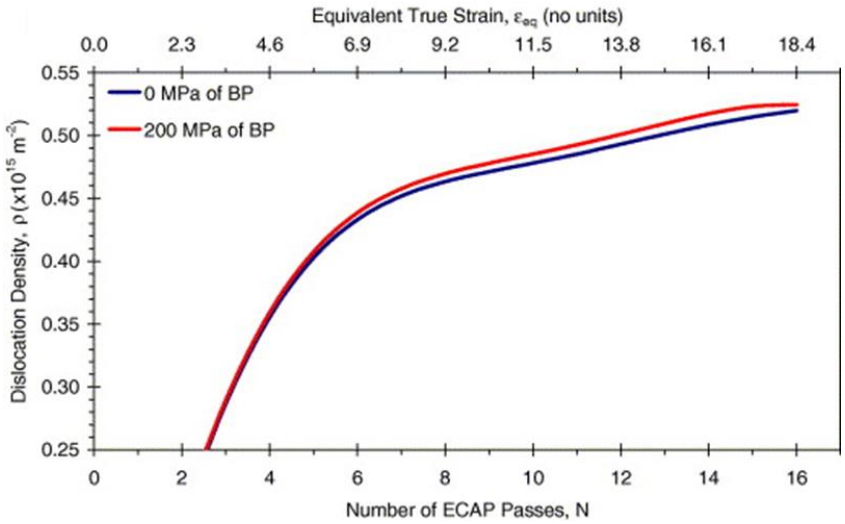

Figure 10: Evolution of dislocation density in the cell interior after ECAP with/without the use of backpressure (BP). Reprinted with permission from Mckenzie, P. W. J., Rimma Lapovok, and Y. Estrin. "The influence of back pressure on ECAP processed AA 6016: Modeling and experiment." Acta Materialia 55, no. 9 (2007): 2985-2993.[43]

2.5 Ultra-Fine Grained Aluminum Alloys 6xxx

2.5.1 Dynamic Precipitation

In pure aluminum strengthening following ECAP was attributed to the grain refinement as a result of the Hall-Petch law[45], and the formation of a high density of dislocation. For aluminum alloys, there is an additional contribution of the intermetallic compounds, and the hardening precipitates initially present in the material[29] which act as barriers to dislocations motion. Roven et al.[46] found in Al-Mg-Si alloys that spherical β" (Mg_2Si) precipitates formed during deformation even when the material is extruded in solution heat treated condition at room temperature. Similar metastable β" (Mg_2Si) precipitates was found earlier by Cabibbo et al. in an AA6082 alloy extruded at room temperature[11]. This was explained by a dislocation assisted mechanism called dynamic precipitation[46, 47]. It was suggested that precipitation is promoted by the high density of dislocations (preferred sites for precipitation) generated during the plastic deformation (figure 11).

Therefore strengthening in as-ECAPed Al-Mg-Si results from the grain refinement (Hall Petch law), and the metastable β" (Mg_2Si) precipitates (Orowan law)[11].

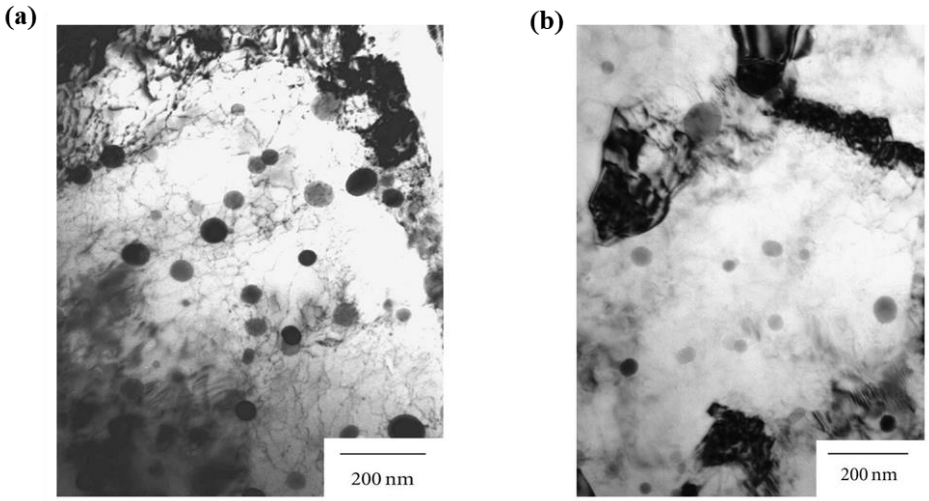

Figure 11: TEM images of spherical/globular Mg_2Si precipitates in an AA6082 alloy (a) After 1 ECAP pass (b) after 6 ECAP passes. Reprinted with permission from G. Angella, P. Bassani, A. Tuissi, and M. Vedani, "Aging behaviour and mechanical properties of a solution treated and ECAP processed 6082 alloy," *Materials Transactions*, vol. 45, no. 7, pp. 2282–2287, 2004[47]

2.5.2 Influence of Aging Treatment

Several combinations of ECAP processing and aging treatment have been investigated in the literature to maximize the mechanical properties of ECAPed aluminum alloys. Ferrasse et al.[48] first investigated the effects of a pre-ECAP aging treatment at 170 ˚C up to 8h on the strength of an AA6061 aluminum alloy. The study found that such a pre-aging treatment leads to a more homogeneous and finer microstructure. It also increases both the strength and the ductility of the material[48]. Reasons are the small precipitates formed during the pre-aging treatment that prevent grain growth by pinning the GB while acting as a more effective barrier to dislocation motion than the dislocations itself. Later Kim et al.[49] found that a low-temperature post-ECAP aging treatment at 100 ˚C is more effective than the pre-ECAP aging treatment in strengthening AA6061 aluminum

alloys. Indeed, the largest increase in yield strength (425 MPa) and ultimate tensile strength (460 MPa) was obtained after 6 passes and a post-aging treatment at 100 ˚C for 2 days (~ 8% of ductility)[49]. It is 40% higher than the UTS of the unprocessed material (~ 250 Mpa). This is explained by the formation of fine precipitates (~ 20 - 40 nm) especially at the dislocations generated during ECAP. Indeed, they enhanced precipitation kinetics by decreasing the peak aging temperature from 170 ˚C to 100 ˚C, and by suppressing recovery[49, 50]. The study also found that the common needle-shaped β"(Mg_2Si) and lathe-shaped β'(Mg_2Si) precipitates found in cast AA6061 after peak-aging are replaced by globular/cluster Mg_2Si after ECAP due to higher GB diffusion rate[49, 50].

2.5.3 Fragmentation of Precipitates and Particles

Several studies investigated the particles evolution (IMCs, hardening precipitates) during ECAP processing. As a general conclusion, ECAP is effective to break the precipitates into fine particles through shearing and to homogeneously distribute them in the matrix[11, 24, 51, 52]. This leads to additional strengthening through particle/dislocation interaction[11] as they are more effective obstacles to dislocation motion than the dislocation itself. Particle fragmentation during ECAP was reported for Mg_2Si precipitates and AlFeSi IMCs in AA6082 alloys[11], for Al_2Cu precipitates[53] in AA2024 alloys and $MgZn_2$ precipitates in AA7050 alloys[54]. Indeed when the material is extruded following Route C, the particles rearrange along the extrusion direction at the beginning of the deformation before being homogeneously redistributed in the matrix[11] while for Route Bc, they rearrange along the shear direction.

2.6 Corrosion Mechanisms in Aluminum Alloys

2.6.1 Passivation

The superior corrosion resistance of aluminum alloys is due to their natural tendency to form an aluminum oxide film (1~ 3 nm thick) at their surface that greatly acts as barrier protection for corrosion. Passive films mechanism and kinetic growth models were first proposed in the 30s by Verwey[55]. It was suggested that film growth kinetic is controlled by cations exchange within the passive film that use an electric field as a driving force. This theory known as high field model (HFM) was later modified by Mott Cabera[56, 57] who suggested that the cations exchange does not occur within the passive film. Instead, the cations, after being released by the metal transfer to the film at the metal/passive film interface. In the '80s MacDonald et al.[58-60] published a series of paper on a new mechanism called point defect model (PDM) which involved metal/electrolyte interactions. In addition to the cation/cation transfer at the metal/passive film interface, the PDM model included cation/anion/vacancies transfers and mobility between the electrolyte and the metal. However the passive film of aluminum alloys is not fully protective and resistant to chloride ions in particular. It can be susceptible to localized breakdown that results in pits formation, and the anodic dissolution of the aluminum matrix[60].

2.6.2 Pitting and Passivation Breakdown

Pitting is the most dangerous and common form of localized corrosion in aluminum alloys. It is an autocatalytic process impossible to predict and monitor due to the stochastic nature of the phenomenon[61]. Pit growth mechanisms in aluminum alloy, in particular, have been extensively studied by Frankel and al.[62]. Although pitting has been investigated for many decades, the mechanisms for passive film breakdown and pit growth are still not well understood. Three main

models have been proposed to explain passive film breakdown when exposed to Cl-rich electrolyte[61]: The first one suggests that pitting starts by the adsorption, the penetration, and the transport of Cl^- ions in the passive film[63, 64]. The second model suggests a competitive adsorption mechanism of Cl^- and $O2^-$ in the passive film which promotes the release of metal ions into the electrolyte[65-67]. The third one suggests that the passive film breaks because of mechanical stress due to an excess of pressure within the film following the adsorption of aggressive ions[68, 69]. Nevertheless, it is well accepted that pitting occurs[62] in 3 steps:

- Pits nucleation or initiation as a result of passive film breakdown after adsorption of aggressive ions (Cl^-) at the film interface.
- Metastable pits propagation and growth, characteristic of pits which, nucleate and grow to a certain size for a limited amount of time, and repassivate.
- Stable pits propagation and growth as long as the pit environment and pit interior are acidic enough to keep consuming the surrounding aluminum matrix.

Pits formation results from an electrochemical reaction between the metal and the oxygen dissolved in water; the two main anodic and cathodic reactions[70]. It is followed by the precipitation of aluminum hydroxides; the main corrosion products found inside and at the vicinity of the pits[70]. These processes[70] can be summarized as the following:

Anodic reaction: $Al \rightarrow Al^{3+} + 3e^-$

Cathodic reaction: $O_2 + 2H_2O + 4e^- \rightarrow 4OH^-$

Precipitation: $Al^{3+} + 3H_2O \rightarrow Al(OH)_3 + 3H^+$

The most common technique to assess the pitting corrosion susceptibility of a material is polarization measurement during which either the material's potential (E) or the current flow (I)

are monitored[71]. The breakdown potential (E_{pit}) derived from the E = f(I) curve is generally used as criteria to screen the stability of a passive film, and the ability of a material to form stable pits at its surface[62]. Stable pits form at potentials more active than E_{pit} and grow at potentials more active than the repassivation potential (E_{rep}). These two potentials are measured during cyclic potentiodynamic polarization testing when the potential or current are monitored while the sample is polarized[70]. Besides, the difference between E_{rep} and E_{pit}, which represents the size of the hysteresis loop, indicates the ability of the pits to repassivate. In other words, higher pitting and repassivation potentials suggest lower susceptibility to pitting, however, this rule should be used with caution because of the stochastic nature of the phenomena and the sensibility of these potentials to material inhomogeneity, the scan rate, and the chloride concentration[62].

2.6.3 Influence of Alloying Elements

In aluminum alloys, pitting corrosion generally occurs at the vicinity of the precipitates, and the intermetallic compounds (IMCs)[72]. However, aluminum is one of the most reactive elements of the EMF series, followed by Mg and Zn[73]. Therefore any cathodic Fe, Si, Cu-rich particles in the aluminum matrix will favor its dissolution while any anodic Mg, Zn-rich particles will dissolve in favor of the aluminum matrix[72, 74]. The formation of IMCs compound is the primary cause for passive film breakdown in aluminum alloys. For instance, in the 6XXX series, Al-Fe-Si IMCs are preferential sites for pits formation due to their Fe content[72]. However anodic phases can lead to pits nucleation and growth as well. This is the case for the S-phase (Al_2CuMg) in Al 2024-T3[75]. The mechanism starts with dealloying of Mg and Al leaving cathodic Cu-rich precipitates in the matrix. The occurrence and severity of pitting corrosion is influenced by the size and spacing

of the precipitates. Indeed it was found that precipitates smaller than a critical size limit don't induce pitting while larger precipitates do[76].

2.6.4 Intergranular Corrosion

Intergranular corrosion (IGC) is the second form of localized corrosion in aluminum alloys during which the grain boundary chemistry is electrochemically different from the surrounding matrix[77]. IGC mainly occurs following precipitation hardening[78] or sensitization treatment[79] during which GB precipitation occurs leading to micro-galvanic cells and precipitates free zones (PFZ)[80] at the vicinity of the GB. For instance in Al-Cu alloys (2xxx series) cathodic Al_2Cu precipitates form during aging treatment at the GB while anodic β-phase (Al_2Mg_3)[78] precipitates form in Al-Mg alloys during sensitization. However, the IGC resistance of aluminum alloys is usually improved by optimizing the heat treatment temperature and time which can alter the mechanical properties of the material.

Aluminum alloys from the 6xxx series are mostly susceptible to IGC in their extruded form after aging treatment because of its GB characteristics (HAGBs) and the formation of PFZ[80]. However their susceptibility to IGC can be reduced by optimizing the amount of Cu and Mg/Si ratio[81-83] in the material in addition of optimizing the heat treatment conditions[84, 85].

2.7 Corrosion Susceptibility of Ultra-Fine Grained Aluminum Alloys

2.7.1 Effects of SPD on Grain Size

We mentioned in the previous sections that SPD processes induce several microstructural changes in the material regarding grain size distribution, GB density and misorientation, residual stress, and dislocation density. Although most of the studies found that SPD decreases the anodic corrosion current density of aluminum alloys above E_{pit}[86-92] couple groups either found that the

Table 1: Literature review: Influence of SPD processes on the corrosion susceptibility of pure aluminum

	Processing	Testing Environment	E_{corr}	E_{pit}	Rp	anodic current density	Reference
Pure Aluminum	Al 1050, ARB, 9 passes, RT	0.3 M H_3BO_3 + 0.001 M $Na_2B_4O_7$	x	increase	increase	decrease	[86]
	AA1050,annealing at 370 ◦C for 7200 s ARB 9 passes RT	0.3 M H_3BO_3 + 0.1 M NaOH	x	increase	increase	decrease	[87]
	Al-5,4 wt% Ni Al-5wt% Cu ECAP 6 passes RT Route Bc 33 mm/s	0,075 M $Na_2B_4O_7$ + 0,3M H_3BO_3 + 0,002M NaCl	decrease	decrease	x	x	[88]
	ECAP, 16 passes 0.5 mm/s, RT	0,01 mol/L Na_2SO_4 + 3,5% NaCl	decrease	increase	increase	decrease	[89]
	AA1050, ECAP, RT Route Bc, 16	natural sea water	decrease	decrease	increase	decrease	[90]
	Al 1100 , ECAP 8 passes, Route Bc	0,1 M/L Na_2SO_4 + 8,46 mmol NaCl	increase	increase	increase	unaffected	[93]
	AA1050, Rolling + ECAP, 5 passes	0,1 M Na_2SO_4 + 100 ppm Cl-	unaffected	increase	increase	decrease	[91]

anodic current density is unaffected[34, 93, 94] or increase[95] after SPD even for the same material processed by the technique (cf. Table 1 and 2). A similar observation is made for the polarization resistance Rp, used to assess passive film resistance under a small sinusoidal perturbation (+/- 10 mV). Some groups found that Rp increase after ECAP[86, 87, 89-91, 93, 96] while others found a decrease in Rp with SPD. The most controversial results exist for the pitting potential (E_{pit}) and the corrosion potential (E_{corr}). There is no general agreement on the evolution of E_{corr} and E_{pit} with SPD. A possible reason is the sensibility of the final microstructure to processes parameters (especially the extrusion speed), the initial state of the material (T6 condition or after solution heat treated), the number of passes, and the initial amount of IMCs. For instance some studied used an extrusion

speed of 0.5 mm/sec[89] others 25 mm/sec[96] and 50 mm/sec[34]. However, the extrusion speed is known to influence strain localization, DRX and therefore localized corrosion[97]. Also, the choice

Table 2: Literature review: Influence of SPD processes on the corrosion susceptibility of aluminum alloys

Alloys	Processing route	Testing Environment	E_{corr}	E_{pit}	Rp	anodic current density	Reference
Al-Si	Room temperature HPT 1/4, 1/2, 1, 10 revolutions	3,5 wt% NaCl	increase	increase	increase	decrease	[92]
Al-Mg-Si	Annealing 500 ◦C for 24 hours ECAP RT 5 passes Route A	3 wt% NaCl	unaffceted	increase	unaffected	x	[97]
	AA6082- T6 - ECAP RT 8 passes, Route E 25 mm/min	0,1 M NaCl	increase	increase	increase	x	[98]
	AA6063, ECAP, RT 6 passes, Route E 50 mm/min, Aging at 170°C for 23 min	0,01 M NaCl	unaffected	unaffected	x	unaffected	[95]
Al-Cu-Li	AA2024 ECAP at RT 4 passes, Route Bc	0,5 mol/L NaCl	unaffected		x	unaffected	[94]
Al-Mn	Anneling at 573 K for 1hr ARB at RT , 5 passes	3,5 wt% NaCl	increase	x	x	increase	[96]
Al-Mg	ECAP , 12 passes, Route Bc	0.1 M NaCl 0.01M NaCl	x	unaffected	unaffected	unaffected	[99]

of ECAP route affects the shape of the grains (equiaxed grains, lamellar, mixed) and the shear bands network of the material[28, 29]. Table 1 and 2 show that some studies extruded the material following Route Bc[87, 88, 90, 95] others Route E[34, 96] and Route A[98]. Besides, the maximum number of passes achieved combined with the choice of ECAP Route influence the homogeneity of the material regarding GB characteristics (HAGBs, LAGBs) and particles distribution as discussed earlier. For example, some studies assessed the corrosion susceptibility of the material after 4 passes[94] other up 12 passes[99] and 16 passes[89]. In other words, the intrinsic length scales (grain boundary, precipitates, IMC, dislocations) introduced in UFG materials after SPD, and the large

freedom of processing routes offered by these techniques make the characterization of their corrosion behavior complex.

2.7.2 Effects of SPD on Passivity

The effects of SPD processes on the stability and characteristics of the passive film was assessed by potentiodynamic polarization, and electrochemical impedance spectroscopy in the literature[90, 92, 100 96]. Some groups did not find a change in passivation behavior following SPD processes[94] while others found that the passive film of UFG aluminum alloy is thicker, more adherent, and more resistance after processing. The latter conclusion was made after reporting higher values of polarization resistance (Rp), lower passive current density and higher breakdown potential (E_{pit})[92, 101, 102] following ECAP . Such enhancement of passivation behavior was attributed to:

1) The fragmentation of particles (IMCs, precipitates) during SPD below a critical size[76] which leads to smaller microgalvanic cells in the matrix.

2) The lower surface electron work function (EWF) of UFG materials compare to their coarse grains counterpart materials. Indeed it was reported for an aluminum 2099 alloy that SPD processes decrease the surface EWF because of the grain refinement[102]. Also, low surface EWF is associated to higher surface activity which could enhance the ability of the material to passivate[102].

3) Higher oxygen adsorption due to the high density of defects generated in the material after SPD. Indeed diffusion is known to be faster on defects (dislocations, particles, grain boundaries) than in the bulk[103]. Therefore the increase of oxygen diffusion kinetics in UFG may promote the formation of a thicker and more stable passive film[101, 102]. However, Bruner et al. measured by XPS the atomic concentration of oxygen in the passive film of an Al-Mg alloy processed by ECAP.

The results reveal same oxygen atomic concentration for the coarse grain material and the one processed by ECAP which results in a similar thickness of the passive films[99].

2.7.3 Effects of ECAP on Pitting Corrosion

Pitting in aluminum alloys is greatly affected by the size and spacing of the IMCs. The larger and closer the IMCs the larger the pits. The reason is the size of the microgalvanic cells formed between the cathodic IMCs and the aluminum matrix. In Al-Mg-Si aluminum alloys, the main IMCs; preferred sites for pitting; are the α-AlFeSi and β-AlFeSi phases[98]. Several studies reported a change in the pitting attack from a low density of deep pits to a high density of less deep pits following ECAP[34, 96,101] attributed to the fragmentation of IMCs during processing[11, 51, 104]. The corrosion attack morphology is mainly characterized by pits with [111] facets surrounded by filiform corrosion[94, 97] along the shear direction also reported as "crystallographic pits (Fig. 12).

2.7.4 Effects of Grain Boundary Misorientation

EBSD[37, 38], XRD[51] and 3D-APT[99] are three common techniques used in the field of GB engineering to investigate GB misorientation, grain texture, and grain size distribution. These techniques were used to investigate how SPD processes change GB misorientation from low angle boundary (LAGB) (misorientation< 15 degrees) to high angle boundary (HAGB) (misorientation >15 degrees)[37, 38] when the strain increases. HAGBs are more susceptible to precipitation than LAGBs because of their high GB energy. The use of coincidence site lattice (CSL) approach also demonstrated that they are more prone to IGC in an AA5083 aluminum alloy after ECAP where precipitation of thick β (Mg_2Al_3) phase in conjunction with higher degree of sensitization (DOS) were found at the HAGBs[105]. Enhanced IGC susceptibility was also reported for conventionally extruded AA6061-T6. It was attributed to the formation of precipitates free zone, and GB

precipitates at the HAGB[80]. In contrast coherent twin boundaries (Σ3 and Σ7) having low misorientation (LAGBs) were found to be the most resistant to IGC[106-108]. A recent study confirmed the link between thin β precipitates, low DOS and a high fraction of low grain boundary (Σ<29) in an Al-Mg alloy[109]. As a result the higher the GB misorientation, the higher the susceptibility to GB precipitation and IGC.

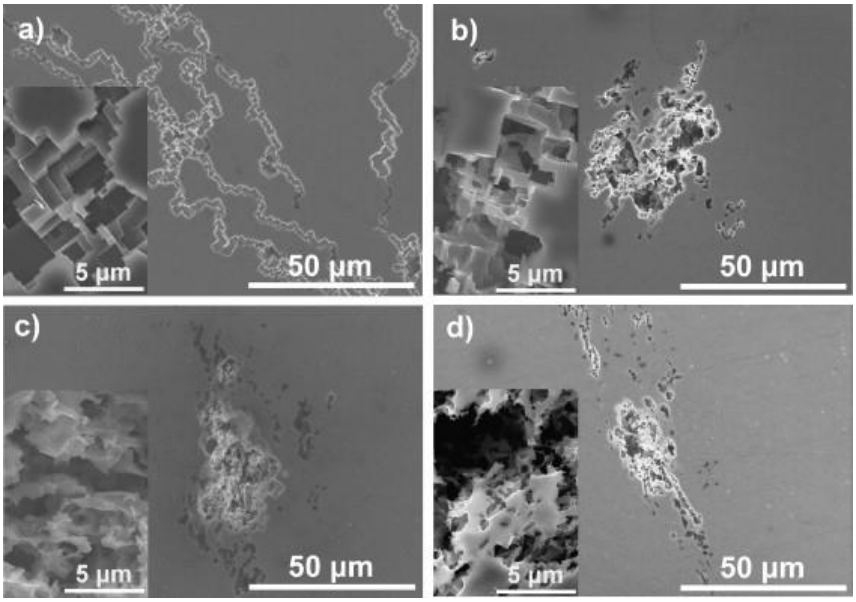

Figure 12: SEM images showing the effects of the number of ECAP passes following route Bc on the pits morphology of an AlMg alloy after potentiodynamic polarization in 0.1 M NaCl (a) CG state, (b) 4 passes, (c) 8 passes and (d) 12 passes. Reprinted with permission from Brunner, J. G., J. May, H. W. Höppel, M. Göken, and S. Virtanen. "Localized corrosion of ultrafine-grained Al–Mg model alloys." Electrochimica Acta 55, no. 6 (2010): 1966-1970.[94]

2.7.5 Effects of Grain Stored Energy

Several groups reported corrosion at GB with no evidence of GB precipitates. Indeed, in an AA2024-T3 aluminum alloy, GB and grain interior dissolution were observed in isolated grains not decorated with Θ phase (Al_2Cu)[110]. However the surrounding grain exhibits a high dislocation

density (associated to a high stored energy), suggesting a correlation between grain-stored energy, thermodynamic instability and IGC[110-114].

2.7.6 Effects of Residual Stress and Strain Localization

Residual stress was reported to affect the integrity of the passive film, the metal-free energy and the electron work function[115] (EWF). EWF is by definition the minimum energy required to remove an electron from a solid surface in vacuum[116]. It can be measured by scanning Kelvin probe (SKP) or indirectly assessed by Volta potential difference (VPD) measurements using the scanning Kelvin probe force microscopy (SKPFM) technique[117]. EWF is affected by changes in

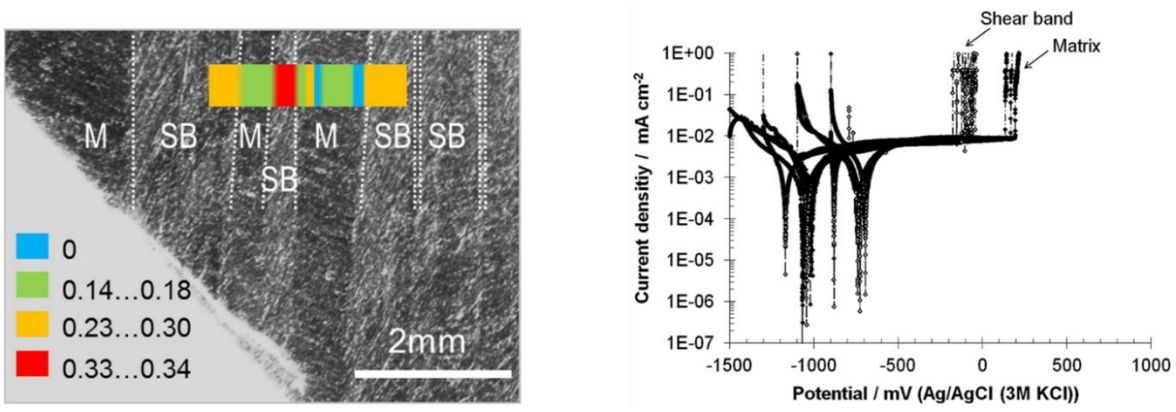

Figure 13: (a) Local micro strain distribution in an AlMgSi0.5 alloy after 1 ECAP pass. M = Matrix, SB = Shear Bands. (b) Potentiodynamic polarization curve of the shear bands and the matrix in an aerated 0.1M NaCl solution. Reprinted with permission from Nickel, Daniela, et al. "Effect of strain localization on pitting corrosion of an AlMgSi0. 5 alloy." Metals 5.1 (2015): 172-191.[97]

the crystal structure (bond length, lattice distortion)[115,118] induced by the introduction of compressive or tensile stresses in the material surface. This is the case for SPD processes such as HPT, ARB, and ECAP after which some residual strain, highly localized within the shear bands, remains in the material. Nickel et al. [97] investigated the interaction between strain localization and

pitting in an UFG Al-Mg-Si alloy by local strain measurements and local electrochemical testing. The results revealed enhanced pitting susceptibility in regions of high residual strain. These regions coexist with the shear bands (Fig. 13) of the material confirming that strain localization and shear banding disrupt passive film stability[97, 119].

2.8 Application of Ultra-Fine Grained Aluminum Alloys

Conductive aluminum wires are generally made of Al-Mg-Si alloys by cold drawing as they exhibit the highest strength/electrical conductivity balance. In metallic materials, strength and electrical conductivity are mutually exclusive properties. Indeed the defects introduced in the microstructure to increase the strength are somehow detrimental to electron scattering, responsible for the electrical conductivity. However ARB[120] and HPT[121, 122] were proved to produce nanostructured Al-Mg-Si alloys with enhanced electrical conductivity and strength through grain refinement, and the precipitation of nanosized Mg_2Si precipitates in the matrix.

3. EFFECTS OF STRAIN LOCALIZATION ON THE CORROSION BEHAVIOR OF ULTRA- FINE GRAINED ALUMINUM ALLOY AA6061*

3.1 Introduction

It has been nearly three decades since the emergence of severe plastic deformation techniques (SPD) have progressed as a viable approach for grain refinement and the development of a good combination of strength, ductility, and thermal stability in metal alloys[29, 123]. Although the influence of SPD processes on microstructure and mechanical properties has been extensively studied, there remain many uncertainties and controversial results regarding the corrosion resistance of such processed metals[112, 114, 124, 125]. Indeed the main challenges in this area of research are the sensitivity of the final microstructure to process conditions (temperature, pressing speed, and aging time/temperature) combined with the large number of processing routes inherent to these SPD techniques[121]. Also, the intrinsic length and size scales (grain boundary area, dislocation density, precipitate morphology, and distribution), helpful for strengthening and grain refinement, add complexity to the understanding of corrosion mechanisms.

In this study we investigate the influence of a particular feature, often disregarded in corrosion studies: adiabatic shear bands. Shear banding is a dominant plastic deformation mechanism for grain refinement in high strain deformation processes such as ball milling, shot peening, wire drawing, high compression tests[23], and equal channel angular pressing (ECAP)[126]. The resulting microstructure is often composed of a high density of micro shear bands which are

* Reprinted with permission from "Effects of strain localization on the corrosion behavior of ultra-fine grained aluminum alloy AA6061." by Ly, Ramatou, Karl T. Hartwig, and Homero Castaneda. 2018, *Corrosion Science,* 139, pp. 47-57, Copyright 2019 by ELSEVIER.

helpful for recrystallization[127]. More importantly, these bands are regions of high strain localization and transient adiabatic heat, with a complicated thermomechanical history. Strain localization and plastic deformation are critical factors in corrosion. They have been reported to affect surface roughness and passive film thickness, known to control localized corrosion susceptibility[115]. Pitting and intergranular corrosion (IGC) are the two main types of localized corrosion in aluminum alloys. In general, pitting results from the breakdown of the passive film around particles in contact with a chloride-rich environment[62, 126]. IGC is a different form of localized attack adjacent or along the grain boundaries (GBs), due to the chemical segregation of particles at the GB either more or less noble than the matrix[77]. These two forms of corrosion, governed by heat treatment parameters and alloying elements[84, 128], make strengthening of aluminum alloys challenging if the goal is also corrosion resistance.

ECAP is a widely-known SPD process for producing ultra-fine grained (UFG) materials by shear deformation[23, 129] without significant change in the workpiece cross-section. The technique consists of pressing a bar through a die with a 90-degree angle by introducing a high strain in the material as it passes through the die. It has the capability to considerably enhance the strength of aluminum 6xxx alloys when combined with low temperature aging[50]. The literature on how strain localization, through shear band formation, affects the corrosion susceptibility of nanostructured aluminum is insufficient. However, in processes such as ECAP, shear bands can cover up to 60% of the overall microstructure after a plastic strain of 4-5 and persist at even higher strains (8-10)[37, 38, 130]. Also, their width, length, and number are highly influenced by the processing routes or strain history[127]. Most of the relevant studies that have dealt with the effects of SPD processes on localized corrosion of aluminum alloys have involved shear band formation without considering them in their research[94, 96, 98, 114, 125]. Raltson et al. in their review, “Effect of grain size

on corrosion"[124] pointed out the limited literature on the combined effects of residual stress and segregation with grain size. To the best of our knowledge, since then there has been only one paper that studied the influence of strain localization on aluminum alloy corrosion susceptibility after ECAP. The study was conducted by doing local electrochemical testing and local strain measurements[97]. Enhanced pitting susceptibility was found in the shear bands and attributed to the high strain localization in that region. However, the band structures were not investigated in sufficient detail to relate their enhanced reactivity to internal microstructure heterogeneities.

Here we investigate the combined influence of grain size, residual stress and chemical segregation with detailed microstructure characterizations. The alloy under study is aluminum alloy AA6061 processed by ECAP after three passes following Route Bc (90-degree rotation between all passes). This processing route provides the most heterogeneous microstructure (high fraction of intercrossed shear bands) and therefore gives an easy route to shear band generation. Our results show redistribution of the AlFeSi intermetallic compounds (IMCs) along the shear direction (SD) and the shear plane of the material making that direction highly susceptible to pitting. We also show preferential precipitation of cathodic and anodic precipitates within the bands, when ECAP is combined with aging, making the bands preferred regions for pitting and intergranular corrosion.

3.2 Experimental Procedure

3.2.1 Materials and Processing

Commercially wrougth AA6061 (0.6wt% Si, 0.9wt% Mg, 0.35wt% Cu, 0.7wt% Fe, 0.08wt% Mn) aluminum bars of 178 mm length by 25.4 mm x 25.4 mm area were used in this study. The bars were initially homogenized at 530 ˚C for three hours in air; water quenched then

extruded in a sliding wall ECAP die with a 90-degree internal angle, 30 minutes after quenching. A maximum of three passes was achieved at room temperature and a pressing speed of 5 mm/sec following Route Bc (90-degree rotation between passes). 24 hours after processing, the bars were aged at 100 ˚C for up to four days. One was kept in the as-extruded conditions for corrosion testing.

3.2.2 Vickers Hardness

Vickers hardness measurements were taken on the plane normal to the extrusion direction (ED) as indicated in Fig. 14. Before measurement, the material surface was polished with silicon carbide (SiC) paper up to grade 1200. The hardness was measured by applying a load of 1 N for ten seconds with a diamond indenter at ten different locations and taking the average.

3.2.3 Microstructure Analyses

Electron backscattered diffraction (EBSD) was used in this study to assess the grain size and the grain boundary misorientation after processing. The analysis was carried out with a TESCAN FERA 3 MODEL scanning electron microscope (SEM) equipped with an Oxford instrument EBSD detector and Aztech V3.3 software. The data were acquired with a step size of 100 nm and an accelerating voltage of 20 kV. HKL channel 5 software was used for EBSD post processing and grain boundary misorientation measurements. A threshold of 5˚ was set for the measurement. X-ray diffraction analyses were performed with CuKα radiation (40 kV, 25 mA) and a Bruker-AXS D8 Advanced X-ray Powder Diffractometer in the range of 2Θ = 30˚ to 90˚. Composition profile analyses were carried out by Time-of-Flight secondary ion mass spectrometry (ToF-SIMS) with a CAMECA IMS 4f detector. A 250 x 250 μm^2 surface area was bombarded with a positive O^2 ion beam (5.5 KeV, 1.2 10^{-6} A) which corresponds to a sputtering rate of 14 nm/sec. The pressure inside the chamber was maintained at 10^{-5} Pa during the analysis. Ion-spec

commercial software was used for the image acquisition. A BRUCKER dimension Icon AFM was used to investigate precipitate morphology and element distribution with an SCM-Pit probe (25 nm radius). Volta potential differences were measured with respect to the SCM-Pit probe by the scanning Kelvin probe force microscope technique (SKPFM). All SKPFM measurements and AFM topography maps were acquired simultaneously in ambient air (with no particular control of the humidity) and at ambient temperature (23 degrees). A lift scan height of 40 nm was used for the measurements. All the microstructure analyses were performed on a surface polished with SiC paper up to grade 1200, alumina diamond suspension up to 1 micron, and a water-free colloidal silica suspension (0.05 μm). The surface was then cleaned and degreased in an ultrasonic bath.

3.2.4 Corrosion Immersion Tests

To assess the IGC susceptibility of the materials after processing and aging, we used the accelerated standard ISO 11846 (Method B) test. Before testing, the material was etched in 5% NaOH at 60 ˚C for 3 minutes then desmuted in 60% NH3 for 2 minutes to reveal the grain boundaries. For that, a square of 1 cm^2 was cut from the center of the bar (as indicated in Fig. 14) to ensure material homogeneity and avoid the existence of cracks. The material was then mounted, polished using SiC paper up to grade 1200, and aluminum diamond suspension up to 1 μm, and then cleaned and immersed in the testing solution (30 g NaCl/L and 10 ml HCl/L, pH ~1) for 24 hours. The extent of IGC was assessed by investigating each material cross-section under the optical microscope. To capture the evolution of the IGC, samples were immersed in the testing solution in parallel, and removed after 5 hours for observation.

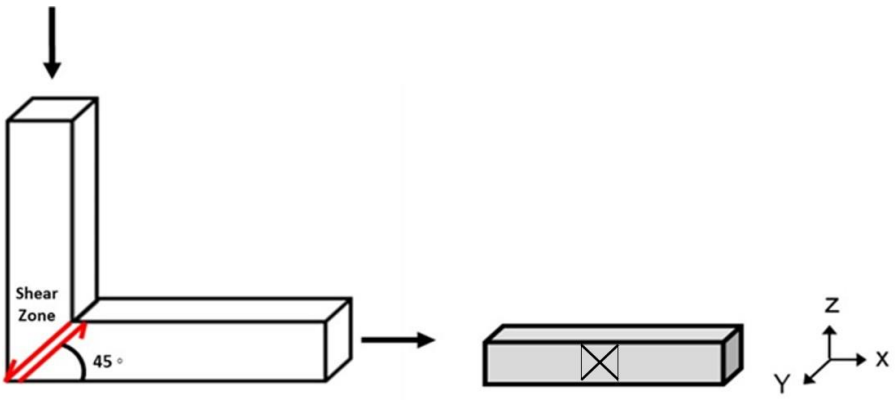

Figure 14: ECAP 90-degree die and x, y, z plane designations. The crossed region indicates the center part of the bar tested in this study.

3.3 Results and Discussion

3.3.1 Material Microstructure

Figure 15a shows a backscatter image of the material surface after processing. The chemical distribution of the AlFeSi IMCs as confirmed by EDX analysis (Fig 15b) is inhomogeneous. Indeed, the AlFeSi IMCs preferentially align along the shear direction (45-degree angle) as reported in previous studies[48]. The etched microstructure of the material reveals a banded structure composed of multiple shear bands along the shear direction as well (Fig. 15c). The shear bands are not visible under the SEM even after etching (Fig. 15d). Thinner bands in the direction perpendicular to the shear direction cross the larger bands. Indeed, after each extrusion there is a formation of shear bands with a 45-degree orientation that rotates by 90 degree after the next pass due to the bar rotation. The dark spots in the etched microstructure correspond to the intermetallic compounds around which pits nucleate during etching (Fig. 15d). It appears in Figure 15c that most of them are located within the bands but not all the shear bands are decorated with these compounds. Also, the matrix is composed of several small precipitates, more evident in the etched

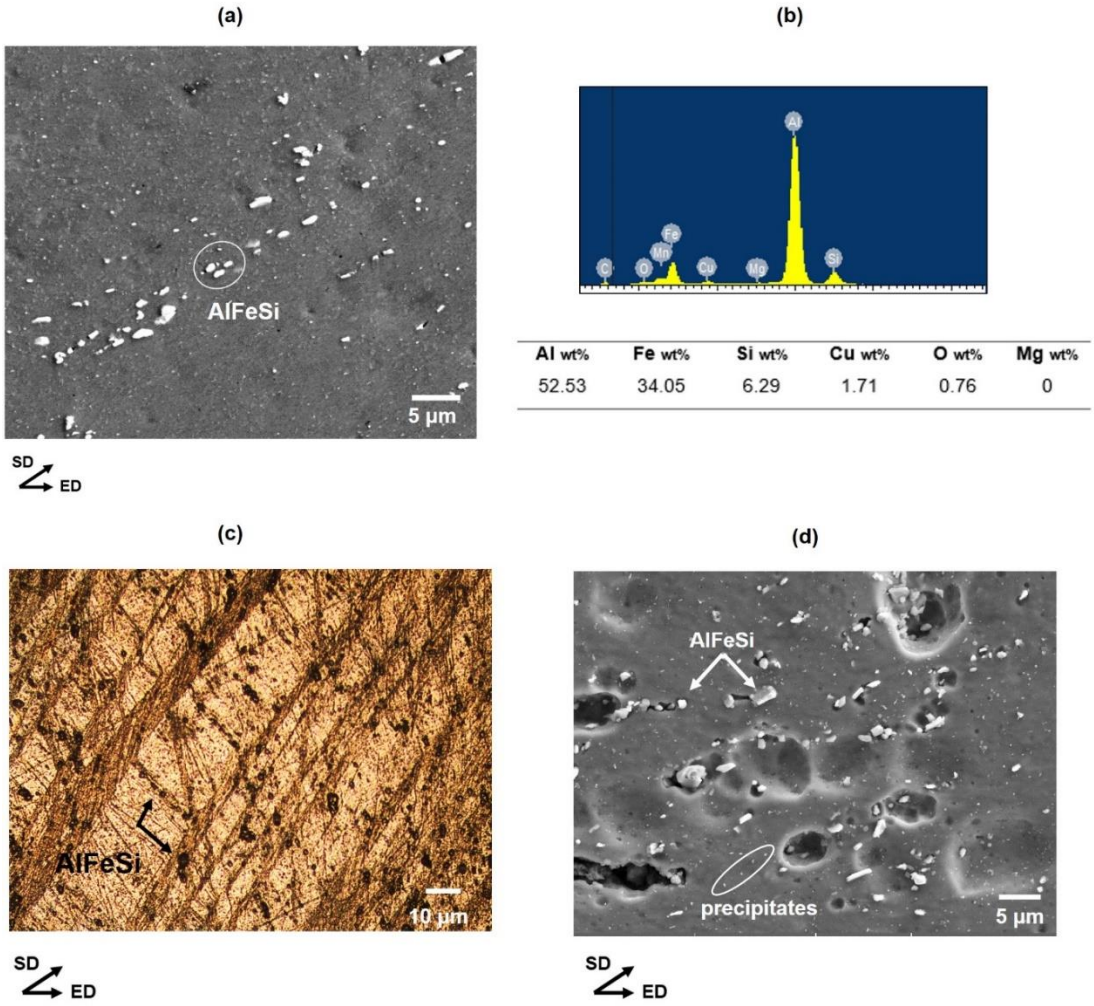

Figure 15: (a) SEM backscatter image of the As-extruded material showing the AlFeSi compounds distribution. (b) EDX analysis results confirming the AlFeSi compounds chemistry. (c) Etched microstructure of the As-extruded material showing shear band structure. (d) Corresponding SEM image.

microstructure (Fig. 15b). These precipitates nucleated during the processing by a dislocation assisted mechanism called dynamic precipitation[46]. The precipitate chemistry previously characterized by high-resolution transmission electron microscopy (HRTEM) was reported as β"(Mg_2Si) precipitates[46]. Here we performed X-ray analysis to have a global picture of the existing phases in the material (Fig. 16). We detected a small peak at a 2Θ value of 39.8° attributed to the Mg_2Si phase. We also identified a peak at 34.1° which we attribute to the AlCuMgSi phase.

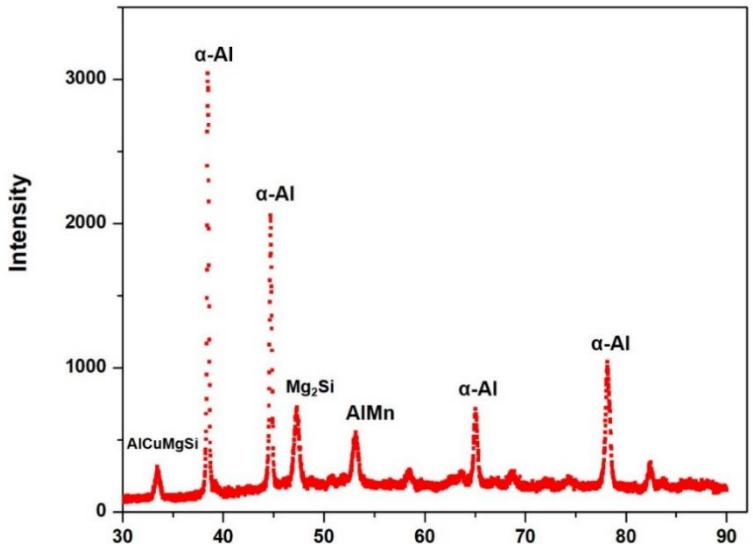

Figure 16: XRD pattern of the As-extruded material after three ECAP passes indicating the existence of AlCuMgSi and Mg_2Si phases in the material.

3.3.2 Vickers Hardness

To investigate precipitation hardening effects on the localized corrosion of the material, we performed a post-aging treatment at 100 ˚C up to four days after processing. This choice of aging temperature and time is based on previous results indicating that precipitation hardening in this material is effective after low-temperature aging for a couple of days[50]. The Vickers hardness evolution as a function of aging time at 100 ˚C is shown in Figure 17. There is a slight increase in hardness after 3 ECAP passes (~110 HV) compared to the as-received AA6061-T6 material (~ 100 HV). Such increase with processing is attributed to grain boundary and dislocation strengthening as demonstrated in the literature[50]. The hardness increase becomes more significant with aging up to 48 hours (~ 152 HV) due to the nucleation and growth of β"(Mg_2Si) and β'(Mg_2Si) precipitates[49]. The material in this state (at the peak hardness) will be referred as extruded and peak aged in this study. Further aging up to four days decreases the hardness down to 136 HV as a consequence of precipitates coarsening and grain growth. This combination of aging

time/temperature differs from the conventional T6 heat treatment for which peak hardness occurs (~175 ˚C for about 8 hours)[9].

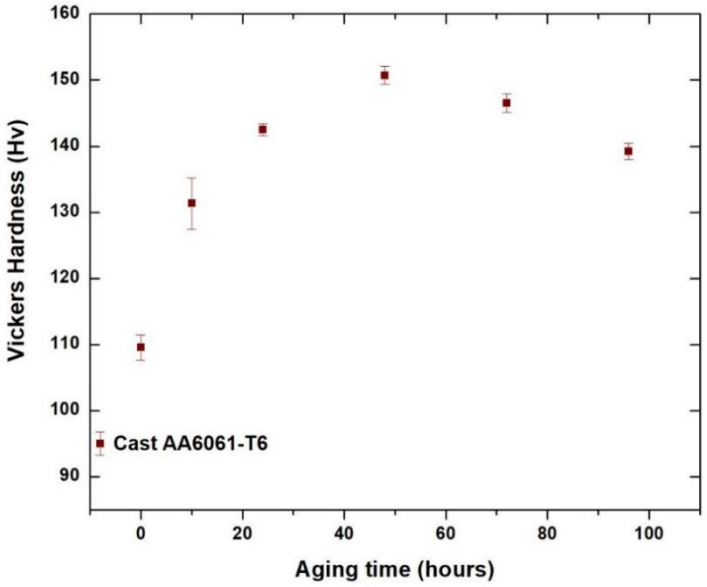

Figure 17: Vickers Hardness evolution after extrusion and post-aging at 100 ˚C up to four days.

3.3.3 Shear Bands Microstructure

3.3.3.1 AlFeSi IMCs Distribution

AlFeSi are the main Fe-rich intermetallic compounds that form in Al-Mg-Si alloys during casting. In the material, they exist as hexagonal α-Al_8Fe_2Si phase and monoclinic/orthorhombic β-Al_5FeSi phase[131]. These phases do not dissolve during homogenization at 530 ˚C even after long homogenization times. Therefore, they remain in the matrix throughout the ECAP process. In terms of corrosion behavior, AlFeSi compounds are cathodic to the aluminum matrix because of their Fe content. Due to that, they are preferential sites for pitting in aluminum alloys[72]. As a consequence, their distribution has to be carefully controlled during processing to avoid segregation that results in large pit formation during corrosion.

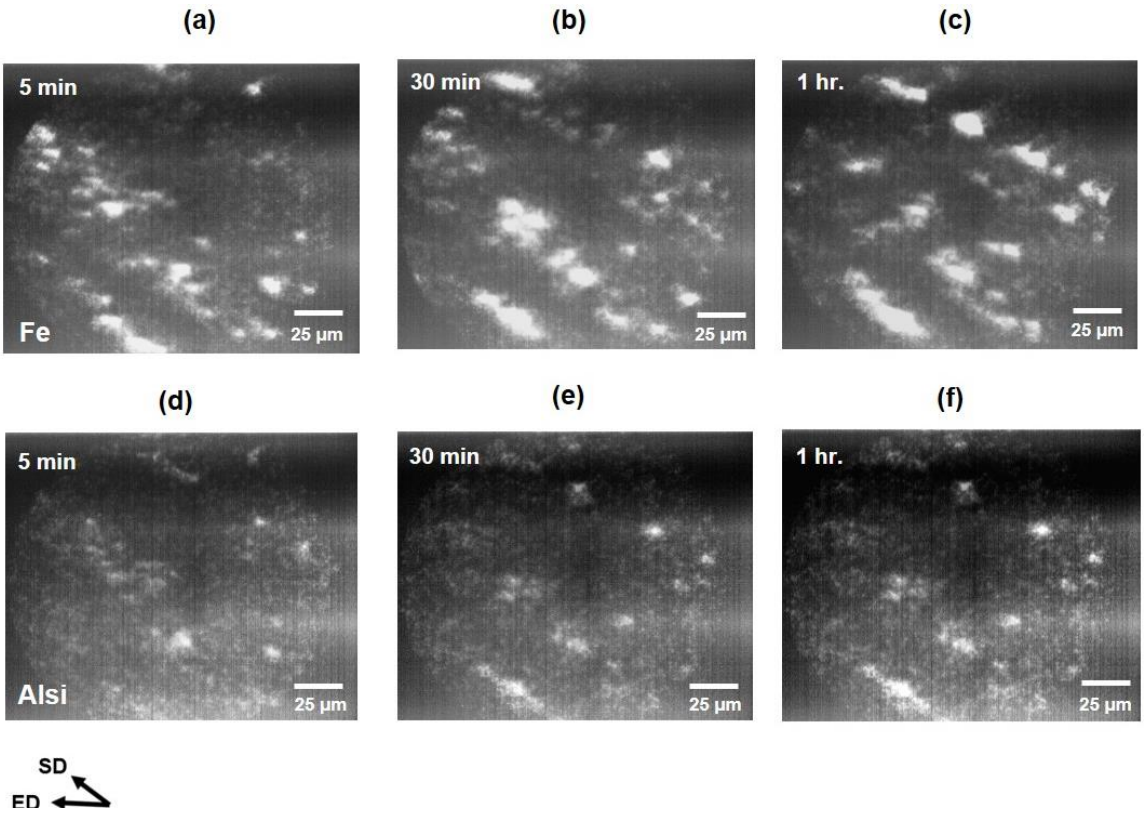

Figure 18: TOF-SIMS depth profile images of Fe (top) and AlSi-compounds (bottom) after processing for different sputtering times. (a, d) 5 minutes sputtering, (b, e) 30 minutes sputtering (c, f) 1 hour sputtering.

In order to picture the IMCs distribution on the surface and in the bulk of the material after extrusion, we performed TOF-SIMS analysis. The analysis was performed on Fe to track the AlFeSi compounds location as Fe is not involved in other phases in the material. Fig. 18a, 18b & 18c display the results after sputtering up to one hour. The circle where the bright areas indicate the location of Fe has a diameter of 150 µm. The same analysis was performed on the AlSi compounds, which location (bright areas) matches with that of Fe (Fig. 18d, 18e, 18f). This complementary analysis confirms that the location of Fe atoms corresponds to the location of the AlFeSi compounds in the material. Figures 18d, 18e & 18f display clear evidence of isolated Fe-rich regions along the shear direction, similar to the AlFeSi distribution observed in Figure 15a. In addition, the orientation and location of the bright bands remain unchanged after further sputtering

up to 1 hour (equal to a sputtered thickness of 50 microns). Also, the overall intensity of the Fe signal does not fade, indicating alignment of AlFeSi compounds under each other. Thus we conclude from the TOF-SIMS analysis that the shear direction and shear plane of this material are the preferred locations for AlFeSi compound aggregates. As a consequence, this direction and plane will be highly susceptible to pitting and large pit formation. It is important to mention that there is no correlation between the size of the bright areas and the real size of the Fe-rich compounds.

3.3.3.2 Hardening Precipitates Distribution

In this study, we took advantage of the high lateral resolution of the atomic force microscope (AFM) and its good topography contrast to study precipitation phenomena in the material. However, this technique does not provide information on precipitate chemistry. Figures 19a, 19b & 19c show the results after processing and peak aging (at 100 ˚C for two days). Figure 19a exhibits a banded structure similar to the etched microstructure (Fig. 15c). Most of the bands are oriented along the shear direction (45-degree angle). They also cross each other similarly to the bands in Figure 15c due to the bar rotation between each pass. Therefore, we suggest that the bands observed in the AFM maps correspond to the shear bands of the material. Additionally, there are clear signs of a difference in precipitation behavior between the matrix and the shear bands full of precipitates. Figure 19b & 19c show a higher magnification of the shear band interior with clear details of the precipitate morphology, size, and distribution. We can identify three types: (1) “point” precipitates of ~20 nm size, (2) “lineal” precipitates with a spherical shape and an average diameter less than 10 nm and (3) “cluster” precipitates of ~ 50 nm size. Similar precipitate sizes and morphologies were previously reported in the literature by transmission electron microscopy

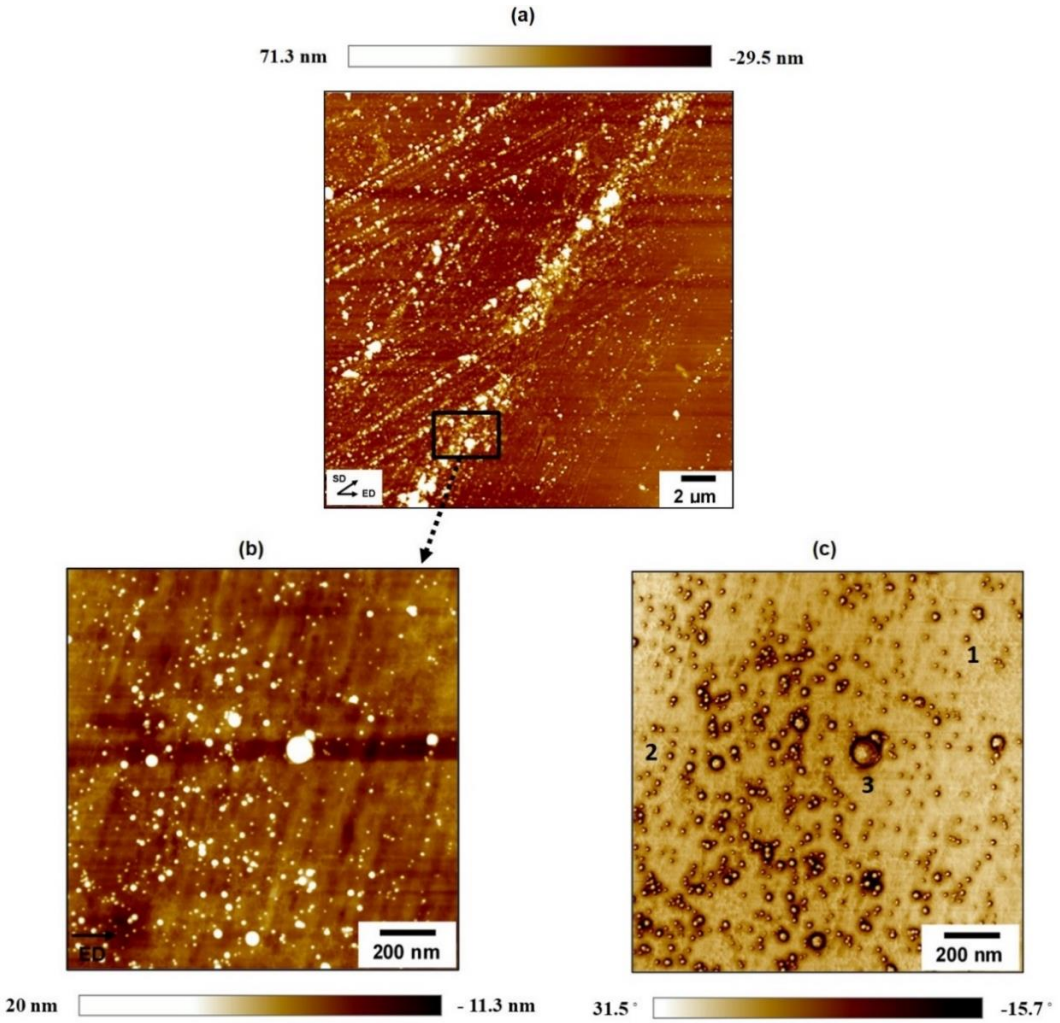

Figure 19: AFM maps of the material after extrusion and peak aging. (a) Topography map showing shear band structure and preferential precipitation inside the shear bands. (b) Topography map of the shear band interior showing precipitate morphology & distribution. (c) Corresponding phase map with (1) indicating "point" precipitates, (2) indicating "lineal" precipitates and (3) indicating "cluster" precipitates.

(TEM) indicating a good correlation between the two analyses[45]. Figure 20 shows the AFM map of the as-extruded material which exhibits different precipitate morphology and distribution. Indeed there is a homogenous distribution of small spherical precipitates, formed by dynamic precipitation with no apparent signs of clustering. This is explained by the low processing temperature (room temperature) and time (less than 5 min per extrusion) that do not provide enough driving force for cluster formation.

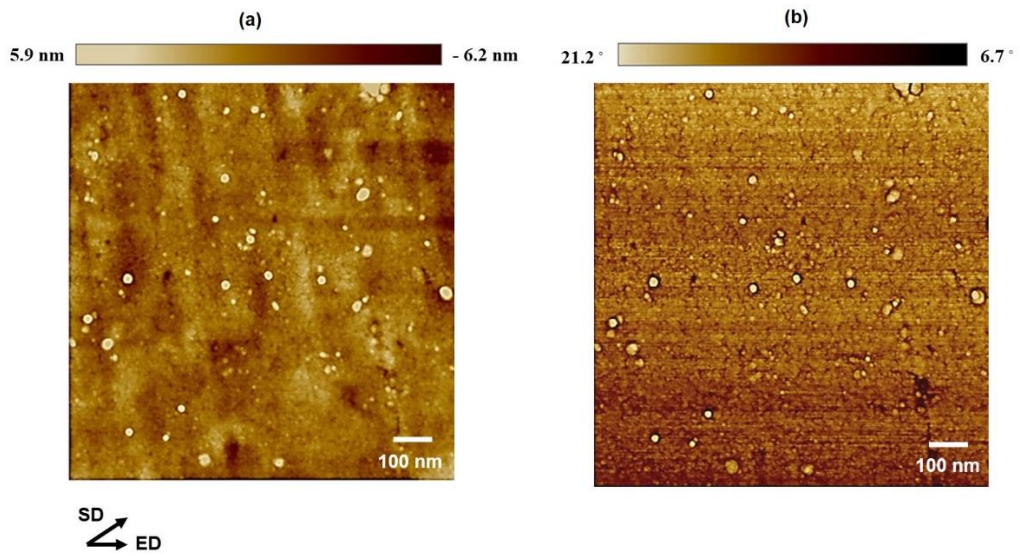

Figure 20: AFM (a) topography map and (b) phase map of the As-extruded material showing small precipitates homogeneously distributed in the matrix.

3.3.3.3 Shear Bands Grains Structure

The difference in precipitation between the shear bands and the matrix suggests a difference in microstructure such as dislocation density, grain size, grain morphology and grain boundary misorientation known to affect precipitation kinetics. To understand such differences, we investigated the shear band grain structure by EBSD, after processing. Figure 21 and Figure 21b show the inverse pole figure and GB orientation maps of the as-extruded material with a heterogeneous grain size distribution. Indeed, the shear bands, delineated by dashed lines, are composed of small equiaxed grains with a higher misorientation (> 15 degrees) than the matrix, which is composed of coarser grains (Fig. 21b). It is known that shear bands in aluminum alloys are composed of equiaxed grains with a majority of high angle boundaries (HAGBs) (misorientation > 15 degrees), surrounded by low angle boundaries (LAGBs) (misorientation < 15 degrees)[38, 130]. It is also known that HAGBs possess high energy making them highly susceptible to grain boundary precipitation. As a consequence, grain boundary precipitation in the shear band

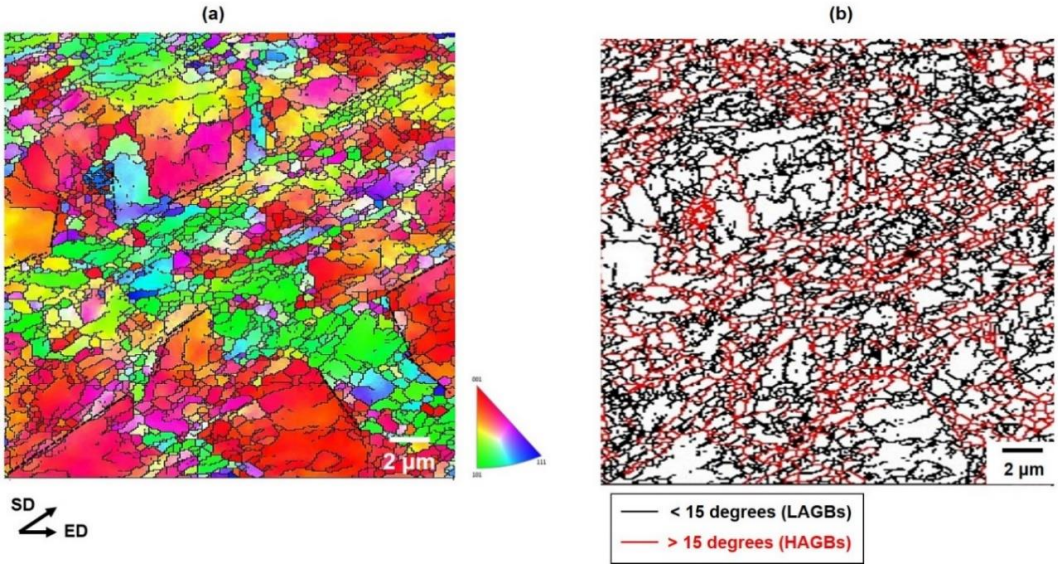

Figure 21: EBSD results after three ECAP passes. (a) Inverse pole figure showing shear band internal structure composed of fine equiaxed grains. (b) Corresponding grain boundary misorientation with thin black lines indicating LAGB and thin red lines for HAGBs.

region will most likely be higher than in the matrix. Although this analysis provides a possible reason for the difference in precipitation, it does not suggest that all precipitates in the shear bands are located at the grain boundaries. Intragranular precipitates may exist in the shear band matrix as well due to nucleation and growth at dislocations[46].

3.3.4 Volta Potential Distribution

In the current work, we acquired the Volta potential difference (VPD) distribution of the material's surface in air using the scanning Kelvin probe force microscopy (SKPFM) technique, simultaneously with its topography and phase maps. The goal was to detect whether or not a significant difference in Volta potential exists between the precipitates/clusters and the matrix. VPD is the indirect measurement of the electron work function (EWF) difference between the scanning probe tip and the material. EWF is by definition the minimum energy required to remove an electron away from the material's surface in a vacuum. It was demonstrated in the literature

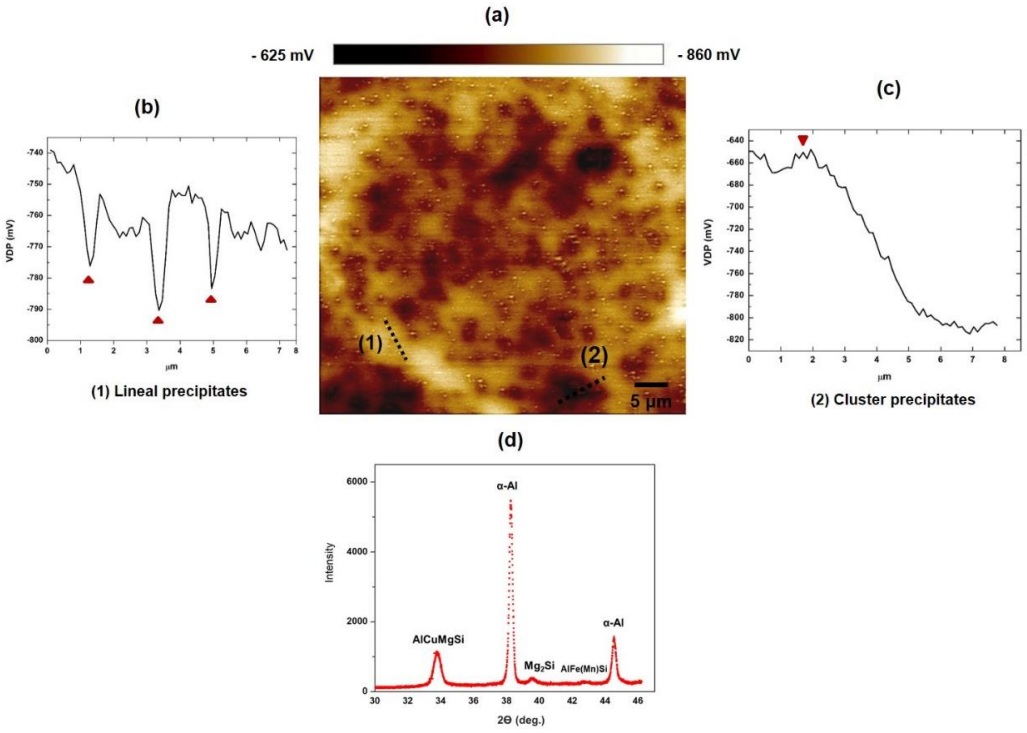

Figure 22: (a) VPD map of the Extruded and peak aged material obtained by SKPFM. (b) VPD difference scan of the lineal precipitates. (c) VPD scan of the cluster precipitates. (d) XRD pattern of the surface indicating Mg_2Si and AlCuMgSi phases.

that a linear relationship exists between VPD in air and the free corrosion potential in an aqueous environment[117]. As a rule, cathodic precipitates will most likely exhibit a positive VPD with the matrix while anodic precipitates will display a negative VPD. However, it was demonstrated that this correlation is not always correct. Also, the measurement is sensitive to surface preparation, residual stress and surface impurities[118, 132] therefore the use of VPD to predict corrosion behavior must be done with caution. Figure 22b displays the VPD results over a 0.25 mm^2 area scan. The distribution is heterogeneous; there is a sharp difference in contrast between the "lineal" precipitates (brighter) and the clusters (darker). Regarding VPD, the "lineal" precipitates exhibit a negative VPD with the matrix (- 40 mV) characteristic of anodic behavior (Fig 22a). In contrast, the clusters display a large positive VPD (+170 mV), which is characteristic of cathodic behavior

(Fig. 22c). In AA6061, anodic precipitates are most likely enriched in Mg in the form of Mg_2Si precipitates while cathodic precipitates are mostly enriched in Cu in the form of a so-called Q phase ($Al_4Mg_8Si_7Cu_2$)[50, 128]. Precipitates of this kind were depicted in the extruded and peak aged material by X-Ray diffraction (Fig. 22d). However, a more local chemical analysis of precipitate chemistry is needed to identify their exact composition.

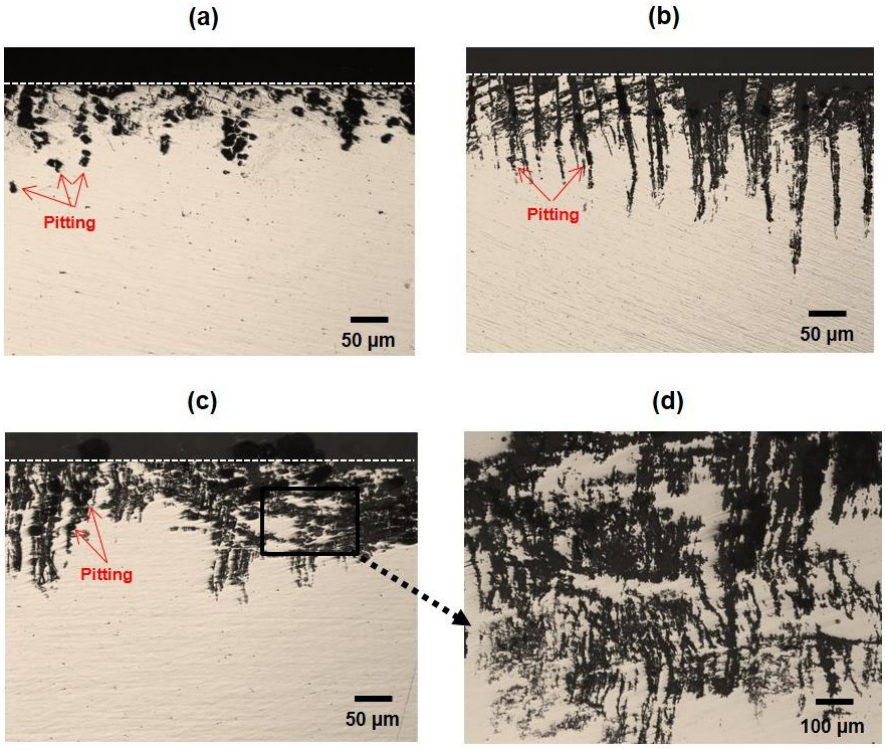

Figure 23: Material's cross-sections after immersion for 24 hours in 30 g NaCl/L and 10 mL HCl/L, pH ~1. (a) As-extruded material. (b) Extruded & peak aged material (two days aging). (c) Extruded & overaged material (three days aging).

3.3.5 Immersion Test Results

The localized corrosion susceptibility of the materials after processing on one hand and processing + aging on the other hand were evaluated in an acidified concentrated NaCl solution (pH ~ 1). Figures 23a, 23b & 23c display the results after a 24 hours immersion. The as-extruded

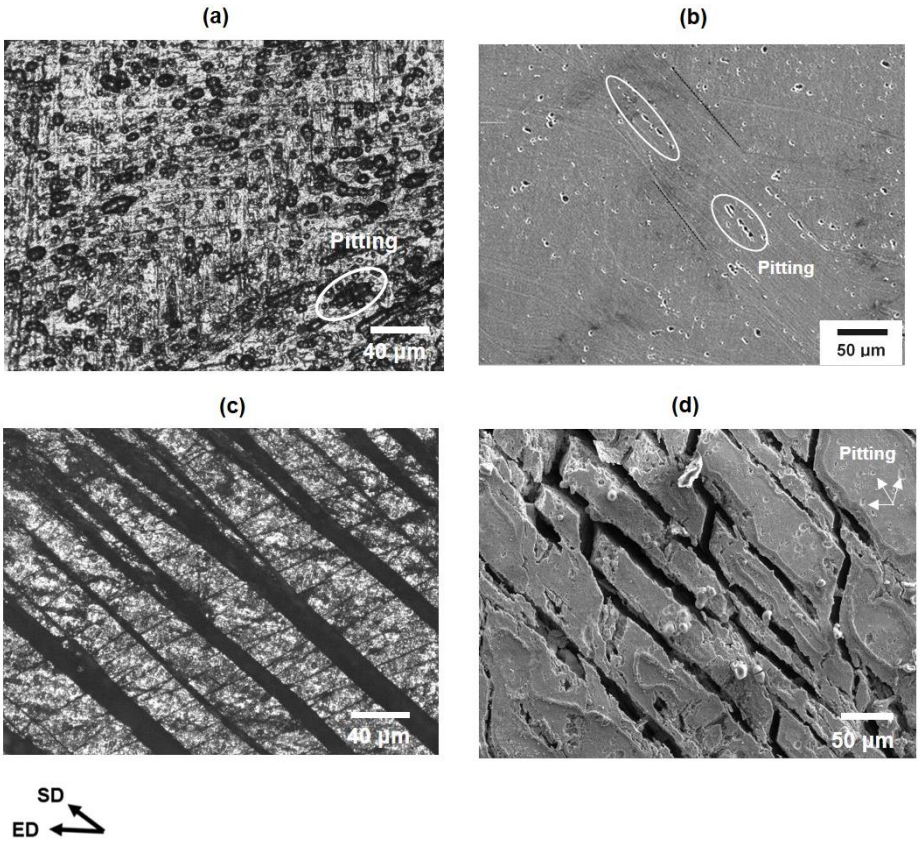

Figure 24: Corrosion morphology of the exposed surface after immersion for 24 hours in 30 g NaCl/L and 10 mL of concentrated HCl/L, pH ~1. (a) OM image of the as-extruded material surface showing pitting attack. (b) Corresponding SEM image. (c) OM image of the Extruded & peak aged material surface showing shear band corrosion. (d) Corresponding SEM image.

material's cross-section exhibits clear signs of pitting with an attack morphology composed of several close spaced pits (Fig. 23a). The corresponding exposed surface (Fig. 24a & 24b) displays evidence of pits on the entire surface as well. The pits appear more elongated and closer along the shear direction as a result of IMC alignment in that preferential direction (Fig. 15a). The material reactivity changes significantly when ECAP is combined with aging (Fig. 23b and Fig. 23c). Indeed the corrosion attack morphology is no longer characterized by pitting but by the substantial dissolution of the matrix around the pits, regardless of the aging time (Fig. 23d). The corresponding exposed surfaces of the peak aged and overaged materials were also investigated (Fig. 24c & 24d). The corrosion is highly localized along the shear direction in the form of bands similar to the shear

band networks revealed by etching (Fig.15c). The SEM image of the peak aged material indicates existence of multiple small pits in the surrounding matrix that did not entirely dissolve. The IGC penetration depth is the highest for this material (~ 200 μm) (Fig. 24b).

3.3.6 Shear Bands Corrosion Initiation Mechanism

To better understand the IGC mechanism after ECAP and aging, as well as the morphology of the corrosion attack, the peak aged material was immersed for 5 hours and then removed from the solution for examination. Fig. 25a indicates that corrosion is localized along the shear direction.

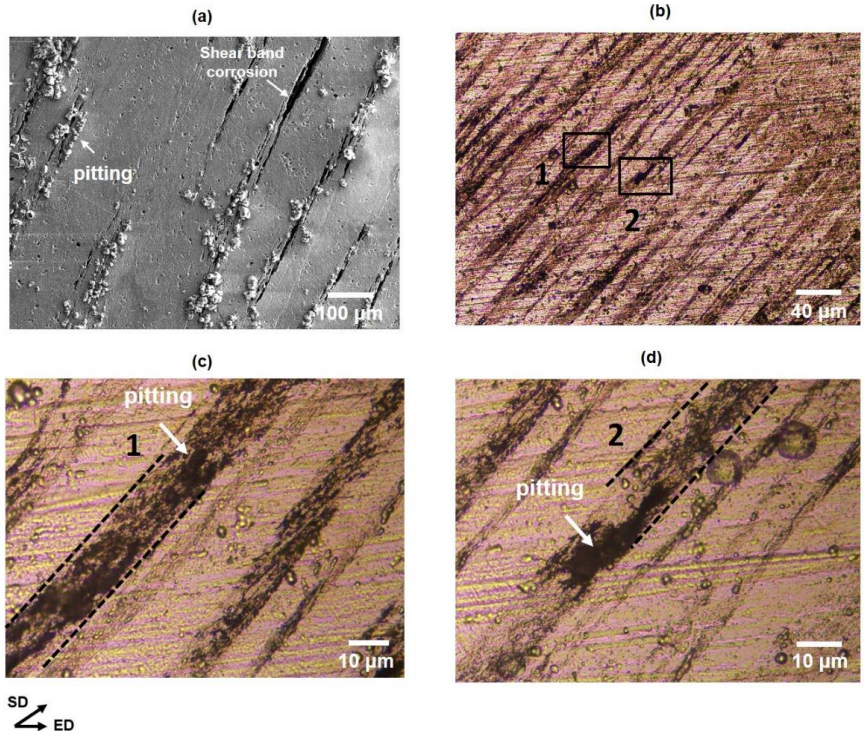

Figure 25: (a) Corrosion morphology of the exposed surface after a five-hour immersion in 30 g of NaCl/L and 10 mL of concentrated HCl/L. (b) (c) & (d) show corrosion restricted to the shear band region & pitting occurring within the shear bands.

Fig. 25b, 25c & 25d also indicate that the dissolution is restricted to the shear band area, explaining the banded attack morphology. In addition, several pits are visible within the bands (Fig. 25c &

25d). They are close to each other and aligned along the shear direction, found to be the most susceptible direction to pitting. The AlFeSi compounds responsible for such enhanced reactivity have been identified within the pits where the particles did not fall out (Fig. 26a and Fig. 26b). The micrographs also show subgrain boundary dissolution in their vicinity (Fig. 26b). The total length of the dissolution, which is about 150 μm indicates how fast the shear band corrosion propagates. Base on the microstructure analyses and immersion test results, we suggest the following mechanism for the shear band dissolution: the dissolution starts first by pitting around the closely spaced AlFeSi compounds located either within the shear bands or at the vicinity of the shear band

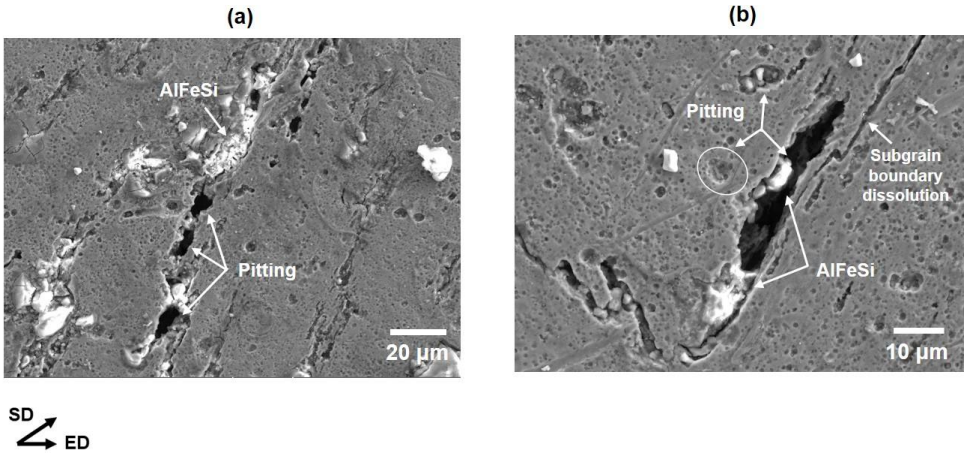

Figure 26: SEM images showing (a) formation of closely spaced pits at the vicinity of the AlFeSi compounds, & (b) extensive grain boundary dissolution of ~ 150 micron long.

boundary. The large density of precipitates and their large VPD provide enough driving force for the corrosion to propagate toward the bands and consume all of the grains. The dissolution eventually slows down when the opposite shear band boundary is reached (as sketched in Fig. 27 – top image). A possible explanation for this could be the difference in precipitation between the shear band and the matrix. Indeed the lower density of precipitates in the matrix provide less

driving force for corrosion compare to the shear band region, full of precipitates. As a consequence, the shear band dissolution will slow down once the matrix is reached.

3.3.7 IGC Propagation Mechanism

The immersion test results indicate the formation of interconnected pits in the cross-section of the as-extruded material (Fig. 26). Such attack morphology is attributed to the cathodic IMC distribution along the entire shear plane of the material. As a consequence, the pits will tend to merge to form larger pits (Fig. 26a). In the case where the IMCs are not close enough to combine, the acidic pit environment will lead to the formation of multiple interconnected pits by a chain

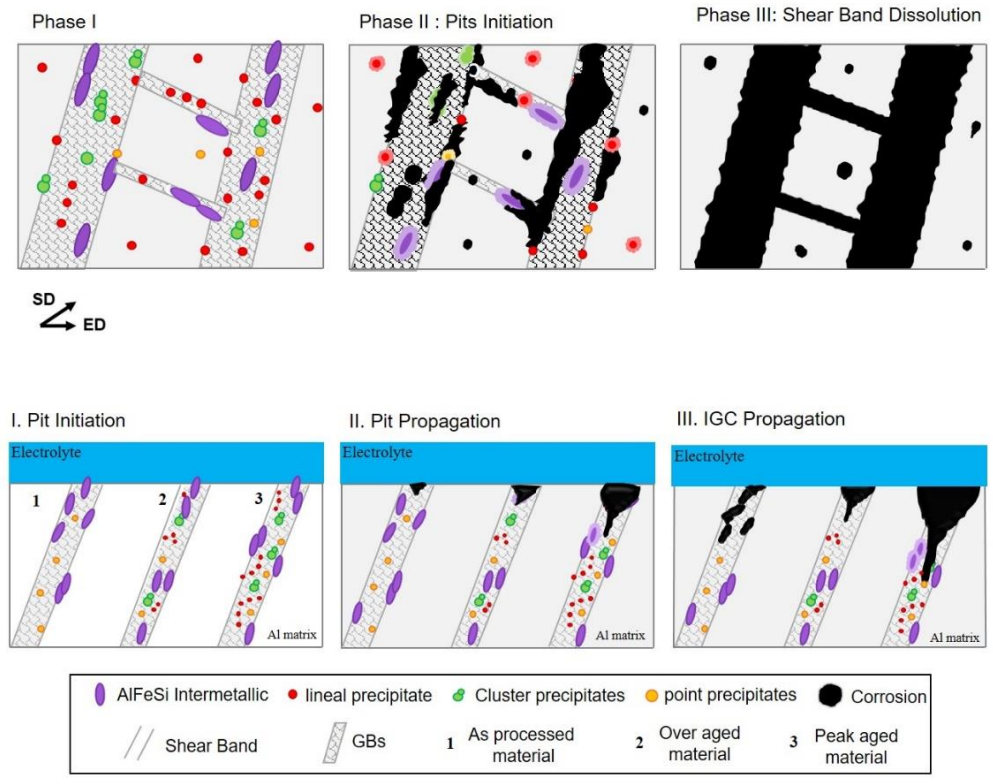

Figure 27: Schematic of the localized corrosion mechanism after processing & aging. Top image: proposed mechanism for shear band corrosion (top view). Bottom image: proposed mechanism for the initiation and propagation of IGC within the material (cross-section view).

reaction (Fig. 27 – bottom image). When ECAP is combined with aging, the AlFeSi compounds are surrounded by several anodic and cathodic precipitates. Therefore, the pitting attack does not only induce the formation of interconnectedpits in the cross-section, but the corrosion of the surrounding matrix also occurs as shown in Fig. 25(c) and sketched in Fig. 27 – bottom image).

3.4 Conclusions

In this study of how strain localization affect the corrosion susceptibility of severely deformed Al-Mg-Si alloys:

- We showed by TOF-SIMS analysis that alignment of cathodic AlFeSi compounds within the shear plane and along the shear direction of the material occurs during processing. Such an IMC distribution makes this direction and this plane highly susceptible to pitting.

- We demonstrated that the combination of ECAP and aging, performed to increase strength, induces preferential segregation of precipitates and clusters within the shear bands when the microstructure is partially recrystallized. As a consequence, the bands are preferred regions for the initiation and propagation of IGC in ultra-fine grained (UFG) aluminum alloys processed by ECAP.

- Base on the previous conclusions, shear band formation must be avoided or minimized to improve the localized corrosion resistance of aluminum alloys in a chloride-rich environment.

- This study points out possible reasons for the conflicted literature about the effects of grain size/processing on corrosion, as the shear band structure, being process and material dependent, have a strong influence on the localized corrosion resistance of the overall material.

4. INSIGHTS INTO THE ELECTROCHEMICAL RESPONSE OF A PARTIALLY RECRYSTALLIZED Al-Mg-Si ALLOY AND ITS RELATIONSHIP TO CORROSION EVENTS*

4.1 Introduction

Ultra-fine grain (UFG) aluminum alloys are of great interest to the transportation industry due to their high strength/weight ratio[29, 133]. They have been successfully processed in the laboratory by severe plastic deformation (SPD) techniques such as equal channel angular pressing (ECAP)[129], high-pressure torsion (HPT)[23], and accumulative roll bonding (ARB). ECAP appears to be the most promising route to process high strength aluminum alloys with reasonable ductility at a large scale[129]. The technique often consists of pressing a material through a 90-degree angle die, at a high strain rate by shear deformation, without changing the workpiece cross-section. The process can increase the strength of AA6XXX by 40% when combined with a low-temperature post-aging due to grain refinement, the formation of a high dislocation density and the promotion of fine precipitates in the aluminum matrix[50]. However, the influence of such microstructure on the electrochemical response of the bulk material, and the sequence of corrosion events are still unclear. Indeed, the corrosion susceptibility of UFG aluminum alloys involves multiple localized mechanisms at once which make the understanding of its electrochemical response complex. Many studies have investigated the influence of SPD processes on the electrochemical response of aluminum alloys [34, 94, 96, 98, 99, 101]. The most recent literature indicates that the bulk electrochemical

* Reprinted with permission from "Insights into the electrochemical response of a partially recrystallized Al-Mg-Si alloy and its relationship to corrosion events" by Ly, Ramatou, Karl T. Hartwig, and Homero Castaneda, 2019, *Electrochimica Acta*, 308, pp.35-44. Copyright 2019 by ELSEVIER

response is not influenced by the bulk composition (intermetallic and precipitates) after ECAP[34, 94, 96, 99]. However, the corrosion attack morphology changes from a low density of deep pits to a high density of pits less deep, due to the fragmentation of Fe-rich compounds[96, 101], preferred sites for pitting in Al-Mg-Si alloys[72]. Also, a study reported that the passive film resistance of ECAPed aluminum alloys, assessed by polarization resistance measurements, increases for the same reasons[101]. However, most of these studies investigated the material's electrochemical response either with no post ECAP aging treatment[94, 98, 101] or after a post-aging time for less than 24 hours at high temperature (170 °C)[34, 96]. Such processing routes were demonstrated earlier by Kim et al. to induce little change in the as-extruded microstructure and mechanical properties [50]. Indeed, the most significant changes occur after a low-temperature post-aging treatment (100 °C) for at least two days [50]. To the best of our knowledge, the electrochemical response of UFG Al-Mg-Si alloys after such a heat treatment has not yet been reported. However, in previous studies, we investigated by immersion testing how this heat treatment affects localized corrosion[134, 135]. We learned that pitting and intergranular corrosion (IGC) are confined in the shear bands of the material due to the extensive precipitation of Mg/Si and Cu-rich precipitates in that region. These bands form during processing when the heat generated by the deformation get trapped in the material[127]. They are mainly composed of fine equiaxed grains with high angle boundaries (misorientation >15 degrees) and higher dislocation density than the matrix[38].

It was found for several aluminum grades that high angle boundaries (HAGBs) are more prone to IGC than low angle boundaries (misorientation < 15 degrees) because of GB precipitation [80, 105, 107, 109, 136]. Also, several groups reported corrosion near GB or within grains with no evidence of GB precipitates but with high dislocation density, suggesting a correlation between grain-stored energy, thermodynamic instability and intragranular corrosion[111-114]. This short literature review

shows how complex the synergistic effects of grain size, precipitates, and dislocations density are on the corrosion susceptibility of UFG aluminum alloys.

Here we investigate how shear band formation and precipitation affect the electrochemical response of UFG AA6061 alloys when the microstructure is partially recrystallized (ie made of a bimodale grain size distribution at the initial stage of the deformation). To achieve this, the material was extruded up to 3 passes to maximize shear bands formation [38] then aged at 100 ˚C up to three days. Our results indicate that the electrochemical response of the bulk material is significantly affected by the low-temperature post-aging treatment and the precipitation within the shear bands. Filiform corrosion along the shear direction and pitting occur simultaneously. However pitting does not always lead to filiform corrosion.

4.2 Experimental Procedure

4.2.1 Materials and Processing

Commercial wrought AA6061 aluminum alloy bars (maximal nominal composition: Si 0.6wt%, Mg 0.9wt% Cu, 0.35wt%, Fe 0.7wt%, Mn 0.08wt%) of 178 mm length by 25.4 mm x 25.4 mm area were initially annealed at 530 ˚C for 3h in air, and water quenched. The bars were repetitively extruded at room temperature within 1 hour with a pressing speed of 5 mm/sec. A sliding wall ECAP die with a 90-degree internal angle was used to achieve a maximum of three passes following route Bc (90˚ rotation between each pass). The bars were aged at 100 ˚C for up to three days, 24 hours after extrusion. One was kept in the as-extruded condition for comparison. In this study, the under-aged, peak-aged and over-aged conditions refer respectively to a one day, two days and three days aging treatment based on Vickers hardness measurements reported in the literature[50, 135].

4.2.2 Electrochemical Testing

Electrochemical testing was carried in a 1M aerated NaCl solution and 0.1M deaerated NaCl solution. The deaerated solution was purged with nitrogen gas for 1hr before testing. A standard three-electrode cell composed of a platinum wire mesh counter electrode and a saturated calomel electrode (SCE) as reference were used during all experiments. The electrochemical tests were performed on a 1 cm^2 surface cut from the central part of the extruded bar (to avoid cracks formation)[135] and mounted in epoxy resin. Before corrosion testing, the sample surfaces were mechanically polished with SiC paper up to grade 2000, then rinsed with distilled water and degreased. Cyclic potentiodynamic polarization (CPP) tests were carried out at a scan rate of 0.166 mV/s in both testing solutions after measuring open circuit potential (OCP) for 30 minutes. A current limit of 10 mA/cm^2 was set for the forward scan. Potentiostatic polarization tests were performed at a potential of -650 mV vs. SCE for 45 minutes to assess IGC susceptibility. This potential was selected based on the CPP curves. All electrochemical data were collected with a Gamry Ref 1000 potentiostat at ambient temperature (23 ˚C).

4.2.3 Microstructure Characterizations

Electron backscattered diffraction (EBSD) was carried out to characterized the shear bands internal structure (grain size distribution and GB misorientation). For that we used a TESCAN FERA 3 MODEL scanning electron microscope (SEM) equipped with an Oxford instrument EBSD detector and Aztech V3.3 software. The grain size distribution was acquired with a step size of 100 nm, an accelerating voltage of 15 KV and HKL channel 5 software. We used a threshold of 5˚ for the grain boundary misorientation map. Once the electrochemical test finished, we cleaned the working electrode in an ultrasonic bath and analyzed the pits morphology, the depth of the

IGC, and the width of the filiform corrosion by optical microscopy, scanning electron microscopy (SEM) and a Keyence 3D laser confocal microscope equipped with a VK analyzer V 3.4.0.1 software. Precipitate chemistry was characterized by a TESCAN LYRA 3 MODEL SEM equipped with an Oxford INCA electron dispersive X-Ray spectroscopy (EDX) analyzer.

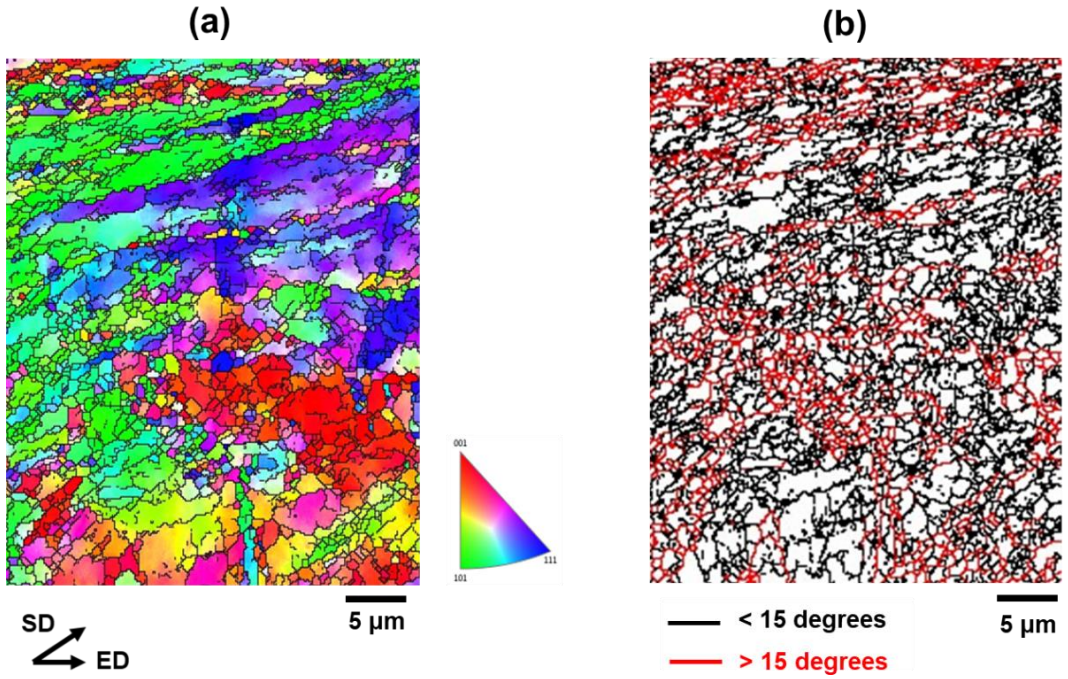

Figure 28: EBSD images after three ECAP passes. (a) Inverse pole figure showing elongated subgrain along the shear direction (SD). (b) Corresponding grain misorientation map with thin black lines indicating LAGBs and thin red lines for HAGBs.

4.3 Results and Discussion

4.3.1 Microstructure

The microstructure after three ECAP passes is partially recrystallized. Indeed it consists of a mix of coarse grains, fine equiaxed grains and elongated subgrains along the shear direction (45-degree angle) (Fig. 28a). The coarse grains and, the elongated subgrains are mainly made up of LAGBs as indicated in Figure 28b. However, some of the elongated subgrains boundaries are

decorated with fine equiaxed grains made up of HAGBs[135]. They formed during deformation by dynamic recrystallization. We showed in our previous study that most of these equiaxed grains are located within the shear bands of the material where precipitation kinetics differ from the matrix[135].

4.3.2 Electrochemical Tests Results

4.3.2.1 OCP evolution

Figure 29 shows the OCP evolution of wrought AA6061-T6 and the ECAPed materials before CPP measurements. First, the as-extruded material exhibits a more positive OCP (~ - 735 mV vs. SCE) than the wrought AA6061-T6 (~ - 750 mV vs. SCE) when no post-heat treatment is performed after ECAP. There is a slight decrease in OCP between the as-extruded material on the one hand and the extruded and aged materials on the other (Table 3). This trend is due to the enrichment of the surface with anodic particles during aging. Indeed it was demonstrated in the

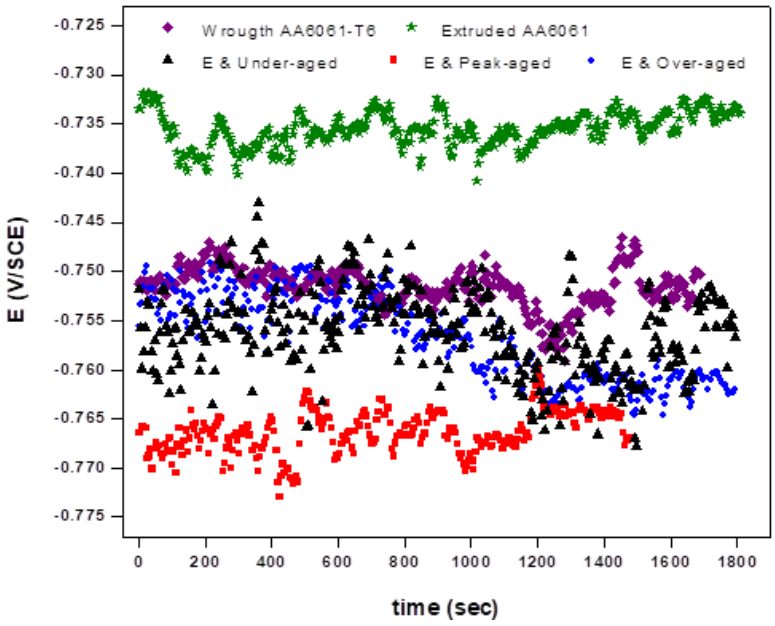

Figure 29: Open circuit potential evolution in 1M NaCl solution: As-extruded AA6061 (star), Wrought AA6061-T6 (diamond), Extruded & under-aged (triangle), Extruded & peak-aged (square), and Rxtruded & over- aged (circle) materials in an aerated 1M NaCl solution.

Table 3: Electrochemical potentials vs SCE derived from the OCP and CPP curves (OCP = Open circuit potential, E_{corr} = corrosion potential, E_{ptp} = pitting transition potential, E_{rep} = repassivation potential).

	OCP (mV)	E_{corr} (mV)	E_{ptp} (mV)	E_{rep} (mV)
Wrought AA6061 T6	-750	-719	-757	-905
Extruded AA6061 (E)	-735	-720	-757	-915
E & Under-aged	-755	-718	-755	-928
E & Peak-aged	-770	-744	-777	-952
E & Over-aged	-760	-740	-767	-941

literature that mainly β'(Mg_2Si) precipitates in the matrix during such a low-temperature heat treatment[50]. Beside, Mg_2Si precipitates are less noble than the aluminum matrix[72]; we confirmed the anodic electrochemical susceptibility of the precipitates by Volta potential difference measurement in our previous study[135]. Also, precipitate density and size increase simultaneously with aging time up to peak aging explaining the lowest OCP value for this material (40 mV less negative than the as-extruded AA6061 material)[50]. The OCP increases after over aging treatment due to precipitate coarsening.

4.3.2.2. Potentiodynamic response

We investigated the effects of ECAP processing on the potentiodynamic response of the materials in the absence of heat treatment. For that we ran CPP tests in a naturally aerated 1M NaCl solution on the as-extruded AA6061 and the wrought AA6061-T6 materials. Figure 30 shows that the shape of the hysteresis loops is similar for both materials. There is a sharp increase in current above E_{corr}, because of anodic dissolution. No passivation behavior and breakdown potential are depicted in the polarization curves as the materials are already in an active state at

OCP (Fig. 30). The potentiodynamic response of the as-extruded and the wrought AA6061-T6 materials are similar; their CPP curves almost overlap (Fig. 30 & Table 3). However, their respective localized attack morphologies are significantly different.

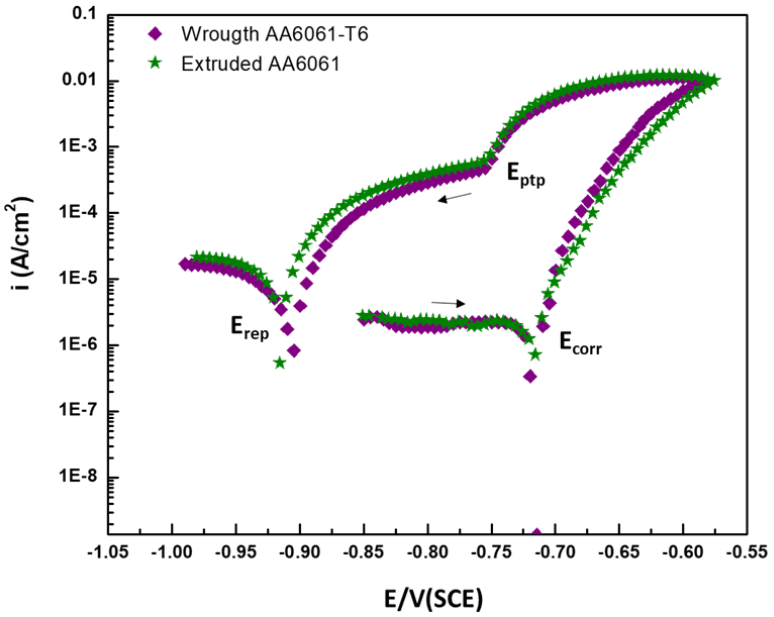

Figure 30: CPP curves of the (a) As-extruded AA6061 (star) and wrought AA6061-T6 (diamond) materials in an aerated 1M NaCl solution. (E_{rep} = repassivation potential, E_{corr} = corrosion potential, E_{rep} = pitting transition potential).

Indeed, pits after ECAP are smaller than in the wrought AA6061-T6 material (Fig. 31b & 31d); they are also closely spaced and elongated along the shear direction. We showed in our previous study that such pits morphology and distribution result from the fragmentation of AlFeSi intermetallic compounds along the shear direction during processing (preferred site for pitting in this material) [127, 134, 135]. In addition the pits are surrounded by filiform corrosion along the shear direction. Similar pitting attack morphology was reported in the literature[97, 99]. The filiform corrosion was explained by the high density of dislocation, high stored energy, and high residual

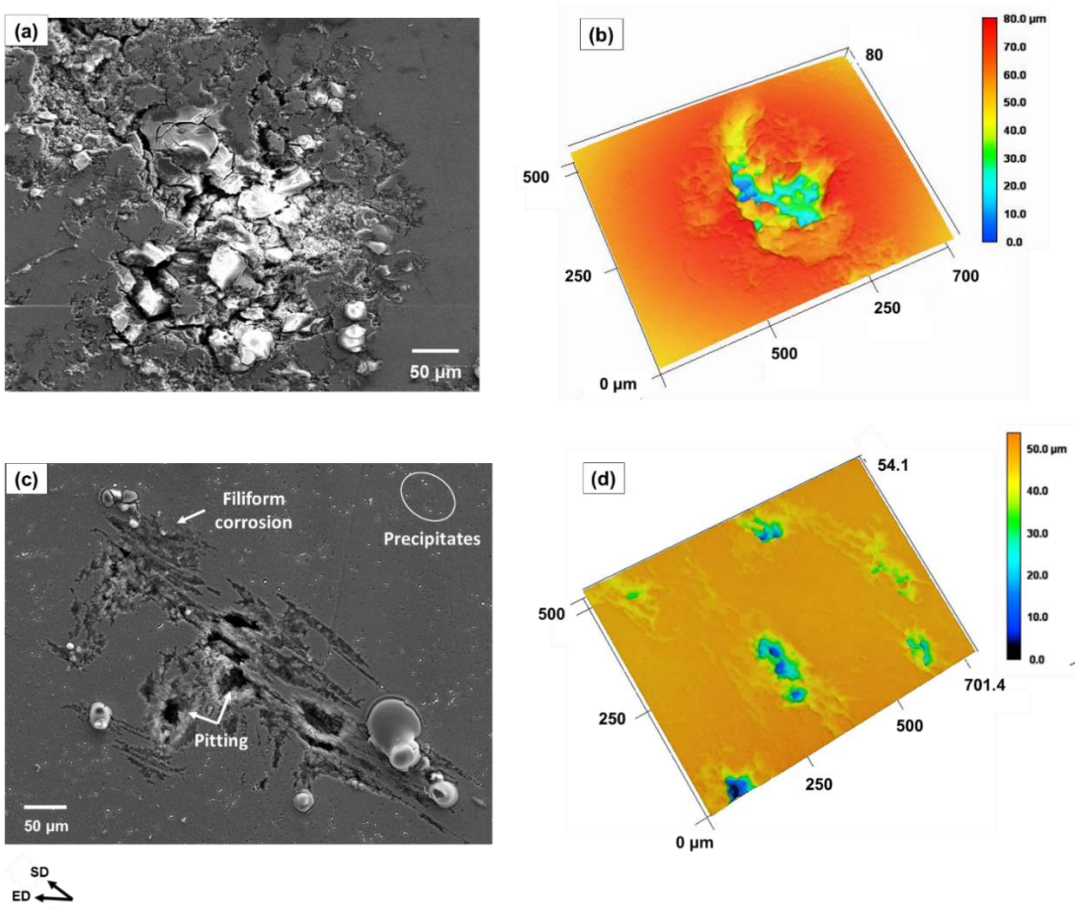

Figure 31: SEM image of pits morphology after CPP testing (left), and 3D representation of the pits (right). Wrought AA6061-T6 (a) & (b), and As-extruded AA6061 (c) & (d).

stress in this material that promote the dissolution of the entire grains during corrosion[97, 99]. Thus, the anodic current density of the as-extruded material accounts for the dissolution of the aluminum the matrix at the AlFeSi intermetallic compounds followed by trenching (pitting corrosion) and the dissolution of the matrix along the shear direction (filiform corrosion). Figure 31c shows several small particles covered by corrosion products in the matrix away from the large pits. These particles were reported as β”(Mg_2Si) precipitates by transmission electron microscopy in the literature[46]. They formed during deformation by a dislocation assisted mechanism called dynamic precipitation. Regarding microstructure, the wrought and the as-extruded materials possess

different volume fraction and size of AlFeSi intermetallic compounds and Mg_2Si precipitates but their potentiodynamic responses are similar. Therefore the bulk potentiodynamic response of UFG AA6061 is not influenced by the bulk composition in 1M aerated NaCl, although the morphology of the corrosion attack changes with ECAP processing. Fig. 31b and 31d show the 3D representation of the pits after cleaning in an ultrasonic bath confirming the increase in pits density after ECAP. Several studies also reported a decrease in pits depth following ECAP as well base on a statistic analysis of multiple pits[34, 96, 101].

4.3.2.3 Effects of a low-temperature post-aging treatment

Figure 32a displays the CPP curves of the as-extruded sample and the post-heat treated materials in the aerated 1M NaCl solution. The corrosion potential (E_{corr}) is unaffected by the post-aging treatment up to 1 day and shift cathodically by ~ 50mV to less noble potentials when the aging time increases (Fig 32a & Table 3). This is attributed to the enrichment of the surface with anodic β'(Mg_2Si) precipitates during aging[50]. Also, pitting corrosion occurs spontaneously at the free potential as the repassivation potential (E_{rep}) is lower than E_{corr} (Figure 32a and Table 3). The width of the hysteresis loops seems identical for all the materials indicating similar degree of pitting regardless of the aging treatment and ECAP processing. In contrast, the slope of the anodic current density above E_{corr} changes significantly with the heat treatment, being the highest at peak-aging and over-aging. Thus, the potentiodynamic response of the bulk material in aerated 1M NaCl, is strongly influenced by the bulk composition (precipitates size & distribution) after a low temperature post-aging treatment. Fig 32b and 32c show the corrosion attack morphology in the peak-aged sample at the end of the CPP test. It is characterized by multiple closely spaced pits surrounded by filiform corrosion along the shear direction. The filiform corrosion appears wider

than on the as-extruded material (Fig. 32b & 32c). It is also supported by the 3D representation of the pits in figure 32d. The EBSD results reveal that most of the small equiaxed grains along the shear direction, are made of HAGBs (Fig 28a & 28b). Such GB characteristics were reported to to promote IGC, due to their high susceptibility to GB precipitation[80, 105, 107, 109, 136]. Besides HAGBs,

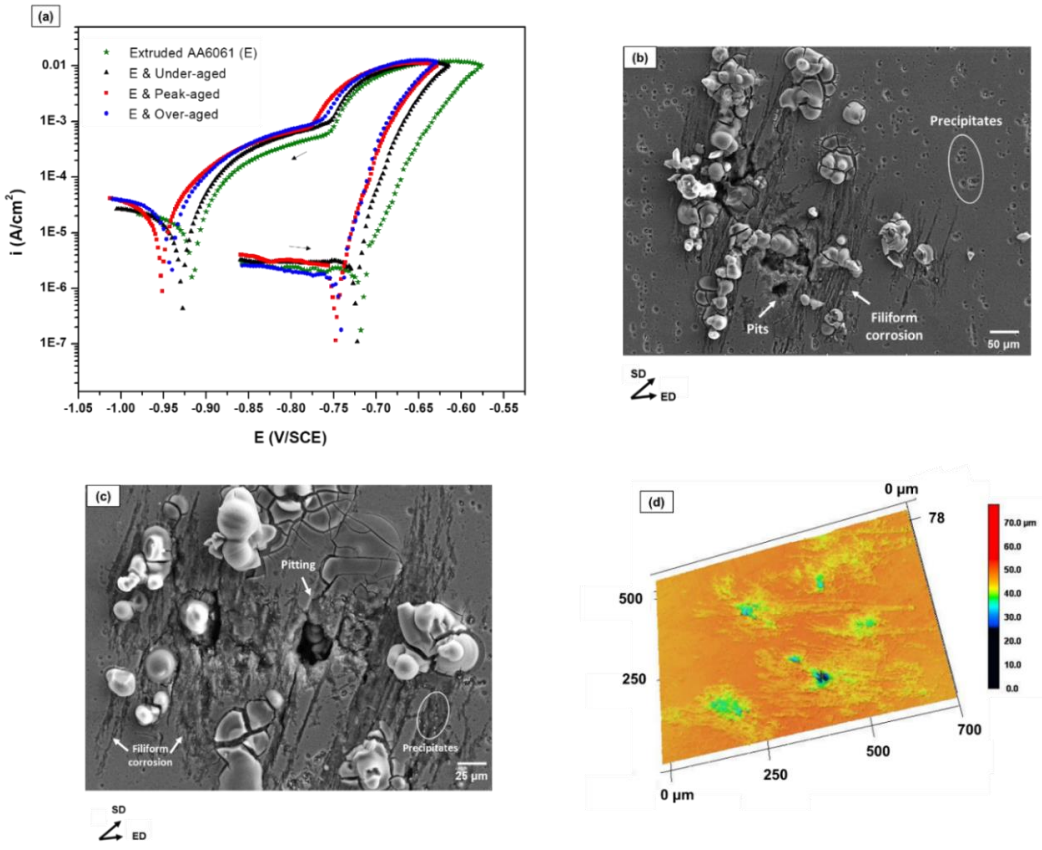

Figure 32: (a) CPP curves in an aerated 1M NaCl solution: As-extruded AA6061 (star), Extruded & under-aged (triangle), Extruded & peak-aged (square), and Extruded & over-aged (circle). (b) and (c) SEM images of the peak-aged material after CPP testing showing pitting and filiform corrosion along the shear direction. (d) Corresponding 3D representation of the pits after CPP test.

dislocations are preferred sites for precipitation in this material as their density increases significantly up to 4 ECAP passes[129]. Therefore, precipitation kinetics and corrosion susceptibility are enhanced along the shear direction[135]. This is confirmed by the numerous precipitates within

the region with filiform corrosion along that direction (Figure 31c). Figure 31b displays multiple small pits with precipitates in the matrix away from the region with filiform corrosion and the shear direction. We showed in a previous study by Volta potential difference (VPD) measurements that these precipitates (identified in the literature as β" (Mg_2Si)[50]) exhibit a negative VPD with the aluminum matrix. Therefore pitting at these anodic β" (Mg_2Si) precipitates involves dealloying of Mg, and Si enrichment of the precipitates. Thus the anodic current density after aging accounts for pitting at the cathodic AlFeSi intermetallic compounds, pitting at the anodic precipitates and filiform corrosion along the shear direction.

The reverse scans of the materials in Figure 32 show an abrupt change in potential known as pitting transition potential (E_{ptp}). This potential shifts to less noble values when post-aging heat treatment is performed, being the least noble at peak-aging (Figure 32a and Table 3). Such trend is in agreement with the evolution of E_{corr} and anodic current density as the extruded and peak-aged AA6061 samples exhibit the most active and the fastest kinetic of dissolution. It is reported in the literature that more negative E_{ptp} could indicate deeper pits[99]. Figures 33a & 33b display the pit morphology under optical microscope after ECAP and peak aging respectively. The filiform corrosion in Figure 33b forms a pattern of parallels lines along the shear direction similar to the shear bands network of the material, revealed by etching in our previous study[135]. This observation confirms that filiform corrosion in UFG AA6061 alloys is preferentially located within the shear bands of the material[97, 135] under potentiodynamic polarization as well. Indeed, these bands, in addition to their HAGBs characters, are regions of high residual strain[97] and high stored energy[137]. All of which were reported to promote pit growth[97, 138] and intragranular corrosion[110-114].

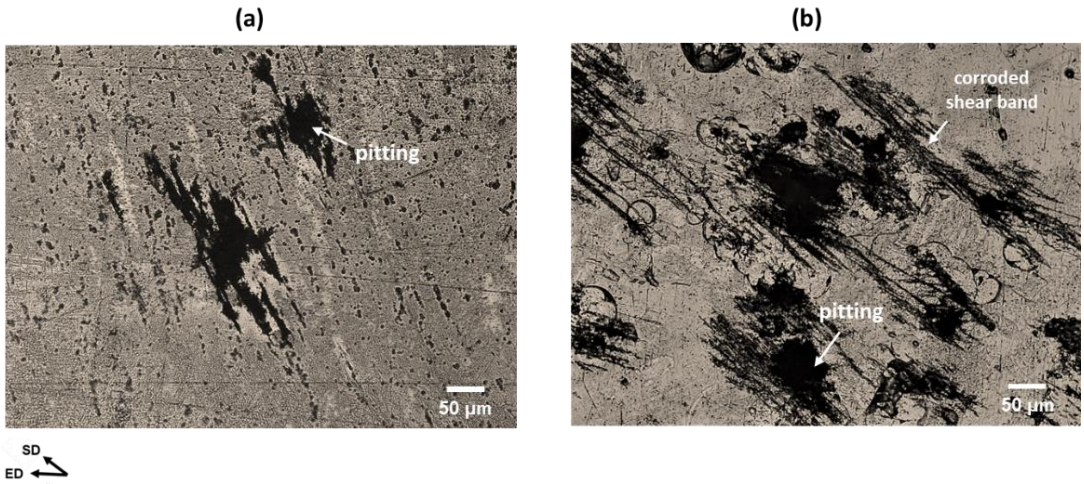

Figure 33: Optical microscope images of pit morphology in the (a) As-extruded material and (b) Extruded & peak-aged material showing pitting and filiform corrosion in the shear bands along the shear direction.

4.3.3 Potentiostatic Response and Intergranular Corrosion

We previously showed that UFG AA6061 are susceptible to IGC after a low temperature post-aging treatment at 100 ˚C up to 3 days[135]. Also the severity and morphology of the IGC attack changes significantly with the precipitation within the shear bands[135]. Here we investigate the relationship between the potentiostatic response of the materials and their susceptibility to IGC in an aerated 1M NaCl. For that we held the as-extruded and extruded and aged samples at -0.65 V vs. SCE for 2500 seconds. Fig. 34 shows a sharp increase in current during the first 1000 seconds for all the samples, characteristic of pit activity. The as-extruded material exhibits the lowest current increase and level, whereas the current density is the highest after peak-aging. Besides, the evolution of anodic current density with aging time follows the same trend as the Vickers hardness up to 1500 sec[50, 135] indicating that the anodic dissolution is influenced by the precipitates size and density after post-aging. However the anodic current density of the over aged material approaches that of the peak-aged material between 1500 and 2500 seconds. Figures 35a, 35b, and 35c display the exposed surfaces of the as-extruded, the peak-aged and over-aged materials respectively at the

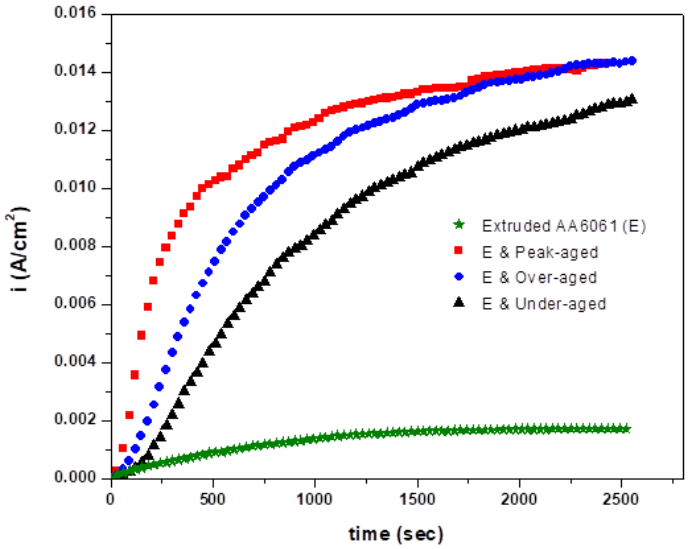

Figure 34: Potentiostatic polarization curves of the Extruded & aged materials in an aerated 1M NaCl solution at – 650mV vs SCE.

end of the potentiostatic test. The as-extruded material shows few small pits with slight corrosion along the shear direction, explaining the lowest anodic current density increase and level (Fig. 35a). In contrast, the peak-aged and over-aged materials surfaces show multiple closely spaced pits surrounded by filiform corrosion along the shear direction (Fig. 35b and 35c). The length and width of the filiform corrosion between the peak-aged and over-aged materials are in agreement with their corresponding anodic current density levels being the highest at peak aging (Fig. 34). However, the pits density seems the same in both materials. Indeed they possess similar volume fraction of fragmented AlFeSi intermetallic compounds. Figure 36 shows the corresponding SEM image of the over-aged material's surface, with a zoom in the region with filiform corrosion. The pits size is relatively small compared to the size of the filiform corrosion (Fig. 36b) confirming that the anodic dissolution at this potential is mainly controlled by the precipitation within the shear bands and the filiform corrosion rather than the propagation of the pits. Metallographic cross-section analyses were carried out after potentiostatic test to investigate IGC. The as-extruded

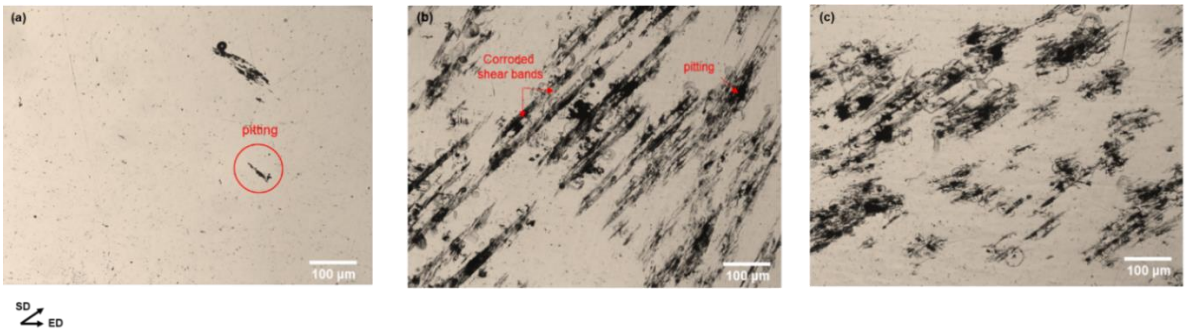

Figure 35: Optical microscope images of the materials exposed surfaces after potentiostatic testing at -650 mV in an aerated 1M NaCl solution. (a) As-extruded material showing pitting attack, (b) Extruded & peak-aged, and (c) Extruded & over-aged materials, showing pitting and corrosion in the shear bands.

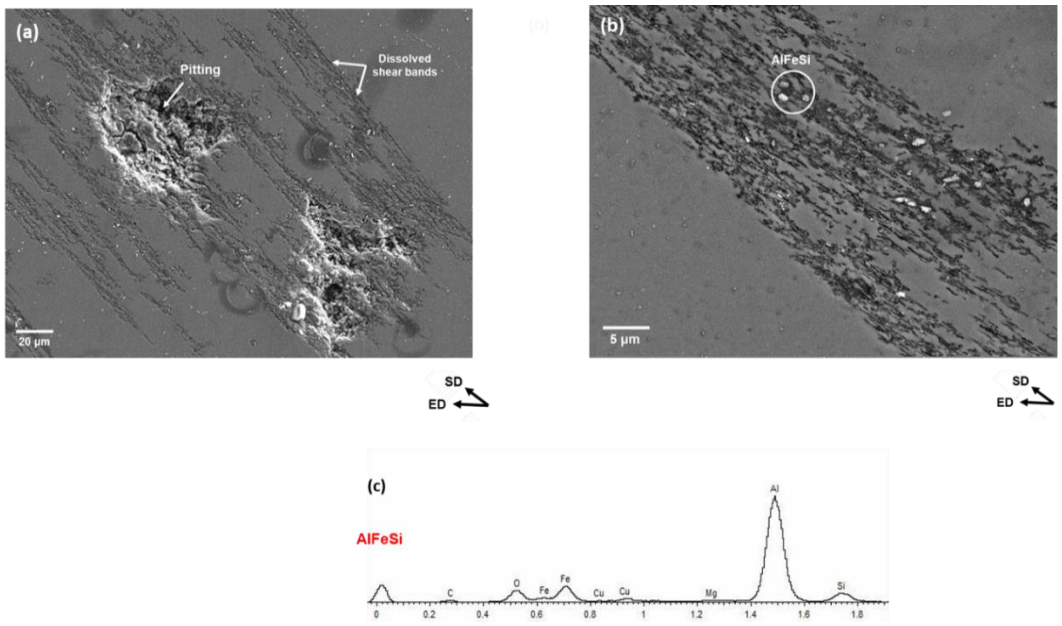

Figure 36: (a) Exposed surfaces of the Extruded & peak aged materials after potentiostatic testing in an aerated 1M NaCl solution at -650Mv vs SCE, (b) Zoom in the dissolved shear bands region showing AlFeSi intermetallic compounds and small precipitates within the subgrain, (c) EDX point analysis spectrum confirming the AlFeSi chemistry of the coarse particles.

material's cross-section does not exhibit visible signs of IGC, but a pit like attack along the shear direction instead (Fig. 37a). A similar observation was reported for an Al-Cu-Mg alloy (AA2024) after potentiostatic holding in a 0.5M aerated NaCl solution[94]. We explained the 45-degree

orientation of the IGC attack by the orientation of the shear planes of the material and the distribution of the AlFesi compounds under each other along that direction[135]. In contrast the peak-aged material exhibits signs of pitting and IGC. Therefore the anodic current density at this potential accounts for pitting at the AlFeSi intermetallic compounds, filiform corrosion in the shear bands and IGC.

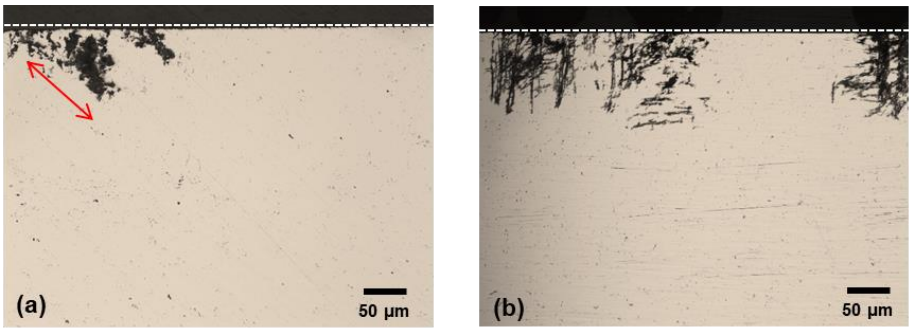

Figure 37: Material's cross sections after potentiostatic testing in aerated 1M NaCl at -650 mV vs SCE (a) As extruded material showing pitting attack, and (b) Extruded & peak aged materials showing pitting and intergranular corrosion. Red arrows indicate the direction of the shear planes.

4.3.4 Passivation Behavior

The potentiodynamic response of the wrought AA6061-T6 material on the one hand and the as-extruded and the peak-aged materials on the other were compared in a 0.1M deaerated NaCl solution. The goal of using a less aggressive environment was to learn about the effects of ECAP and a low-temperature post-aging treatment on passivation, and get more insights into the sequence of corrosion events. These three materials were specifically chosen for study because they exhibit distinct differences in microstructure (AlFeSi compound size/distribution, precipitate/cluster density) as demonstrated in our previous study[135], and distinct electrochemical responses in the 1M aerated NaCl solution. Figure 38 shows a slight decrease in E_{corr} with ECAP (~ 50 mV) regardless of the low-temperature post-aging treatment, indicating that there is no effect of

precipitation in the corrosion potential of the material when measured in 0.1M dearated NaCl solution. Such a trend in E_{corr} was not observed in the 1M aerated NaCl solution (Fig 30 & 32a).

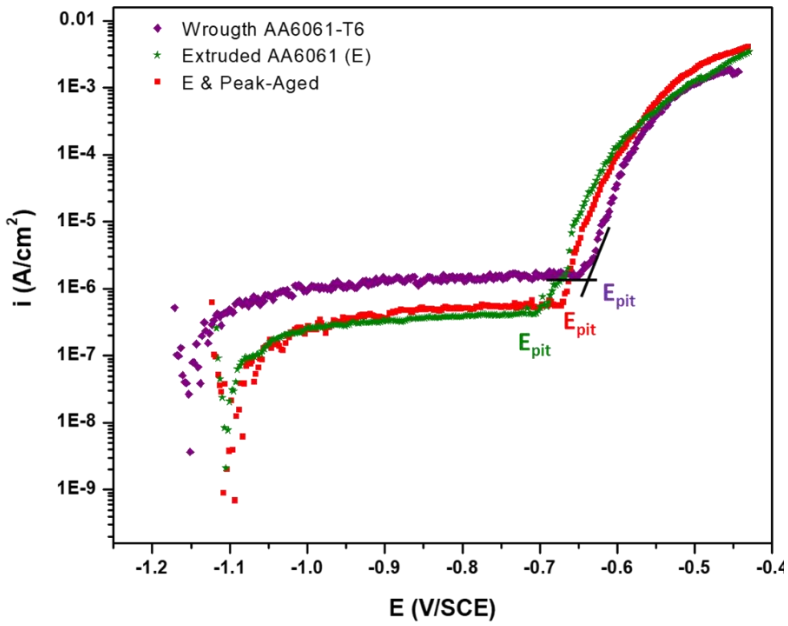

Figure 38: Polarizations plots of the Wrought AA6061-T6 (diamond), As-extruded (star) & Extruded & peak aged (square) materials in a deaerated 0.1M NaCl solution.

Besides, the wrought and ECAPed materials display a passive behavior in the diluted NaCl solution characterized by a passivation plateau between E_{corr} and the breakdown potential (E_{pit}). The passive current density is higher for the wrought AA6061-T6 material than the ECAPed materials, indicating that passive film formation is easier after ECAP regardless of the post-aging treatment. This is explained by the increase of number of defects (grain boundary, dislocation, particles) in the material after ECAP as oxygen diffusion is faster on such defects than in the bulk[103]. Enhancement of passive film formation after grain refinement was also reported for other nanocrystalline materials[139, 140]. In contrast Brunner et al. did not find increase in passivation behavior for an UFG Al-Mg alloy after 4 ECAP passes when compared to its course grain

counterpart[99]. The study reported that ECAP processing and the increase in GB and dislocation densities do not seem to affect passive film formation[99]. Here the material under study is a heat treatable Al-Mg-Si alloys with a high density of precipitates and intermetallic compounds compare to non-heat treatable Al-Mg alloy. Therefore oxygen diffusion, and passivation are enhanced after ECAP. To study passivation behavior before and after ECAP processing, we compared the level of passive current density in the 0.1M NaCl solution. However, the use of a chloride-rich environment may affect the passive current density due to the formation of metastable pits in the passive region that cannot be capture during the polarization. Therefore the comparison of passive current density to assess passivation should be done with caution. Figure 38 shows that the pitting corrosion (E_{pit}) potential of the wrought AA6061-T6 (~ -635 mV) is slightly higher than that of the as-extruded material (~ -650 mV) regardless of the post-aging treatment. This trend in E_{pit} suggests that ECAP processing slightly decreases the stability of the passive film. This may be attributed to the high volume fraction of fragmented cathodic AlFeSi intermetallic compounds after ECAP that increase the density of local micro galvanic cells in the material.

4.3.5 Sequence of Corrosion Events

The anodic current density of both extruded materials is similar between E_{pit} and ~ 550 mV while being one order of magnitude higher than that of the wrought AA6061-T6. This is not in agreement with the trend observed in the aerated 1M NaCl (Fig. 32) as the anodic current density of the as-extruded material was similar to the wrought AA6061-T6 and lower than that of the peak-aged sample. Thus, in this range of potential ECAP processing increases significantly anodic dissolution kinetics regardless of the post-aging treatment. The differences in anodic current density are less pronounced above -550 mV although the extruded and peak-aged material show

the highest level of current among all three materials. The slope of the anodic current density of the three materials changes around -600 mV indicating a change in anodic reaction.

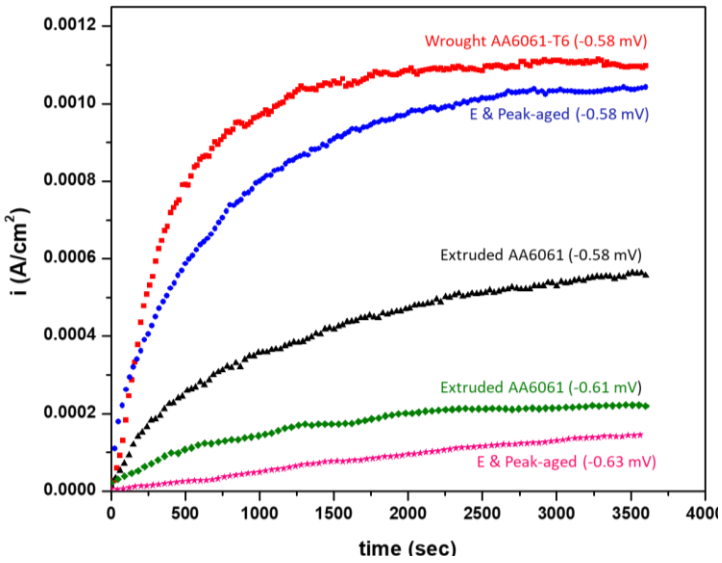

Figure 39: Potentiostatic polarization curves for the wrought AA6061-T6, Extruded & peak aged and the as-extruded AA6061 materials at -0.58 mV, -0.61 mV and -0.63 mV.

To elucidate the sequence of corrosion events (pitting and filiform corrosion), we ran potentiostatic polarization tests at several potentials around E_{pit}, and -600 mV. Figure 39 shows the evolution of anodic current density of the extruded and peak aged material near E_{pit} (-630 mV). There is a linear increase in current as a result of passive film breakdown and formation of stable pits. Above E_{pit} at (-610 mV) the anodic current density of the as-extruded material increases faster with time. The analysis of its exposed surface display small isolated pits with no filiform corrosion at their vicinity and isolated regions with filiform corrosion along the shear direction (Figure 40a). Thus, filiform corrosion and pitting seem to occur simultaneously in this range of potential when no aging treatment is performed. Also pitting does not always induce filiform corrosion along the shear direction, and the filiform corrosion does not necessarily start by pitting at the AlFeSi

intermetallic compounds. Indeed the filiform corrosion is explained in the literature by the high stored energy (high dislocation density) in that region that promotes the dissolution of the entire grains. Figure 39 shows the potentiostatic response of the wrought 6061-T6 and the ECAPed materials at -580 mV. They all display similar evolution of anodic current density as in Figure 34

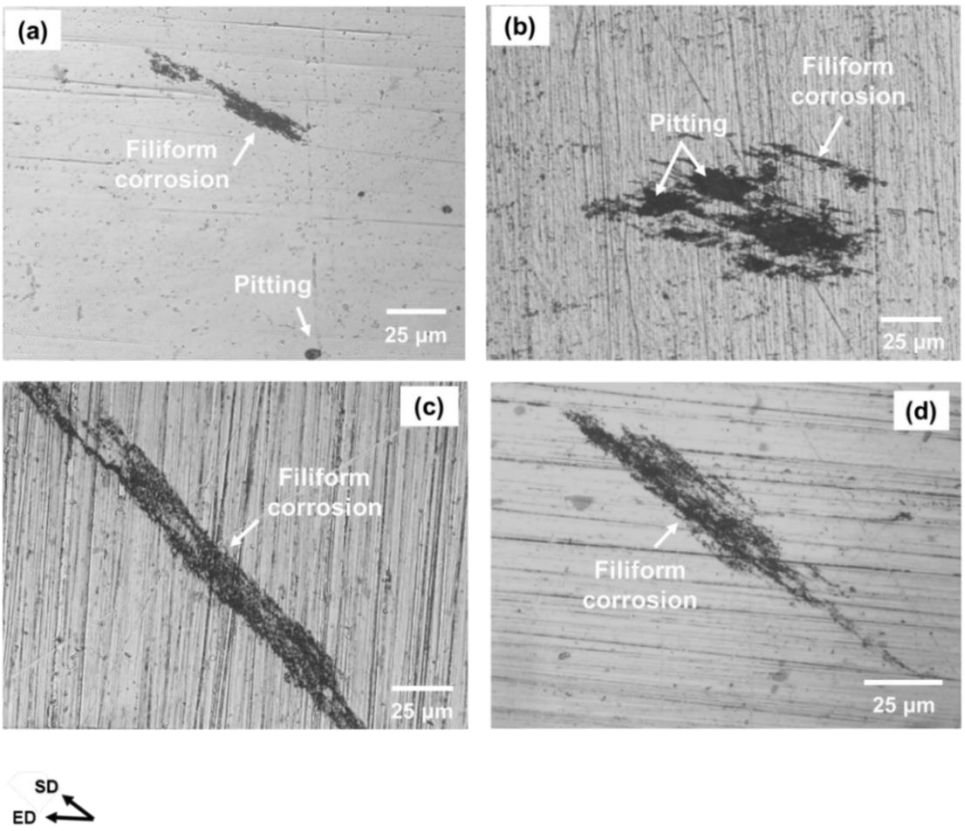

Figure 40: State of the exposed surfaces at the end of the potentiostatic polarization test (a) as-extruded material at -630mV. (b) & (c) extruded & peak-aged materials at -610 mV. (d) as-extruded material at -580 mV.

with a sharp increase up to 1000 seconds followed by a plateau. Although the potentiodynamic curve of the three materials near -580 mV are close to each other, the as-extruded material shows the lowest level in anodic current density among all. The state of the peak-aged material surface at the end of the potentiodynamic test at -580 mV shows several closely-spaced pits surrounded

by filiform corrosion similarly to the ones observed in the aerated 1M NaCl solution (Figure 40b). They seem to have nucleated at the closely spaced AlFeSi intermetallic compounds[134, 135]. There are also regions with filiform corrosion and no sign of pitting confirming that filiform corrosion is not necessarily associated to pitting at the AlFeSi intermetallic compounds (Figure 40c). Similar observation was made for the as-extruded material at the end of the potentiostatic test at -580 mV (Figure 40d). Although it is complex to elucidate the sequence of corrosion events, pitting and filiform corrosion seem to occur simultaneously and separately in the ECAPed materials regardless of the aging treatment.

4.4 Conclusions

In studying the electrochemical response of UFG Al-Mg-Si alloys we found that:

- The potentiodynamic and potentiostatic responses of UFG AA6061 after ECAP are greatly influenced by the precipitation within the shear bands after a low-temperature post-aging treatment (100 ˚C up to 3 days). The anodic dissolution and the severity of the IGC are the highest after peak aging.
- The corrosion attack is characterized by pitting at the AlFeSi compounds surrounded by filiform corrosion along the shear direction and within the shear bands of the material (regardless of the post-aging treatment).
- Filiform corrosion, IGC, and pitting around the AlFeSi intermetallic compounds and the MgSi precipitates are the four main corrosion manifestations after ECAP and post-aging treatment.
- Potentiostatic polarization tests in aerated 0.1M NaCl solution show that filiform corrosion (along the shear direction) and pitting occur simultaneously and separately. However,

pitting does not always lead to filiform corrosion, and the filiform corrosion does not necessarily start by pitting at the AlFeSi intermetallic compounds.

- The passive current density increases after ECAP regardless of the post-aging treatment. Such improvement in passivation is due to the grain refinement, and the high density of dislocation and precipitates in the material after processing.
- The pitting potential decreases after ECAP and aging because of the high density of micro-galvanic cells in the material (fragmented AlFeSi IMCs and Mg_2Si precipitates). Thereby the passive film is less stable.

5. INFLUENCE OF DYNAMIC RECRYSTALLIZATION AND SHEAR BANDING ON THE LOCALIZED CORROSION OF SEVERELY DEFORMED Al-Mg-Si ALLOY*

5.1 Introduction

Dynamic recrystallization (DRX), and dislocation annihilation are two collaborative grain refinement mechanisms occurring during severe plastic deformation[39] such as equal channel angular pressing (ECAP). DRX is promoted during ECAP through the formation of narrow regions of intense shearing and straining so-called shear bands[141]. These bands undergo rapid heating and fast cooling within a fraction of millisecond during deformation[40]. Their formation mechanism, microstructure, and thermomechanical response have been extensively studied in the literature for aluminum[142], titanium[42], stainless steel[41], and magnesium[143] alloys. Recently, Meyer et al. proposed a revised rotational DRX model to explain grain refinement during ECAP of pure titanium[42]. The mechanism starts by the accumulation of dislocations within the deformed grains that rearrange into dislocation cells and subgrain boundaries. The subgrains evolve into fine equiaxed grains by rotation thanks to the thermal energy stored in the bands[42]. Earlier, Langdon[28] investigated shear-band evolution for different numbers of ECAP passes and ECAP routes. The study showed that route Bc (90-degree rotation of the bar between each pass) is the most effective route to form fine equiaxed grains rapidly. Afterwards several groups studied how this route affects subgrains size, grain aspect ratio, and grain boundary (GB) characteristics in aluminum alloys[37, 38, 43]. The results show that the most significant changes from coarse grain to elongated

* Reprinted with permission from "Influence of dynamic recrystallization and shear banding on the localized corrosion of severely deformed Al–Mg–Si alloy" by Ly, Ramatou, Karl T. Hartwig, and Homero Castaneda, 2018, *Materialia*, 4, pp.457-465, Copyright 2019 by ELSEVIER.

subgrains occur between 0 and 4 passes. At this stage, the microstructure is partially recrystallized. Between 4 and 8 passes (the focus of the current study) the grains become equiaxed and the percentage of high angle boundaries (misorientation > 15 degrees) becomes dominant. The microstructure at the end of this stage is near full recrystallization[37, 38, 43]. High angle grain boundaries (HAGBs), high dislocation density and residual stress were found to enhance localized corrosion due to differences in precipitation[80, 109, 112] and grain-stored energy between the unstrained and strained regions[110, 114]. Pitting and intergranular corrosion are the main localized corrosion manifestations in aluminum alloys when no external stress is applied. Pitting mainly occurs near cathodic particles located inside the grains[48] while IGC is a selective attack near anodic or cathodic GB precipitates. In aluminum alloys, IGC is governed by the aging treatment (temperature/time) and the amount and nature of alloying elements such as Cu[128, 107]. In addition, when peak aging treatment is performed following a strain hardening process[81, 128], the IGC resistance of Al-Mg-Si alloy decreases due to the formation of precipitate free zones (PFZ), and grain boundary Cu-rich precipitates at the HAGBs ($Al_4Cu_2Mg_8Si_7$)[81, 128]. In recent years, the corrosion susceptibility of severely deformed aluminum alloys has been extensively studied after different processing routes [94, 98, 99]. Most of this work investigated how grain size and particle fragmentation influence corrosion without considering the effects of dynamic recrystallization through shear banding. To better understand corrosion in ECAPed Al-Mg-Si alloys, we recently learned that shear bands play a decisive role in the localized corrosion of partially recrystallized AA6061 due to differences in precipitation and particles distribution between the matrix and the shear bands[135]. Here we investigate the combined effects of dynamic recrystallization and peak aging on corrosion near full recrystallization. Our results indicate that the higher the percentage of recrystallized grains, the higher the strength of the material, and the lower the localized corrosion.

The location and morphology of corrosion attack suggest that the energy stored in the grain influence the IGC susceptibility of severely deformed AA6061 more than GB precipitation.

5.2 Experimental Procedure

5.2.1 Materials and Processing

The material investigated is a wrought AA6061 aluminum alloy (maximal nominal composition Si 0.8 wt%, Fe 0.7 wt%, Mg 1.2wt% Cu 0.40wt%, Mn 0.15wt%). ECAP processing was carried out at 125 ˚C using a sliding wall ECAP 90-degrees die and a backpressure of 28 MPA. The material was initially annealed at 530 ˚C for 3h in air, water quenched, and preheated at 125 ˚C for 30 min in the die before extrusion. The material was cooled down in air between each ECAP pass. A maximum of 7 passes (N=7) following Route Bc at a pressing speed of 5 mm/sec was achieved as a higher number of passes induced cracks formation in the extruded bars (Fig. 41). The bars were all aged at 100 ˚C for 2 days twenty four hours after extrusion[43]. We explained the choice of a common heat treatment temperature and time regardless of the number of ECAP passes in the following sections.

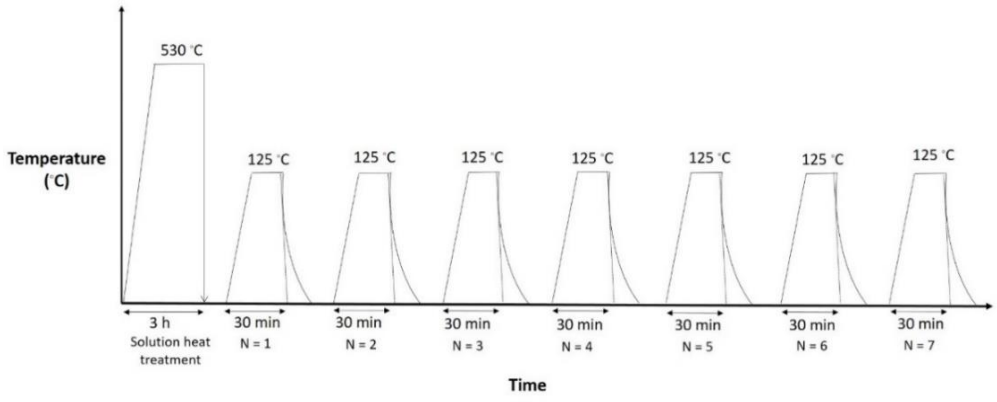

Figure 41: Time/temperature profile of the material during the solution heat treatment and the ECAP processes up to 7 passes.

5.2.2 Vickers Hardness

Vickers hardness measurements were taken on the workpiece side plane normal to the extrusion direction of the bars after ECAP and peak aging. The goal was to investigate strengthening effects, through DRX and precipitation hardening on localized corrosion susceptibility. During hardness measurements, a load of 100 g was applied for 10 sec with a diamond indenter. The average hardness was obtained by making a total of 10 indents on a polished surface prepared with silicon carbide (SiC) paper.

5.2.3 Microstructure Analysis

The shear band network and particle distribution were investigated after extrusion by optical microscopy and a TESCAN FERA 3 MODEL scanning electron microscope (SEM). Composition depth profile analyses were carried out on a clean and grounded surface with a secondary ion mass spectrometry (SIMS) CAMECA IMS 4f detector and Ion-spec commercial software. The goal was to investigate the existence of chemical segregation within the bulk material. For that, we bombarded a 250 x 250 μm^2 surface area with a positive O_2 ion beam (6 KeV, 0.85 10^{-6} A) at a sputtering rate of 12 nm/sec while maintaining a pressure of 10^{-5} Pa inside the SIMS chamber.

We took advantage of the high lateral resolution of the atomic force microscope (AFM) and its good topography contrast to investigate precipitate morphology and distribution after the peak-aging treatment. We acquired Volta potential distributions using the scanning Kelvin probe force microscopy (SKPFM) technique coupled with the AFM. The analyses were carried out with a BRUCKER dimension Icon AFM and Nanoscope 9.1 software. Topography and Volta potential

maps were acquired with an OSCM-PT-R3 probe (20 nm radius). The data acquisition and processing procedures are described in detail in our previous study[135].

5.2.4 Corrosion Immersion Tests

The accelerated standard ISO 11846 (Method B) test was used to assess the intergranular corrosion susceptibility of the samples after ECAP followed by peak-aging. Samples were etched before the immersion test to reveal the GBs and evaluate their sensitivity to IGC. For the testing, a 1 cm^2 sample was cut from the center of each bar mounted, polished, immersed in the testing solution (30g NaCl/L and 10 ml HCl/L (pH ~1)) and removed after 24 hours for investigation[135]. The severity of the IGC attack was assessed by metallographic cross section analysis.

5.3 Results and Discussion

5.3.1 Microstructure Evolution with Processing

5.3.1.1 Dynamic Recrystallization

Figure 42a, 42b, and 42c represent the etching response of the materials respectively after 3, 5 and 7 passes. There is a clear difference in contrast between the recrystallized regions (dark) and the unrecrystallized ones (bright) due to different etching responses. Therefore, the percentage of over etched areas indicates the level of DRX after each pass. Three ECAP passes at 125°C lead to a partially recrystallized microstructure with a well-defined shear band network (dark, narrow bands). After 5 ECAP passes, the percentage of recrystallized region increases while the spacing between the shear bands decreases (Fig 42b). Their length and spacing decrease further after 7 passes as the microstructure is near full recrystallization[37, 38, 43]. The dark spots, more visible in Figure 42a, correspond to etch pits around the intermetallic compounds.

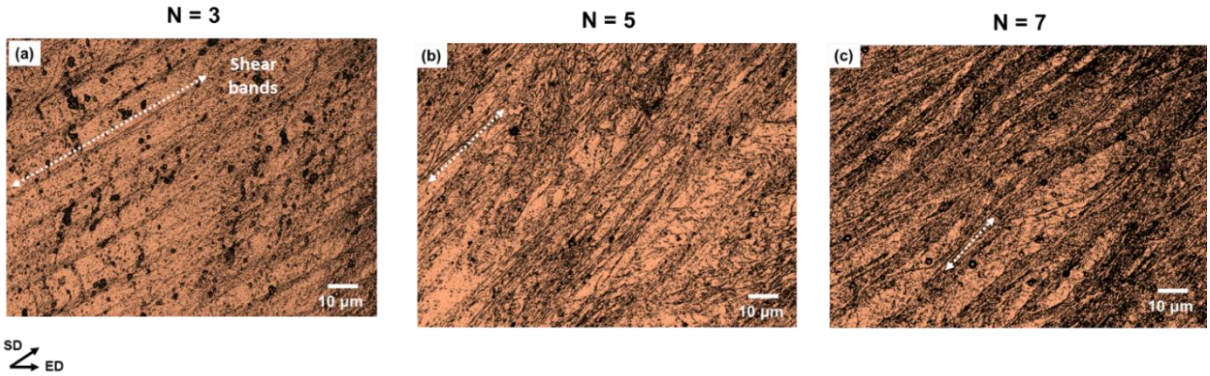

Figure 42: Optical microscope picture of the etched microstructure after ECAP and peak aging (100 °C for 2 days) showing the shear band network and recrystallized regions (dark): (a) 3 ECAP passes, (b) 5 ECAP passes, and (c) 7 ECAP passes (SD = shear direction, ED= extrusion direction).

5.3.1.2 Intermetallic Compounds

Figure 43 shows the respective SEM images of the etched microstructures displayed in Figure 42. The bright coarse particles represent AlFeSi intermetallic compounds (IMCs) whom distribution and size change significantly with the number of ECAP passes. Indeed, they are fragmented and redistributed along the shear direction after 3 ECAP passes[135]. The IMCs become smaller and homogeneously distributed in the matrix as the number of passes increases to 7 due to particle shearing and the 90-degree rotation of the bar[104]. It is well known that Fe-rich intermetallic compounds are preferred sites for pitting in aluminum alloys because of their high cathodic electrochemical potential. In Al-Mg-Si alloys, these IMCs exist mainly as β-Al_5FeSi and α-Al_8Fe_2Si phases. The AlFeSi distribution controls the severity of pitting corrosion regarding pit density and size; the larger and closer the AlFeSi compounds are, the larger the pits will be. Fe being a critical element in the material because of IMCs formation; we assessed the exact amount of Fe by induced coupled plasma mass spectrometry analysis. The results reveal a maximal composition of 0.33 wt% of Fe in the alloy under study which is lower than the composition limit of 0.7 wt%. We also took a closer look at the intermetallic distribution within the bulk material

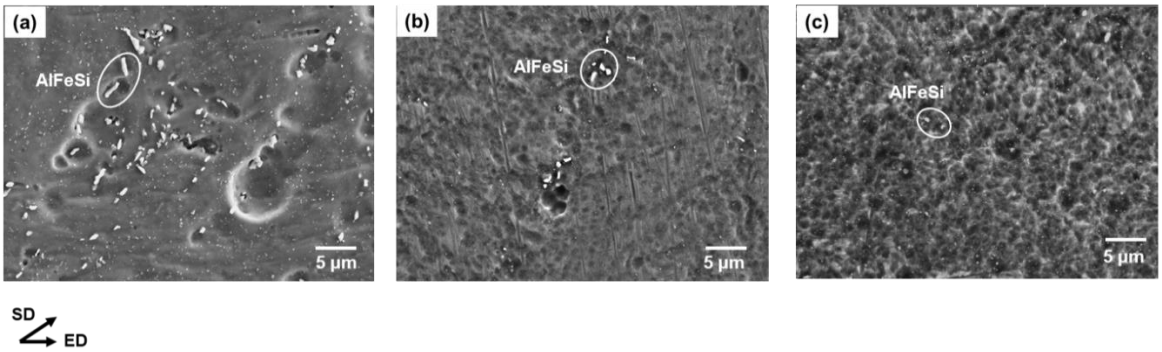

Figure 43: SEM pictures of the etched microstructure after ECAP and peak aging (100 ◦C for 2 days) showing fragmented AlFeSi compounds: (a) 3 ECAP passes, (b) 5 ECAP passes, and (c) 7 ECAP passes.

after each ECAP pass. For that, we ran composition depth profile analyses on Fe by TOF-SIMS [135]. Figure 44 displays the results over a 250 µm x 250 µm area sputtered for 1hr where the bright pixels indicate the location of Fe, and therefore that of AlFeSi compounds. Fig. 44a, 44d, and 44g represent the materials' top surface after 3, 5 and 7 ECAP passes respectively. The Fe-pixels distribution agrees with the etched microstructure (Fig. 43). Indeed, we can identify isolated regions of segregated Fe-pixels (AlFeSi) along the shear direction after 3 passes (Fig. 44a). The Fe become less segregated and homogeneously distributed as the number of passes increases up to 7 (Fig. 44d, 44g and 44b, and 44c). Thus, smaller corrosion pits are expected after 7 ECAP passes than 3 ECAP passes. We investigated the bulk composition by sputtering the surface up to 1 hour and removing about 50 µm of aluminum layer. The position of the Fe-pixels in Figures 44b and 44c barely changes with sputtering time confirming our previous results at room temperature: the IMCs are redistributed closely under each other in the shear planes of the material[135]. In contrast, the Fe distribution changes with the sputtering time after 5 and 7 passes (Fig. 44d – 44i) as an indication of a more homogeneous bulk composition. In other words the higher the number of ECAP passes, the better the AlFeSi distribution is within the bulk. Nevertheless, AlFeSi segregation along the shear direction persists after 7 passes (white circle, Fig. 44g – 44h).

Therefore, a high number of ECAP passes is needed to break the IMC interconnectivity and reduce pitting along the shear direction during corrosion.

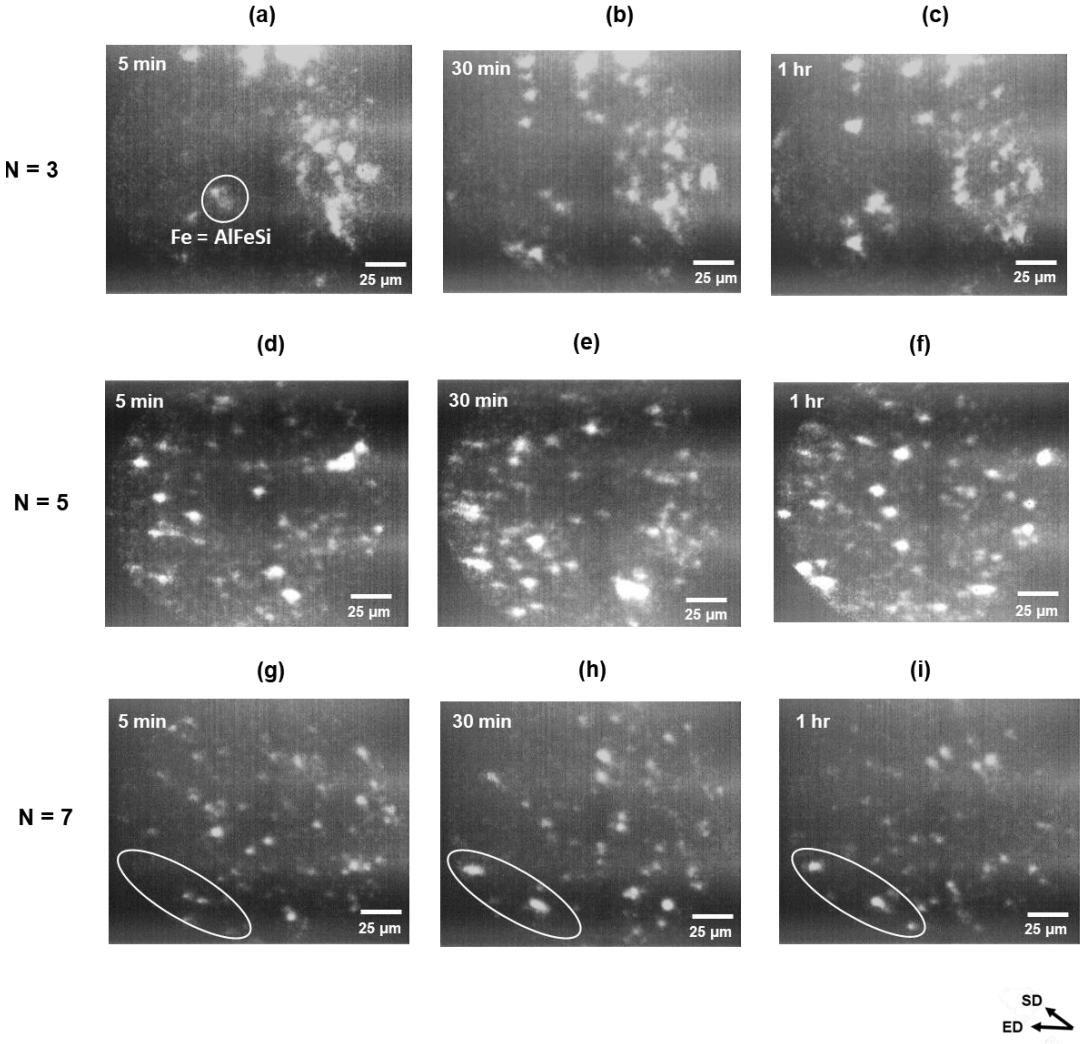

Figure 44: SIMS - Composition depth profile analysis results for Fe distribution after 3 ECAP passes (N=3), 5 ECAP passes (N=5), and 7 ECAP passes (N=7). Results after 5 min sputtering (a), (d), (g), 30 min sputtering (b), (e), (g), and 1hr sputtering (c), (f) (i).

5.3.1.3 Precipitation Hardening

In this study, we aged all the extruded materials (3, 5 and 7 ECAP passes) at 100 ˚C for 2 days after ECAP. It was reported that peak hardness in this material is reached for such a

combination of aging temperature and time, regardless of the number of ECAP passes[49]. In other words, precipitation kinetic is not influenced by the number of passes, although the material's thermomechanical history changes with processing. However, the precipitate size slightly increases[43]. This may be attributed to an existing competition between dislocations formation and grain boundary creation during dynamic recrystallization[39]. Indeed, precipitation in severely deformed materials mainly occurs at the dislocations and the grain boundaries. During ECAP, the dislocation density inside the subgrains increases sharply up to 4 passes[37, 38]. Their number either reaches a plateau (due to saturation)[37] or slightly decreases (by annihilation) between 4 and 8 passes[37, 38]. Meanwhile, the percentage of high angle boundary boundaries increases as a result of grain refinement. Thereby, precipitation kinetics is not affected by dynamic recrystallization. In our previous work, we found that shear bands are preferred sites for precipitation and corrosion manifestations in partially recrystallized AA6061[135]. As shear banding decreases during DRX, here we investigated how precipitation hardening and the Volta potential difference (VPD) between the AFM tip and the material evolves when the microstructure is near full recrystallization (after 7 passes). Volta potential is an indirect measurement of the electron work function defined by the minimum energy needed to remove electrons away from a surface in vacuum[144]. It is a sensitive measurement that provides useful information on surface reactivity (matrix, particles precipitates) and therefore corrosion susceptibility[119, 135]. Fig 45a shows the AFM topography map over a 50 x 50 μm surface after 7 ECAP passes and peak aging. The coarse particles represent the fragmented AlFeSi compounds previously characterized by SEM and TOF-SIMS analyses. They remain aligned along the shear direction after 7 ECAP passes, as observed above. The largest AlFeSi IMCs are ~ 76 nm high, and ~ 2 μm wide. There are several small particles along the shear direction more apparent in the Volta potential difference map (Fig 45b). In this map, we can

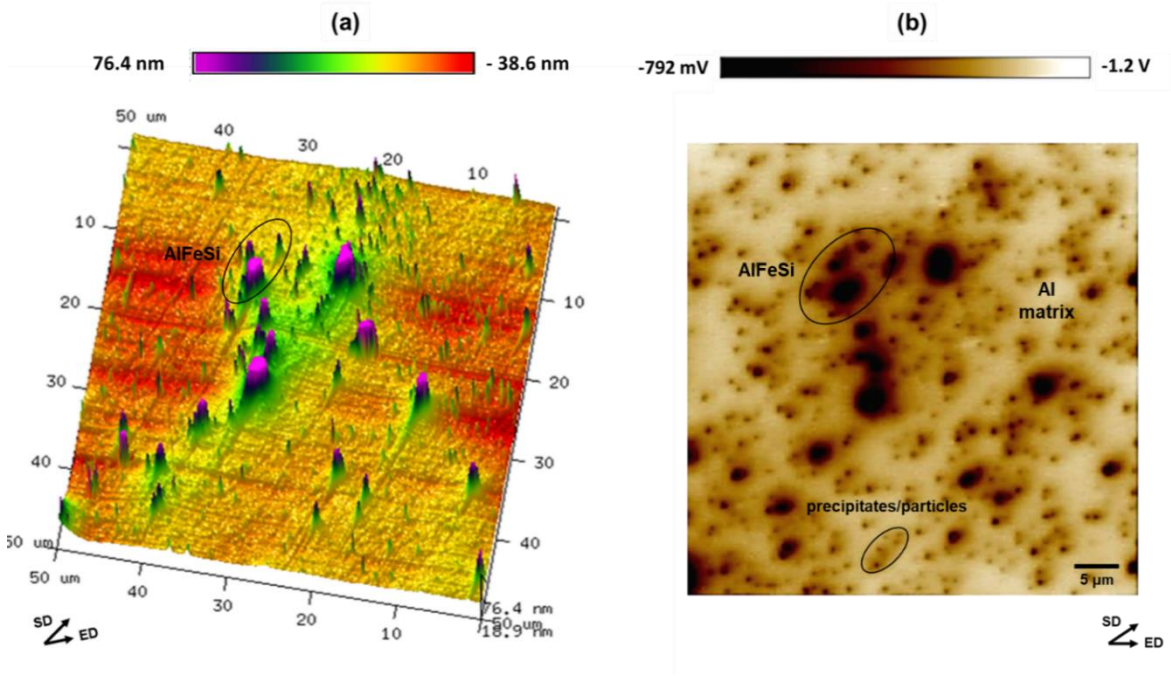

Figure 45: (a) AFM topography map after 7 ECAP passes showing AlFeSi compounds. (b) Volta potential distribution map.

distinguish the aluminum matrix (Al) which corresponds to the bright regions of lowest VPD (-1.05V), a sign of high surface reactivity. We can also distinguish coarse AlFeSi compounds in black with higher VPD (-0.7 V). Such a VPD distribution suggests that particles with higher VPD than the matrix will most likely induce pitting during corrosion. It is difficult to differentiate whether the small particles visible along the shear direction correspond to the fragmented AlFeSi compounds or the hardening precipitates (Figure 45b). Nevertheless, these particles have higher VPD than the aluminum matrix. Thus, small corrosion pits are expected to form in their vicinity during corrosion. In this material, we did not notice isolated regions of segregated particles along the shear direction as it was the case for the partially recrystallized microstructure (3 ECAP passes) in our previous study[135]. Such a difference in precipitate distribution with the number of ECAP passes may result from a decrease of shear banding effects during DRX.

5.3.2 Corrosion Immersion Tests

5.3.2.1 Cross Section Analysis

IGC susceptibility was investigated by immersion testing in an acidified NaCl solution (pH~1) according to the standard ISO test 11846 (Method B). Metallographic cross-section analysis is the most common technique to assess IGC susceptibility. Figure 46 shows the state of the material's cross section after a 24 hour immersion. There is a strong influence of processing on the morphology of the IGC attack. Indeed, after 3 passes, the IGC propagated vertically within the material as bands (Fig. 46a). Several interconnected pits are visible in the cross-section as a result of the AlFeSi IMCs distribution under each other (Fig. 44a, 44b, and 44c). Both the IGC penetration depth and the spacing of the corroded bands decrease up to 7 passes (Fig. 46b and 46c). The 45-degree propagation of the IGC, similar to the shear plane orientation, is more evident after 5 and 7 passes. This observation suggests that the shear planes are highly susceptible to

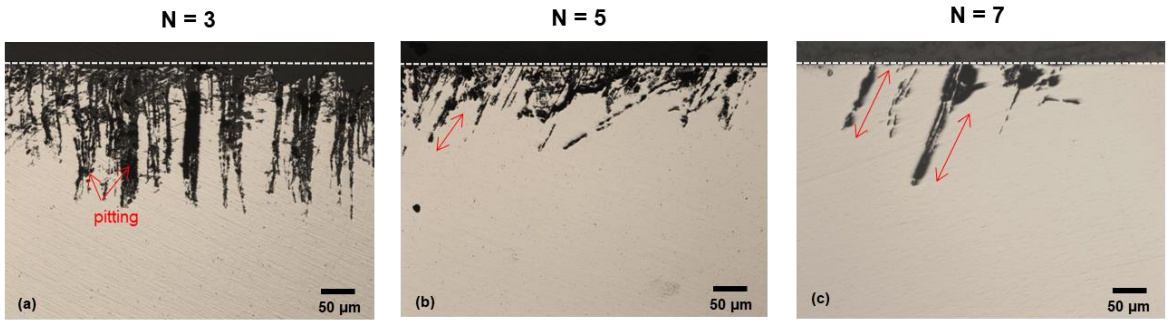

Figure 46: Cross section micrographs after a 24 hour immersion test in 30g NaCl/L + concentrated HCl (pH ~1): (a) 3 ECAP passes, (b) 5 ECAP passes, and (c) 7 ECAP passes followed by peak aging.

corrosion. The number of corroded bands and the width of the corrosion right below the top surface substantially decrease with the number of passes. However, there is no noticeable difference in propagation depth between 3, 5 and 7 ECAP passes.

5.3.2.2 Exposed Surfaces

To get more insights into the differences in IGC morphology with the number of ECAP passes, we investigated the exposed surfaces of the material after a 24-hour immersion test. Several large pits were visible after 3 passes (Fig. 47a) as a result of the close spacing of AlFeSi compounds and their higher VPD than the aluminum matrix (Fig 45b). The pit size significantly decreases after 5 and 7 passes (Fig. 47b and 47C) following the conclusion from the SIMS results. Hence, the higher the number of ECAP passes, the smaller the AlFeSi IMCs, and the smaller the pits. Figures 47a shows that after 3 passes the shear bands of the material represented by the narrow dark parallel bands are corroded entirely while the surrounding matrix (non-recrystallized grains) is not. We previously explained the preferred dissolution of the shear bands relative to the matrix by the differences in GB characteristic (HAGB) and precipitation[135]. We suggested that once the corrosion starts by pitting near the AlFeSi compounds, it does not spread outside the shear bands because of the low density of precipitates in that region that does not provide enough driving force for corrosion[135]. When the number of ECAP passes increases up to 5, the size and length of the corroded bands along the shear direction decrease significantly (Fig 47b). After 7 passes (Fig. 47c),

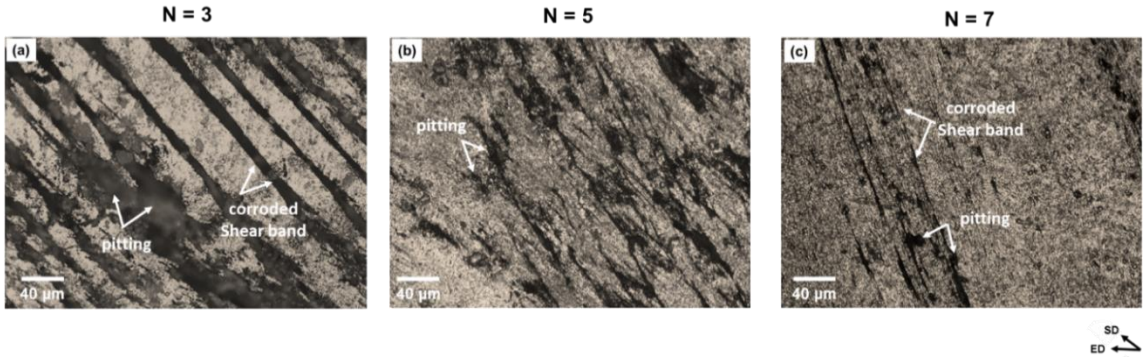

Figure 47: Optical microscope image of the exposed surface after a 24 hour immersion test in 30g NaCl/L + concentrated HCl (pH ~1): (a) 3 ECAP passes, (b) 5 ECAP passes, and (c) 7 ECAP passes followed by peak aging.

their number, size, and length decrease further in accordance with the shear band network revealed by etching in Figure 42. Figure 47a shows the SEM image of the surface at the end of the 24-hour immersion test. Interestingly, the recrystallized grains along the shear direction dissolved entirely while the surrounded matrix exhibits pitting only. Therefore, shear bands are preferred regions for corrosion even when the fraction of recrystallized grains and HAGBs in the material increase[37, 38, 43]. As a conclusion, the smaller the shear bands, the lower the surface reactivity and the width of the IGC.

To get more insights into the differences in reactivity between the recrystallized grains along the shear direction and the ones in the matrix, we immersed the material after 5 ECAP passes in the same NaCl solution for a shorter time (5 hours). The corrosion attack is characterized by elongated closely spaced pits, and filiform corrosion around the pits (Fig. 48a) reported as crystallographic pitting corrosion in the literature[94]. We took a closer look at the locations where the filiform corrosion developed and the ones where it did not. These regions are marked in Fig 48b as number 1 and 2 respectively. Figure 48c reveals that filiform corrosion developed preferentially where the grains are elongated along the shear direction. Indeed, we can identify them by their corresponding grain boundaries (bright lines) revealed by etching before the immersion test. Such grain morphology is characteristics of heavily deformed grains most likely located within the shear bands of the material[37, 38, 43]. We can distinguish multiple small pits in the matrix as well. Figure 48d shows one of the regions with no manifestation of filiform corrosion (red square). The surface exhibits large isolated pits as a result of the close spacing between the AlFeSi compounds. More noticeably, there are several small pits in the matrix. Their distribution agrees with that of the small particles with high VPD (Figure 45b). The etched grain boundaries suggest an equiaxed morphology which may correspond to the recrystallized grains that formed

during DRX. As a conclusion, filiform corrosion is the dominant corrosion manifestation in the heavily deformed grains along the shear direction while pitting mainly occurs in regions of small equiaxed grains.

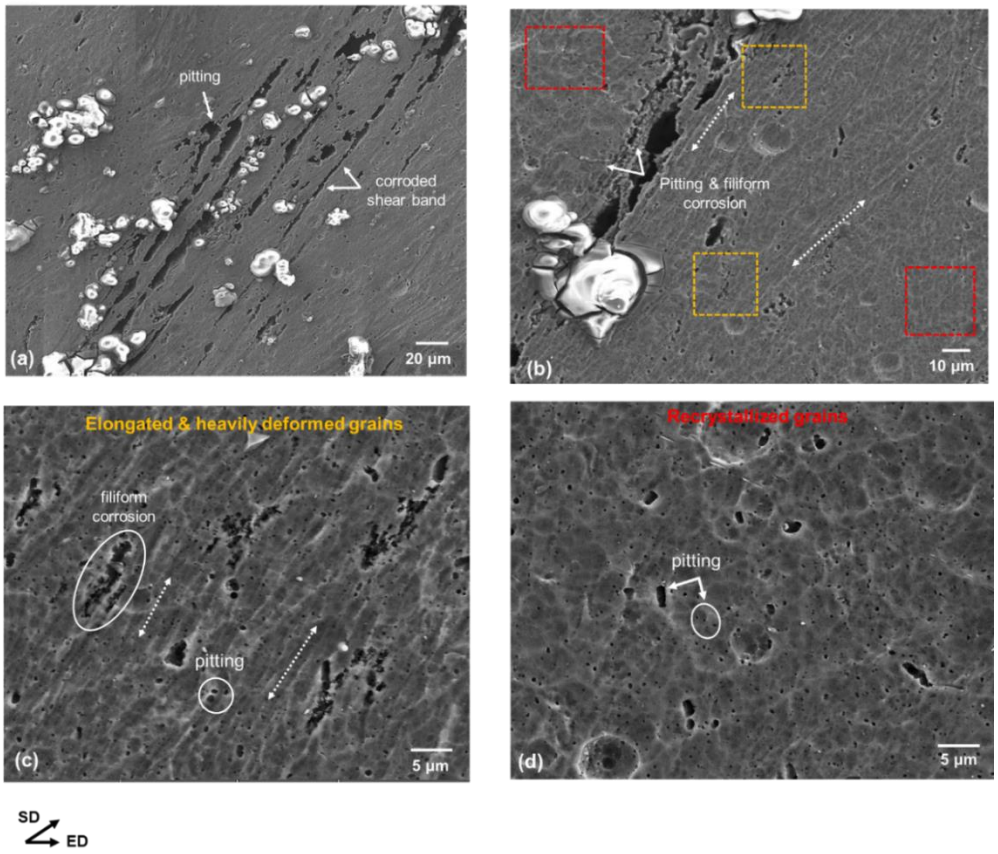

Figure 48: SEM images of the exposed surface: (a) 7 ECAP passes + peak aging and 24 hours immersion test, (b) 5 ECAP passes + peak aging and 5 hours immersion test, yellow square indicates the heavily deformed region, and red square indicates recrystallized region, (c) zoom inside the yellow square showing filiform corrosion and pitting in the heavily deformed region, and (d) zoom inside the red square showing pitting only in the recrystallized region.

5.3.2.3 Corrosion Susceptibility of the Recrystallized Grains

Several studies have reported that the IGC susceptibility of extruded Al-Mg-Si alloys is either more severe or restricted in the recrystallized regions, and thereby depends on the fraction

of recrystallized grains[80, 128]. This is not the case in our study. Although the IGC is confined to the shear bands, the higher the number of ECAP passes, the higher the fraction of recrystallized grains, and the lower the reactivity of the surface (Fig. 47). The AFM topography and VPD maps after 7 passes (Fig. 45) did not show noticeable differences in precipitation and VPD in the material as it was the case for the partially recrystallized microstructure (3 passes)[135]. Thus, the differences in corrosion manifestation between the recrystallized grain inside and outside the shear bands cannot be explained by precipitation phenomena alone. Besides precipitation, the level of residual strain and dislocation density are two well-known contributing factors to corrosion[102, 114]. Indeed, some studies reported grain dissolution in highly strained regions with high dislocation density (high stored energy) but no evidence of GB precipitates[110, 111, 114]. Hence, a correlation may exist between high grain stored energy, thermodynamic instability, and high electrochemical activity[110, 111, 114]. Shear bands are regions of HAGBs and high residual stress. Their higher corrosion level than the other recrystallized regions observed in this study suggests that in ECAPed AA6061, grain stored energy plays a more critical role in IGC susceptibility than GB characteristics and precipitation.

5.4 Conventionally Extruded AA6061-T6

In the current study, we assessed the corrosion susceptibility of conventionally extruded AA6061-T6 in parallel with the ECAPed materials. The goal was to investigate how ECAP processing influences the IGC resistance of AA6061 using conventionally extruded AA6061-T6 as a reference. For that, we immersed the conventionally extruded samples in the same concentrated NaCl solution for 24 hours. Figure 49 shows that the material exhibits uniform IGC with pitting along the extrusion direction (ED). It is known that the AlFeSi compounds aligned close to each other along the extrusion direction during processing[110] explaining the pit distribution

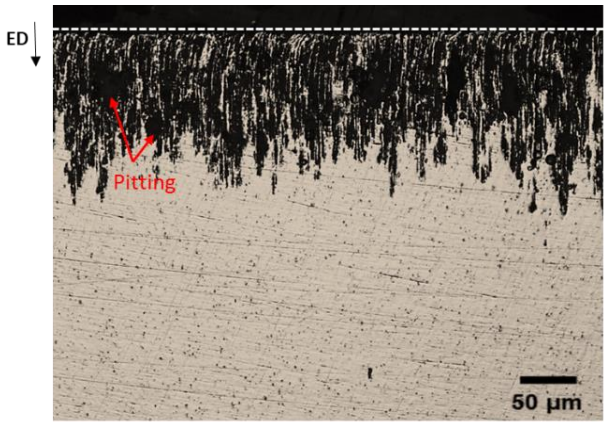

Figure 49: Cross section view of the conventional extruded AA6061-T6 after a 24 hour immersion test showing pitting inside the IGC (ED = extrusion direction).

in Figure 49. Such IGC morphology was explained in the literature by (i) the nature of the GB (HAGBs)[80] (ii) the existence of Cu-rich GB precipitates at the HAGBs (AlCuMgSi, CuSi, and SiMgCu)[128,], (iii) and the formation of PFZs in the vicinity of the HAGBs[80, 128]. Thus, the extrusion and shear directions are highly susceptible to localized corrosion in conventionally extruded AA6061 and ECAPed AA6061, respectively.

5.5 Strength/Corrosion Resistance Relationship

Figure 50 represents the evolution of Vickers hardness and IGC attack morphology as a function of the ECAP processing route. First, there is a substantial increase in hardness between the conventionally extruded AA6061-T6 material on the one hand (~110 HV) and the ECAPed sample on the other (~150 HV). This is mainly attributed to DRX and the creation of a high density of dislocations and precipitates during processing[108]. The hardness increases slightly between 3 and 7 ECAP passes from ~150 HV to ~160 HV as a result of DRX, and precipitation hardening effects[108]. Interestingly, the severity of the IGC barely changes after 3 ECAP passes compared to the conventionally extruded AA6061. The most significant improvement in IGC resistance occurs

after 5 passes (~153 HV) and persists till 7 passes (~160 HV). In other words, the higher the strength of ECAPed AA6061 is, the higher the IGC resistance. Although the width of the corrosion attack is significantly higher for the conventionally extruded material than the ECAPed sample

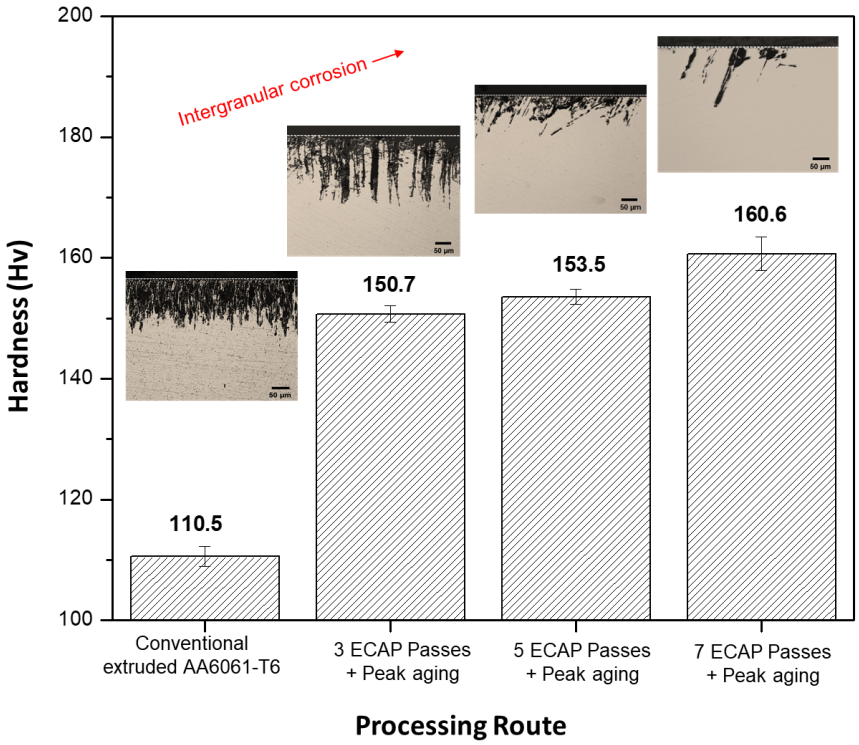

Figure 50: Evolution of Vickers Hardness and IGC morphology as function of the processing route.

after 7 passes, they both possess similar IGC propagation depths. Therefore, DRX and peak aging decrease surface reactivity without slowing down the propagation of IGC. Such a strength/corrosion relationship is not observed in conventionally extruded aluminum alloys as GB precipitation plays an essential role in IGC[80, 128]. This rule breaks with ECAP because the energy stored in the grains and the shear band network seems to influence IGC resistance more than the

precipitation. Figure 51 summarizes the main results of this study, and shows how IGC propagation evolves between conventional extruded AA6061-T6, ECAPed AA6061, partially

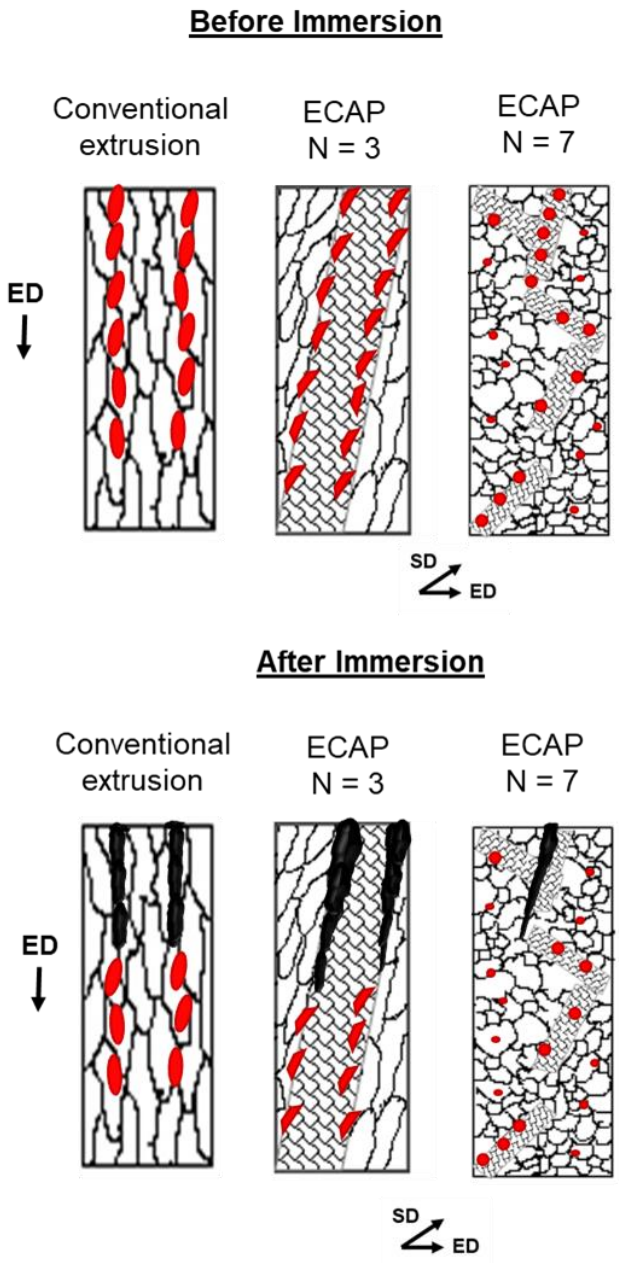

Figure 51: Proposed mechanism for IGC propagation in conventional extruded AA6061 and severely deformed AA6061 after 3 and 7 ECAP passes.

recrystallized AA6061 (3 passes), and almost fully recrystallized AA6061 (7 passes). The typical microstructure of conventionally extruded AA6061 is composed of elongated grains and fragmented AlFeSi compounds along the extrusion direction (Fig. 50a). Fig. 50b illustrates that in this material, the IGC propagates along the grain boundaries because of grain boundary precipitation and formation of PFZ[80, 128] while it is restricted in the shear planes of the ECAPed samples because of the high stored energy in the grains.

5.6 Practical Application

This study shows that it is possible to mitigate IGC in severely deformed AA6061 by reducing shear band formation, a preferred region for corrosion. In practice this is achieved by increasing the number of ECAP passes until the shear bands disappear without changing the peak aging treatment conditions. It is an interesting result as the IGC susceptibility of conventionally extruded AA6061-T6 is usually balanced either by adjusting the amount of Cu in the alloy or the aging time/temperature, which are detrimental to the strength of the material[81, 84].

5.7 Conclusions

In studying how DRX and shear banding affect the corrosion susceptibility of severely deformed AA6061 aluminum alloys we found that:

- DRX and a peak aging treatment (100°C for 2 days) increase the strength and the localized corrosion of severely deformed AA6061 alloys.
- The improved IGC resistance results from a decrease of shear banding effects. The small corrosion pit size observed is attributed to the fragmentation and homogeneous distribution of AlFeSi compounds.

- Modest corrosion in the recrystallized grains outside the shear bands indicates that the energy stored in the grain plays a more critical role in the IGC susceptibility of severely deformed AA6061 alloys than GB precipitation.
- A comparison with conventionally extruded AA6061-T6 demonstrates that shear deformation effectively decreasesIthe IGC susceptibility of extruded and peak aged AA6061. The higher the strength of the material, the lower the IGC susceptibility.

6. SUMMARY

6.1 Conclusions

DRX is effective to simultaneously improve the strength, and the IGC resistance of UFG AA6061 alloys when combined with a low temperature post-aging treatment. This is due to the decrease of shear banding (preferred site for precipitation and corrosion in this material).

In extruded AA6061 the IGC is more affected by grain stored energy than GB precipitation making DRX an effective way to increase resistance to IGC even at peak aging

When ECAP is partially recrystallized, the susceptibility to pitting and IGC is higher than in microstructure near full recrystallization because the shear bands are preferred site for precipitation and therefore corrosion. This result provides a partial explanation to the conflicted literature about the effects of grain size on corrosion, as the shear band have a strong influence on the localized corrosion resistance of the overall material. However their structure depend on the process condition and material initial composition, being process and material dependent,

Passivation is enhanced after ECAP regardless of the post aging treatment because of high level of defect after ECAP. However it is less stable because of high density of micro galvanic cells.

The testing environment influences strongly the effects of the bulk composition on the bulk electrochemical response. The higher the NaCl concentration and the amount of dissolved oxygen are, the higher the effects of precipitation.

The comparison of the strength and IGC resistance of wrought AA6061-T6 with UFG AA6061 indicates that ECAP combined with a low-temperature post aging treatment is beneficial to the material when the microstructure is near full recrystallization (7 ECAP passes). It is not the

case when the microstructure is partially recrystallized (3 ECAP passes). These results provide an additional reason for the conflicted literature.

6.2 Future Work

We studied the electrochemical response of UFG after 3 ECAP passes followed by a low temperature aging treatment. It would be interesting to perform a comparative study after 5 and 7 passes to assess how DRX affects the bulk composition, and the stability of the passive film.

We attempted to elucidate the sequence of corrosion events by performing potentiostatic polarization test at several single ppotentias. However we were not able to fully understand when pitting and filiform corrosion start. Therefore performing potentiostatic test at more potentials combined with SEM analysis will help get more insights into the sequence of corrosion events.

REFERENCES

1. Hatch, J. E. "Aluminum: Properties and Physical Metallurgy (Aluminum Association Inc. and ASM International." (1984).

2. Soboyejo, Wole. *Mechanical properties of engineered materials*. Vol. 152. CRC press, 2002.

3. Callister, William D., and David G. Rethwisch. *Materials science and engineering: an introduction*. Vol. 7. New York: John wiley & sons, 2007.

4. Yamakov, V., D. Wolf, S. R. Phillpot, A. K. Mukherjee, and H. Gleiter. "Deformation-mechanism map for nanocrystalline metals by molecular-dynamics simulation." *Nature materials* 3, no. 1 (2004): 43.

5. Chen, Mingwei, En Ma, Kevin J. Hemker, Hongwei Sheng, Yinmin Wang, and Xuemei Cheng. "Deformation twinning in nanocrystalline aluminum." *Science* 300, no. 5623 (2003): 1275-1277.

6. Han, W. Z., G. M. Cheng, S. X. Li, S. D. Wu, and Z. F. Zhang. "Deformation induced microtwins and stacking faults in aluminum single crystal." *Physical review letters* 101, no. 11 (2008): 115505.

7. Liao, X. Z., F. Zhou, E. J. Lavernia, D. W. He, and Y. T. Zhu. "Deformation twins in nanocrystalline Al." *Applied physics letters* 83, no. 24 (2003): 5062-5064.

8. Rana, R. S., Rajesh Purohit, and S. Das. "Reviews on the influences of alloying elements on the microstructure and mechanical properties of aluminum alloys and aluminum alloy composites." *International Journal of Scientific and Research Publications* 2, no. 6 (2012): 1-7.

9. Edwards, G. A., K. Stiller, G. L. Dunlop, and M. J. Couper. "The precipitation sequence in Al–Mg–Si alloys." *Acta materialia* 46, no. 11 (1998): 3893-3904.

10. Tan, Chee Fai, and Said Mohd Radzai. "Effect of hardness test on precipitation hardening aluminium alloy 6061-T6." *Chiang Mai Journal of Science* 36, no. 3 (2009): 276-286.

11. Cabibbo, M., E. Evangelista, and Maurizio Vedani. "Influence of severe plastic deformations on secondary phase precipitation in a 6082 Al-Mg-Si alloy." *Metallurgical and Materials Transactions A* 36, no. 5 (2005): 1353-1364.

12. Cole, G. S., and A. M. Sherman. "Light weight materials for automotive applications." *Materials characterization* 35, no. 1 (1995): 3-9.

13. Heinz, A., A. Haszler, C. Keidel, S. Moldenhauer, R. Benedictus, and W. S. Miller. "Recent development in aluminium alloys for aerospace applications." *Materials Science and Engineering: A* 280, no. 1 (2000): 102-107.

14. Guillaumin, Valérie, and Georges Mankowski. "Localized corrosion of 2024 T351 aluminium alloy in chloride media." *Corrosion Science* 41, no. 3 (1998): 421-438.

15. Knight, S. P., Nick Birbilis, B. C. Muddle, A. R. Trueman, and S. P. Lynch. "Correlations between intergranular stress corrosion cracking, grain-boundary microchemistry, and grain-boundary electrochemistry for Al–Zn–Mg–Cu alloys." *Corrosion Science* 52, no. 12 (2010): 4073-4080.

16. Tan, L., and T. R. Allen. "Effect of thermomechanical treatment on the corrosion of AA5083." *Corrosion Science* 52, no. 2 (2010): 548-554.

17. Lee, S. H., Y. Saito, T. Sakai, and H. Utsunomiya. "Microstructures and mechanical properties of 6061 aluminum alloy processed by accumulative roll-bonding." *Materials Science and Engineering: A* 325, no. 1-2 (2002): 228-235.

18. Saito, Y., H. Utsunomiya, N. Tsuji, and T. Sakai. "Novel ultra-high straining process for bulk materials—development of the accumulative roll-bonding (ARB) process." *Acta materialia* 47, no. 2 (1999): 579-583.

19. Tsuji, Nobuhiro, Yoshihiro Saito, S-H. Lee, and Yoritoshi Minamino. "ARB (Accumulative Roll-Bonding) and other new techniques to produce bulk ultrafine grained materials." *Advanced Engineering Materials* 5, no. 5 (2003): 338-344.

20. Toroghinejad, Mohammad Reza, Fakhreddin Ashrafizadeh, and Roohollah Jamaati. "On the use of accumulative roll bonding process to develop nanostructured aluminum alloy 5083." *Materials Science and Engineering: A* 561 (2013): 145-151.

21. Gashti, S. O., A. Fattah-Alhosseini, Y. Mazaheri, and M. K. Keshavarz. "Effects of grain size and dislocation density on strain hardening behavior of ultrafine grained AA1050 processed by accumulative roll bonding." *Journal of Alloys and Compounds* 658 (2016): 854-861.

22. Pirgazi, Hadi, A. Akbarzadeh, Roumen Petrov, and Leo Kestens. "Microstructure evolution and mechanical properties of AA1100 aluminum sheet processed by accumulative roll bonding." *Materials Science and Engineering: A* 497, no. 1-2 (2008): 132-138.

23. Zhilyaev, Alexander P., and Terence G. Langdon. "Using high-pressure torsion for metal processing: Fundamentals and applications." *Progress in Materials science* 53, no. 6 (2008): 893-979.

24. Horita, Zenji, David J. Smith, Minoru Furukawa, Minoru Nemoto, Ruslan Z. Valiev, and Terence G. Langdon. "Evolution of grain boundary structure in submicrometer-grained Al-Mg alloy." *Materials characterization* 37, no. 5 (1996): 285-294.

25. Murashkin, M. Yu, A. R. Kil'mametov, and R. Z. Valiev. "Structure and mechanical properties of an aluminum alloy 1570 subjected to severe plastic deformation by high-pressure torsion." *The Physics of Metals and Metallography* 106, no. 1 (2008): 90.

26. Zhilyaev, A. P., G. V. Nurislamova, B-K. Kim, M. D. Baró, J. A. Szpunar, and T. G. Langdon. "Experimental parameters influencing grain refinement and microstructural evolution during high-pressure torsion." *Acta Materialia* 51, no. 3 (2003): 753-765.

27. Segal, V. M. "Materials processing by simple shear." *Materials Science and Engineering: A* 197, no. 2 (1995): 157-164.

28. Langdon, Terence G. "The principles of grain refinement in equal-channel angular pressing." *Materials Science and Engineering: A* 462, no. 1-2 (2007): 3-11.

29. Langdon, Terence G. "Twenty-five years of ultrafine-grained materials: Achieving exceptional properties through grain refinement." *Acta Materialia* 61, no. 19 (2013): 7035-7059.

30. Yamasaki, T., H. Miyamoto, T. Mimaki, A. Vinogradov, and S. Hashimoto. "Corrosion Fatigue of Ultra-Fine Grain Copper Fabricated by Severe Plastic Deformation." *Ultrafine Grained Materials II* (2002): 361-370.

31. Zhilyaev, A. P., D. L. Swisher, K. Oh-Ishi, T. G. Langdon, and T. R. McNelley. "Microtexture and microstructure evolution during processing of pure aluminum by repetitive ECAP." *Materials Science and Engineering: A* 429, no. 1-2 (2006): 137-148.

32. Ferrasse, Stephane, K. Ted Hartwig, Ramon E. Goforth, and Vladimir M. Segal. "Microstructure and properties of copper and aluminum alloy 3003 heavily worked by equal channel angular extrusion." *Metallurgical and Materials Transactions A* 28, no. 4 (1997): 1047-1057.

33. Zhu, Yuntian Theodore, and Terry C. Lowe. "Observations and issues on mechanisms of grain refinement during ECAP process." *Materials Science and Engineering: A* 291, no. 1-2 (2000): 46-53.

34. Krüger, L., F. Schwarz, M. Mandel, and M. Hockauf. "Electrochemical corrosion studies of ultrafine-grained aluminium alloy EN AW-6063." *Materials and Corrosion* 66, no. 3 (2015): 226-232.

35. Wei, Q., L. Kecskes, T. Jiao, K. T. Hartwig, K. T. Ramesh, and E. Ma. "Adiabatic shear banding in ultrafine-grained Fe processed by severe plastic deformation." *Acta materialia* 52, no. 7 (2004): 1859-1869.

36. Li, Y. S., N. R. Tao, and K. Lu. "Microstructural evolution and nanostructure formation in copper during dynamic plastic deformation at cryogenic temperatures." *Acta Materialia* 56, no. 2 (2008): 230-241.

37. Mogucheva, A., E. Babich, B. Ovsyannikov, and R. Kaibyshev. "Microstructural evolution in a 5024 aluminum alloy processed by ECAP with and without back pressure." *Materials Science and Engineering: A* 560 (2013): 178-192.

38. Kawasaki, Megumi, Zenji Horita, and Terence G. Langdon. "Microstructural evolution in high purity aluminum processed by ECAP." *Materials Science and Engineering: A* 524, no. 1-2 (2009): 143-150.

39. Lieou, Charles KC, and Curt A. Bronkhorst. "Dynamic recrystallization in adiabatic shear banding: Effective-temperature model and comparison to experiments in ultrafine-grained titanium." *International Journal of Plasticity* 111 (2018): 107-121.

40. Meyers, Marc A., Vitali F. Nesterenko, Jerry C. LaSalvia, and Qing Xue. "Shear localization in dynamic deformation of materials: microstructural evolution and self-organization." *Materials Science and Engineering: A* 317, no. 1-2 (2001): 204-225.

41. Meyers, M. A., Y. B. Xu, Q. Xue, M. T. Perez-Prado, and T. R. McNelley. "Microstructural evolution in adiabatic shear localization in stainless steel." *Acta Materialia* 51, no. 5 (2003): 1307-1325.

42. Li, Zezhou, Bingfeng Wang, Shiteng Zhao, Ruslan Z. Valiev, Kenneth S. Vecchio, and Marc A. Meyers. "Dynamic deformation and failure of ultrafine-grained titanium." *Acta Materialia* 125 (2017): 210-218.

43. Mckenzie, Peter William James, Rimma Lapovok, and Yuri Estrin. "The influence of back pressure on ECAP processed AA 6016: Modeling and experiment." *Acta Materialia* 55, no. 9 (2007): 2985-2993.

44. Zehetbauer, M. J., H. P. Stüwe, A. Vorhauer, E. Schafler, and J. Kohout. "The role of hydrostatic pressure in severe plastic deformation." *Advanced Engineering Materials* 5, no. 5 (2003): 330-337.

45. Hahn, Eric N., and Marc A. Meyers. "Grain-size dependent mechanical behavior of nanocrystalline metals." *Materials Science and Engineering: A* 646 (2015): 101-134.

46. Roven, Hans J., Manping Liu, and Jens C. Werenskiold. "Dynamic precipitation during severe plastic deformation of an Al–Mg–Si aluminium alloy." *Materials Science and Engineering: A* 483 (2008): 54-58.

47. Angella, Giuliano, Paola Bassani, Ausonio Tuissi, and Maurizio Vedani. "Aging behaviour and mechanical properties of a solution treated and ECAP processed 6082 alloy." *Materials transactions* 45, no. 7 (2004): 2282-2287.

48. Ferrasse, Stephane, Vladimir M. Segal, K. Theodore Hartwig, and Ramon E. Goforth. "Development of a submicrometer-grained microstructure in aluminum 6061 using equal channel angular extrusion." *Journal of materials research* 12, no. 5 (1997): 1253-1261.

49. Kim, W. J., J. K. Kim, T. Y. Park, S. I. Hong, D. I. Kim, Y. S. Kim, and J. D. Lee. "Enhancement of strength and superplasticity in a 6061 Al alloy processed by equal-channel-angular-pressing." *Metallurgical and materials transactions A* 33, no. 10 (2002): 3155-3164.

50. Kim, J. K., H. G. Jeong, S. I. Hong, Y. S. Kim, and W. J. Kim. "Effect of aging treatment on heavily deformed microstructure of a 6061 aluminum alloy after equal channel angular pressing." *Scripta materialia* 45, no. 8 (2001): 901-907.

51. Chowdhury, Sandip Ghosh, Cheng Xu, and Terence G. Langdon. "Texture evolution in an aluminum alloy processed by ECAP with concurrent precipitate fragmentation." *Materials Science and Engineering: A* 473, no. 1-2 (2008): 219-225.

52. Angella, Giuliano, Paola Bassani, Ausonio Tuissi, and Maurizio Vedani. "Intermetallic particle evolution during ECAP processing of a 6082 alloy." *Materials transactions* 45, no. 7 (2004): 2182-2186.

53. Murayama, M., Zenji Horita, and K. Hono. "Microstructure of two-phase Al–1.7 at% Cu alloy deformed by equal-channel angular pressing." *Acta Materialia* 49, no. 1 (2001): 21-29.

54. Gao, Nong, Marco J. Starink, Minoru Furukawa, Zenji Horita, Cheng Xu, and Terence G. Langdon. "Microstructural evolution in a spray-cast aluminum alloy during equal-channel angular pressing." *Materials Science and Engineering: A* 410 (2005): 303-307.

55. Verwey, 1. EJW. "Electrolytic conduction of a solid insulator at high fields The formation of the anodic oxide film on aluminium." *Physica* 2, no. 1-12 (1935): 1059-1063.

56. Mott, N. F. "The theory of the formation of protective oxide films on metals.—III." *Transactions of the Faraday Society* 43 (1947): 429-434.

57. Mott, N. F. "The theory of the formation of protective oxide films on metals, II." *Transactions of the faraday society* 35 (1940): 472-483.

58. Chao, C. Y., L. F. Lin, and D. D. Macdonald. "A point defect model for anodic passive films I. Film growth kinetics." *Journal of the Electrochemical Society* 128, no. 6 (1981): 1187-1194.

59. Macdonald, Digby D. "The point defect model for the passive state." *Journal of the Electrochemical Society* 139, no. 12 (1992): 3434-3449.

60. Lin, L. F., C. Y. Chao, and D. D. Macdonald. "A point defect model for anodic passive films II. Chemical breakdown and pit initiation." *Journal of the Electrochemical Society* 128, no. 6 (1981): 1194-1198.

61. Soltis, J. "Passivity breakdown, pit initiation and propagation of pits in metallic materials–review." *Corrosion Science* 90 (2015): 5-22.

62. Frankel, G. S. "Pitting corrosion of metals a review of the critical factors." *Journal of the Electrochemical society* 145, no. 6 (1998): 2186-2198.

63. Evans, Ulick Richardson. "CXL.—The passivity of metals. Part I. The isolation of the protective film." *Journal of the Chemical Society (Resumed)* (1927): 1020-1040.

64. Frankel, G. S. "Pitting corrosion of metals a review of the critical factors." *Journal of the Electrochemical society* 145, no. 6 (1998): 2186-2198.

65. Hoar, T. P., and W. R. Jacob. "Breakdown of passivity of stainless steel by halide ions." *Nature* 216, no. 5122 (1967): 1299.

66. Uhlig, Herbert H. "Adsorbed and Reaction-Product Films on Metals." *Journal of the Electrochemical Society* 97, no. 11 (1950): 215C-220C.

67. Kolotyrkin, Ja M. "Effects of anions on the dissolution kinetics of metals." *Journal of the Electrochemical Society* 108, no. 3 (1961): 209-216.

68. Hoar, T. P. "The production and breakdown of the passivity of metals." *Corrosion Science* 7, no. 6 (1967): 341-355.

69. Sato, N., K. Kudo, and T. Noda. "The anodic oxide film on iron in neutral solution." *Electrochimica Acta* 16, no. 11 (1971): 1909-1921.

70. Vargel, Christian. *Corrosion of aluminium*. Elsevier, 2004.

71. Wang, Shanlin. "Corrosion resistance and electrocatalytic properties of metallic glasses." *Metallic Glasses-Formation and Properties* (2016).

72. Birbilis, Nick, and Rudolph G. Buchheit. "Electrochemical characteristics of intermetallic phases in aluminum alloys an experimental survey and discussion." *Journal of The Electrochemical Society* 152, no. 4 (2005): B140-B151.

73. McCafferty, E. "Introduction to corrosion science. 2010." *Alexandria: Springer*.

74. Sukiman, N. L., X. Zhou, N. Birbilis, A. E. Hughes, J. M. C. Mol, S. J. Garcia, X. Zhou, and G. E. Thompson. "Durability and corrosion of aluminium and its alloys: overview, property space, techniques and developments." *Aluminium Alloys-New Trends in Fabrication and Applications* (2012): 47-97.

75. Zhang, Weilong, and G. S. Frankel. "Transitions between pitting and intergranular corrosion in AA2024." *Electrochimica Acta* 48, no. 9 (2003): 1193-1210.

76. Ralston, K. D., Nick Birbilis, Matthew Weyland, and C. R. Hutchinson. "The effect of precipitate size on the yield strength-pitting corrosion correlation in Al–Cu–Mg alloys." *Acta Materialia* 58, no. 18 (2010): 5941-5948.

77. Buchheit Jr, R. G., J. P. Moran, and G. E. Stoner. "Localized corrosion behavior of alloy 2090—the role of microstructural heterogeneity." *Corrosion* 46, no. 8 (1990): 610-617.

78. Kairy, S. K., S. Turk, N. Birbilis, and A. Shekhter. "The role of microstructure and microchemistry on intergranular corrosion of aluminium alloy AA7085-T7452." *Corrosion Science* 143 (2018): 414-427.

79. Zhang, Ruifeng, Yao Qiu, Yuanshen Qi, and Nick Birbilis. "A closer inspection of a grain boundary immune to intergranular corrosion in a sensitised Al-Mg alloy." *Corrosion Science* 133 (2018): 1-5.

80. Minoda, T., and H. Yoshida. "Effect of grain boundary characteristics on intergranular corrosion resistance of 6061 aluminum alloy extrusion." *Metallurgical and Materials Transactions A* 33, no. 9 (2002): 2891-2898.

81. S Svenningsen, Gaute, John Erik Lein, Astrid Bjørgum, Jan Halvor Nordlien, Yingda Yu, and Kemal Nisancioglu. "Effect of low copper content and heat treatment on intergranular corrosion of model AlMgSi alloys." *Corrosion science* 48, no. 1 (2006): 226-242.

82. Zou, Yun, Qing Liu, Zhihong Jia, Yuan Xing, Lipeng Ding, and Xueli Wang. "The intergranular corrosion behavior of 6000-series alloys with different Mg/Si and Cu content." *Applied Surface Science* 405 (2017): 489-496.

83. Liang, Wen Jie, P. A. Rometsch, L. F. Cao, and Nick Birbilis. "General aspects related to the corrosion of 6xxx series aluminium alloys: Exploring the influence of Mg/Si ratio and Cu." *Corrosion science* 76 (2013): 119-128.

84. Svenningsen, Gaute, Magnus Hurlen Larsen, Jan Halvor Nordlien, and Kemal Nisancioglu. "Effect of thermomechanical history on intergranular corrosion of extruded AlMgSi (Cu) model alloy." *Corrosion science* 48, no. 12 (2006): 3969-3987.

85. PAN, Dao-zhao, Zhi-xiu WANG, Hai Li, and Zi-qiao ZHENG. "Effects of two-step ageing treatment on tensile properties and intergranular corrosion of 6061 aluminum alloy." *The Chinese Journal of Nonferrous Metal* 20, no. 3 (2010): 435-441.

86. Fattah-alhosseini, Arash, and Seyed Omid Gashti. "Passive behavior of ultra-fine-grained 1050 aluminum alloy produced by accumulative roll bonding in a borate buffer solution." *Acta Metallurgica Sinica (English Letters)* 28, no. 10 (2015): 1222-1229.

87. Gashti, Seyed Omid, Arash Fattah-alhosseini, Yoosef Mazaheri, and Mohsen K. Keshavarz. "Effect of grain refinement on mechanical and electrochemical properties of ultra-fine grained AA1050 fabricated via ARB process." *Journal of Manufacturing Processes* 22 (2016): 269-277.

88. Akiyama, Eiji, Zuogui Zhang, Yoshimi Watanabe, and Kaneaki Tsuzaki. "Effects of severe plastic deformation on the corrosion behavior of aluminum alloys." *Journal of Solid State Electrochemistry* 13, no. 2 (2009): 277-282.

89. Dan, Song, Jing-hua JIANG, Pin-hua LIN, and Dong-hui YANG. "Corrosion behavior of ultra-fine grained industrial pure Al fabricated by ECAP." *Transactions of Nonferrous Metals Society of China* 19, no. 5 (2009): 1065-1070.

90. Sherif, El-Sayed M., Ehab A. El-Danaf, Mahmoud S. Soliman, and Abdulhakim A. Almajid. "Corrosion passivation in natural seawater of aluminum alloy 1050 processed by equal-channel-angular-press." *Int. J. Electrochem. Sci* 7 (2012): 2846-2859.

91. Chung, Min-Kyong, Yoon-Seok Choi, Jung-Gu Kim, Young-Man Kim, and Jae-Chul Lee. "Effect of the number of ECAP pass time on the electrochemical properties of 1050 Al alloys." *Materials Science and Engineering: A* 366, no. 2 (2004): 282-291.

92. Wang, Xue, Mengyan Nie, Chuan Ting Wang, Shun Cai Wang, and Nong Gao. "Microhardness and corrosion properties of hypoeutectic Al–7Si alloy processed by high-pressure torsion." *Materials & Design* 83 (2015): 193-202.

93. Son, In-Joon, Hiroaki Nakano, Satoshi Oue, Shigeo Kobayashi, Hisaaki Fukushima, and Zenji Horita. "Pitting corrosion resistance of ultrafine-grained aluminum processed by severe plastic deformation." *Materials Transactions* 47, no. 4 (2006): 1163-1169.

94. Brunner, J. G., Nick Birbilis, K. D. Ralston, and Sannakaisa Virtanen. "Impact of ultrafine-grained microstructure on the corrosion of aluminium alloy AA2024." *Corrosion Science* 57 (2012): 209-214.

95. Wei, Wei, Kun Xia Wei, and Qing Bo Du. "Corrosion and tensile behaviors of ultra-fine grained Al–Mn alloy produced by accumulative roll bonding." *Materials Science and Engineering: A* 454 (2007): 536-541.

96. Hockauf, Matthias, Lothar W. Meyer, Daniela Nickel, Gert Alisch, Thomas Lampke, Bernhard Wielage, and Lutz Krüger. "Mechanical properties and corrosion behaviour of ultrafine-grained AA6082 produced by equal-channel angular pressing." *Journal of Materials Science* 43, no. 23-24 (2008): 7409-7417.

97. Nickel, Daniela, Dagmar Dietrich, Thomas Mehner, Philipp Frint, Dagobert Spieler, and Thomas Lampke. "Effect of strain localization on pitting corrosion of an AlMgSi0. 5 alloy." *Metals* 5, no. 1 (2015): 172-191.

98. Jilani, Oussama, Nabil Njah, and Pierre Ponthiaux. "Transition from intergranular to pitting corrosion in fine grained aluminum processed by equal channel angular pressing." *Corrosion Science* 87 (2014): 259-264.

99. Brunner, J. G., J. May, H. W. Höppel, M. Göken, and S. Virtanen. "Localized corrosion of ultrafine-grained Al–Mg model alloys." *Electrochimica Acta* 55, no. 6 (2010): 1966-1970.

100. Fattah-Alhosseini, A., S. O. Gashti, and M. K. Keshavarz. "Effect of film formation potential on passive behavior of ultra-fine-grained 1050 Al alloy fabricated via ARB process." *Journal of Materials Engineering and Performance* 25, no. 4 (2016): 1683-1689.

101. Nejadseyfi, Omid, Ali Shokuhfar, Amirreza Dabiri, and Amin Azimi. "Combining equal-channel angular pressing and heat treatment to obtain enhanced corrosion resistance in 6061 aluminum alloy." *Journal of Alloys and Compounds* 648 (2015): 912-918.

102. Jinlong, Lv, Liang Tongxiang, Wang Chen, and Guo Ting. "The passive film characteristics of several plastic deformation 2099 Al–Li alloy." *Journal of Alloys and Compounds* 662 (2016): 143-149.

103. Balluffi, Robert W., Sam Allen, and W. Craig Carter. *Kinetics of materials*. John Wiley & Sons, 2005.

104. Xu, Cheng, Minoru Furukawa, Zenji Horita, and Terence G. Langdon. "Using ECAP to achieve grain refinement, precipitate fragmentation and high strain rate superplasticity in a spray-cast aluminum alloy." *Acta materialia* 51, no. 20 (2003): 6139-6149.

105. Zhang, R., R. K. Gupta, C. H. J. Davies, A. M. Hodge, M. Tort, K. Xia, and N. Birbilis. "The influence of grain size and grain orientation on sensitization in AA5083." *Corrosion* 72, no. 2 (2015): 160-168.

106. WeiIandZ, LH Chanl H., S. Cheongz, Rohrer GS, and A. D. Rollettl. "The correlation between grain boundary character and intergranualr corrosion susceptibility of 2124 aluminum alloy". *Applications of Texture Analysis* 201 (2008): 261.

107. Guérin, Mathilde, Joël Alexis, Eric Andrieu, Lydia Laffont, Williams Lefebvre, Grégory Odemer, and Christine Blanc. "Identification of the metallurgical parameters explaining the corrosion susceptibility in a 2050 aluminium alloy." *Corrosion Science* 102 (2016): 291-300.

108. Takayama, Yoshimasa, Masayuki Sato, and Hideo Watanabe. "Crystallographic Orientation Dependence of Corrosion Behabior of 5N Purity Aluminum in Different Concentrations of HCl Aqueous Solutions." In *ICAA13 Pittsburgh*, pp. 391-396. Springer, Cham, 2012.

109. Yan, Jianfeng, Nathan M. Heckman, Leonardo Velasco, and Andrea M. Hodge. "Improve sensitization and corrosion resistance of an Al-Mg alloy by optimization of grain boundaries." *Scientific reports* 6 (2016): 26870.

110. Luo, C., X. Zhou, G. E. Thompson, and A. E. Hughes. "Observations of intergranular corrosion in AA2024-T351: The influence of grain stored energy." *Corrosion Science* 61 (2012): 35-44.

111. Zhang, Xinxin, Xiaorong Zhou, Jan-Olov Nilsson, Zehua Dong, and Changrun Cai. "Corrosion behaviour of AA6082 Al-Mg-Si alloy extrusion: Recrystallized and non-recrystallized structures." *Corrosion Science* 144 (2018): 163-171.

112. Ma, Y., X. Zhou, Y. Liao, Y. Yi, H. Wu, Z. Wang, and W. Huang. "Localised corrosion in AA 2099-T83 aluminium-lithium alloy: the role of grain orientation." *Corrosion Science* 107 (2016): 41-48.

113. Zhou, X., C. Luo, Y. Ma, T. Hashimoto, G. E. Thompson, A. E. Hughes, and P. Skeldon. "Grain-stored energy and the propagation of intergranular corrosion in AA2xxx aluminium alloys." *Surface and Interface analysis* 45, no. 10 (2013): 1543-1547.

114. Casals, N. Fuertes, Andrej Nazarov, Flavien Vucko, Rachel Pettersson, and Dominique Thierry. "Influence of mechanical stress on the potential distribution on a 301 LN stainless steel surface." *Journal of The Electrochemical Society* 162, no. 9 (2015): C465-C472.

115. Casals, N. Fuertes, Andrej Nazarov, Flavien Vucko, Rachel Pettersson, and Dominique Thierry. "Influence of mechanical stress on the potential distribution on a 301 LN stainless steel surface." *Journal of The Electrochemical Society* 162, no. 9 (2015): C465-C472.

116. Smoluchowski, Roman. "Anisotropy of the electronic work function of metals." *Physical Review* 60, no. 9 (1941): 661.

117. Rohwerder, Michael, and Florin Turcu. "High-resolution Kelvin probe microscopy in corrosion science: scanning Kelvin probe force microscopy (SKPFM) versus classical scanning Kelvin probe (SKP)." *Electrochimica Acta* 53, no. 2 (2007): 290-299.

118. Schmutz, P., and G. S. Frankel. "Characterization of AA2024-T3 by scanning Kelvin probe force microscopy." *Journal of the Electrochemical Society* 145, no. 7 (1998): 2285-2295.

119. Örnek, C., and D. L. Engelberg. "SKPFM measured Volta potential correlated with strain localisation in microstructure to understand corrosion susceptibility of cold-rolled grade 2205 duplex stainless steel." *Corrosion Science* 99 (2015): 164-171.

120. Murashkin, M. Yu, I. Sabirov, X. Sauvage, and R. Z. Valiev. "Nanostructured Al and Cu alloys with superior strength and electrical conductivity." *Journal of materials science* 51, no. 1 (2016): 33-49.

121. Valiev, Ruslan Z., M. Yu Murashkin, and Ilchat Sabirov. "A nanostructural design to produce high-strength Al alloys with enhanced electrical conductivity." *Scripta Materialia* 76 (2014): 13-16.

122. Sauvage, X., E. V. Bobruk, M. Yu Murashkin, Y. Nasedkina, N. A. Enikeev, and R. Z. Valiev. "Optimization of electrical conductivity and strength combination by structure design at the nanoscale in Al–Mg–Si alloys." *Acta Materialia* 98 (2015): 355-366.

123. Valiev, Ruslan. "Nanostructuring of metals by severe plastic deformation for advanced properties." *Nature materials* 3, no. 8 (2004): 511.

124. Ralston, K. D., and Nick Birbilis. "Effect of grain size on corrosion: a review." *Corrosion* 66, no. 7 (2010): 075005-075005.

125. Ralston, K. D., Dan Fabijanic, and Nick Birbilis. "Effect of grain size on corrosion of high purity aluminium." *Electrochimica acta* 56, no. 4 (2011): 1729-1736.

126. Chen, G. S., M. Gao, and R. P. Wei. "Microconstituent-induced pitting corrosion in aluminum alloy 2024-T3." *corrosion* 52, no. 1 (1996): 8-15.

127. Meyers, Marc A., A. Mishra, and David J. Benson. "Mechanical properties of nanocrystalline materials." *Progress in materials science* 51, no. 4 (2006): 427-556.

128. Svenningsen, Gaute, Magnus Hurlen Larsen, John Charles Walmsley, Jan Halvor Nordlien, and Kemal Nisancioglu. "Effect of artificial aging on intergranular corrosion of extruded AlMgSi alloy with small Cu content." *Corrosion science* 48, no. 6 (2006): 1528-1543.

129. Valiev, Ruslan Z., and Terence G. Langdon. "Principles of equal-channel angular pressing as a processing tool for grain refinement." *Progress in materials science* 51, no. 7 (2006): 881-981.

130. Iwahashi, Yoshinori, Zenji Horita, Minoru Nemoto, and Terence G. Langdon. "The process of grain refinement in equal-channel angular pressing." *Acta materialia* 46, no. 9 (1998): 3317-3331.

131. Taylor, John A. "Iron-containing intermetallic phases in Al-Si based casting alloys." *Procedia Materials Science* 1 (2012): 19-33.

132. Tanem, Bjørn S., Gaute Svenningsen, and Jostein Mårdalen. "Relations between sample preparation and SKPFM Volta potential maps on an EN AW-6005 aluminium alloy." *Corrosion science* 47, no. 6 (2005): 1506-1519.

133. Ovid'Ko, I. A., R. Z. Valiev, and Y. T. Zhu. "Review on superior strength and enhanced ductility of metallic nanomaterials." *Progress in Materials Science* 94 (2018): 462-540.

134. Ly, Ramatou, Karl T. Hartwig, and Homero Castaneda. "Influence of dynamic recrystallization and shear banding on the localized corrosion of severely deformed Al–Mg–Si alloy." *Materialia* 4 (2018): 457-465.

135. Ly, Ramatou, Karl T. Hartwig, and Homero Castaneda. "Effects of strain localization on the corrosion behavior of ultra-fine grained aluminum alloy AA6061." *Corrosion Science* 139 (2018): 47-57.

136. Kim, S. H., U. Erb, K. T. Aust, and G. Palumbo. "Grain boundary character distribution and intergranular corrosion behavior in high purity aluminum." *Scripta materialia* 5, no. 44 (2001): 835-839.

137. Lins, J. F. C., H. R. Z. Sandim, H-J. Kestenbach, D. Raabe, and K. S. Vecchio. "A microstructural investigation of adiabatic shear bands in an interstitial free steel." *Materials Science and Engineering: A* 457, no. 1-2 (2007): 205-218.

138. Nicolas, Andrea, Alberto W. Mello, and Michael D. Sangid. "The effect of strain localization on galvanic corrosion pitting in AA7050." *Corrosion* 74, no. 8 (2018): 860-872.

139. Meng, Guozhe, Ying Li, and Fuhui Wang. "The corrosion behavior of Fe–10Cr nanocrystalline coating." *Electrochimica acta* 51, no. 20 (2006): 4277-4284.

140. Gupta, Rajeev K., RK Singh Raman, Carl C. Koch, and B. S. Murty. "Effect of nanocrystalline structure on the corrosion of a Fe20Cr alloy." *Int. J. Electrochem. Sci* 8, no. 6791 (2013): e6806.

141. Wu, S. D., Z. G. Wang, C. B. Jiang, G. Y. Li, I. V. Alexandrov, and R. Z. Valiev. "The formation of PSB-like shear bands in cyclically deformed ultrafine grained copper processed by ECAP." *Scripta Materialia* 48, no. 12 (2003): 1605-1609.

142. Gray III, George Thompson, K. S. Vecchio, and Veronica Livescu. "Compact forced simple-shear sample for studying shear localization in materials." *Acta Materialia* 103 (2016): 12-22.

143. Barrett, Christopher D., Aidin Imandoust, Andrew L. Oppedal, Kaan Inal, Mark A. Tschopp, and Haitham El Kadiri. "Effect of grain boundaries on texture formation during dynamic recrystallization of magnesium alloys." *Acta Materialia* 128 (2017): 270-283.

144. Wigner, E. P., and J. Bardeen. "Theory of the work functions of monovalent metals." In *Part I: Physical Chemistry. Part II: Solid State Physics*, pp. 398-401. Springer, Berlin, Heidelberg, 1997.